ABSTRACT

INVESTIGATING IONOSPHERIC PARAMETERS USING THE PLASMA LINE MEASUREMENTS FROM INCOHERENT SCATTER RADAR

by Julio Santana III

Because of deficiencies in sampling resolution and storage space, the plasma line frequency component of the incoherent scatter radar (ISR) spectrum has been neglected in experimentally verifying ionospheric parameters. Several incoherent scatter theories were independently developed with confirmation from low resolution data in the 1960s that used the plasma line resonant frequency and plasma line peak intensity to derive ionospheric parameters. Now that higher resolution measurement techniques exist, this thesis investigates three methods for obtaining plasma line resonant frequency, peak intensity, and spectral width. Following this study, several salient features endemic to the ISR experiment performed on January 15-17th, and January 22nd of 2010 are presented and analyzed.

INVESTIGATING IONOSPHERIC PARAMETERS USING THE PLASMA LINE MEASUREMENTS FROM INCOHERENT SCATTER RADAR

A Thesis

Submitted to the

Faculty of Miami University

in partial fulfillment of

the requirements for the degree of

Master of Science in Computational Science and Engineering

Department of Electrical and Computer Engineering

by

Julio Santana III

Miami University

Oxford, Ohio

2012

Advisor_____

Qihou Zhou

Reader_____

Jade Y. Morton

Reader_____

Chi Hao Cheng

Table of Contents

LIST OF TABLES

LIST OF FIGURES

ACKNOWLEDGEMENTS

This thesis would not have come together without help, support, and guidance of many people who I would be remiss in failing to thank.

When Dr. Qihou Zhou offered to work with me on a Master's thesis, I could not have imagined the winding, hazy path I would pursue over the two years that followed. Both the seemingly endless body of knowledge he possesses on the ionosphere, radar systems, and several other related fields, and the creativity he demonstrated in his suggestions for the presentation of the results were immeasurably helpful in getting me to the finish line. More importantly, his kind and even demeanor was an inestimable relief through the research and writing process. It is because of his advising that I will continue on in this field.

I would also like to thank Dr. Jade Morton and Dr. Chi-Hao Cheng, who were on my committee. I feel extremely fortunate to have had Dr. Morton in capacities as an instructor and as a committee member, as her guidance and support during this process have been invaluable. The work ethic and passion she brings to academic research is only matched by the compassion she displays for her students; I could not have completed my thesis without being a direct beneficiary of both. I am also thankful for Dr. Cheng's presence on my committee, particularly for his aide in signal processing suggestions.

Additional thanks go to Dr. Jim Moller for being my undergraduate research advisor. Though my discipline is different now, a thirst for scientific research was borne from the support and patience of his interactions with this inexperienced research student.

Special thanks are required to Dr. Jens Mueller and Dr. Greg Reese at Miami University's Research Computing Services; without their help, the total computational time of my data processing for this thesis would be measured in years instead of days.

I wish to thank my research colleagues, Mr. Lyndon Pearson and Dr. Yun Gong, for their academic advice and assistance over the last two years. Their constructive feedback has been immensely helpful.

I would also like to thank my sister, Jesenia Santana, for her frequent encouragement and support.

There are a number of people who are neither blood relatives nor academics in this field whose contributions to my thesis are either intangible or immeasurable, but ultimately, I could

not have done without. Due thanks go to Christopher Blanchard, Kasey Butcher, Kevin Donges, Erik Hajek, Aaron Jimenez, L.R. Laggy, Matthew Lewis, Zachary McCoy, Cassidy Nolan, Joseph Scalf, Jill Schmidt, Richard Taylor, and Anika Wiltgen for walking with me in various capacities over the last two years. I am immensely grateful and beholden to them for their peripheral support in research and writing – directly and indirectly.

Finally, I wish to thank my parents, Julio Santana Jr. and Gladys Santana. From birth to now, they have served as my inspiration due to their perseverance, their dedication to my success, and their infinite compassion towards the people they encounter. It is because of their nurturing love and guidance that I am able to pursue my Master of Science. This thesis is gratefully dedicated to them.

1. Executive Summary

Incoherent Scatter Radar (ISR) systems have been used to study ionospheric parameters for decades. The plasma line component of the spectrum was given some theoretical treatment in the 1960's with rudimentary experimental confirmation of developed theory. As data resolution improved through the development of both more robust hardware and effective pulse compression techniques, high resolution confirmation of plasma line theory has been revisited by the scientific community in recent years. This thesis will add to these efforts by studying the data recovered from a dual beam ISR experiment conducted January 15th-17th in 2010. The first objective is to utilize several processing methods in an effort to cleanly extract the plasma line resonant frequencies, intensities, and spectral widths. This entails using simple techniques to extract the plasma line above the noise and clutter level and comparing these results with those obtained from more elaborate extrapolations that attempt to refine the procedure to allow more accurate extraction. The second objective involves investigating salient features of the data that explain physical characteristics of the medium. This includes the presentation and explanation of the drivers for plasma line intensity and spectral width, as well a discussion regarding the low level of the plasma densities. Additionally, because the beam was in rotation during this experiment, ionospheric tilting is studied, and photoelectron propagation is investigated by comparing the plasma line of the upshifted and downshifted peaks.

2. Introduction and Background

2.1 The Purpose of Ionospheric Research

The Earth's ionosphere is a weakly ionized plasma that forms a shell around the Earth. This layer coexists with both the mesospheric and thermospheric regions of the neutral atmosphere, and the topside ionosphere forms the inner layer of the magnetosphere. One way of layer designation for the neutral atmosphere is categorized by ambient temperature, while the various layers of the ionosphere are divided by plasma density as shown in Figure 1.

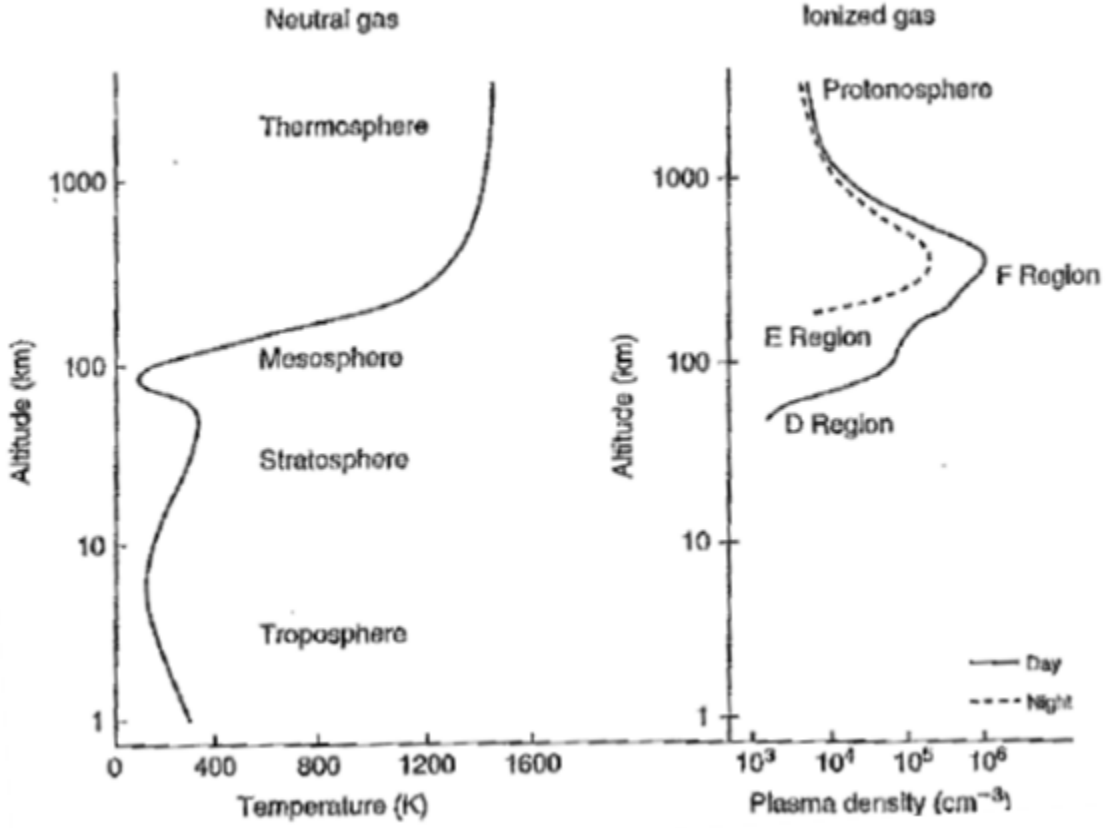

Figure 1: Categorical Layers of Neutral and Ionized Atmosphere (Kelley, 2008).

The presence of charged particles and their interactions in this region has demonstrable benefits and detriments. While the ionosphere provides a suitable shield for protection from harmful solar radiation, the electrostatic fields generated by the charged particles can be devastating to spacecraft and will disrupt radio frequency waves transmitted through, or in

tangential contact with, the region (e.g., Kelley, 2008). These latter effects delineate a need for robust ionospheric understanding.

Shortly after World War II, as various nations competed to explore extraterrestrial space, ionospheric phenomena were studied with heavy interest. As a result of this reinforced interest and the development of higher precision measurement techniques, ionospheric knowledge evolved to describe a largely chaotic, ever changing body of particles whose salient features are not easily detected nor explained. An ionospheric scientist today treats the medium with a mixture of fundamental aeronomical analysis, electrodynamics, and classical fluid theory. Mike Kelley describes the ionosphere as, "a battleground between the earth's neutral atmosphere and the sun's fully ionized atmosphere in which the earth is embedded" (Kelley, 2008), and this conflict facilitates theory that, over the past several decades, has changed dramatically as the research community resolves these competitive interactions into a useful body of knowledge.

2.2 Aeronomy and Plasma Physics

Fundamental parameters of interest include electron density, electron temperature, ion temperature, and ionic composition. Electron density provides the basis for separating the ionosphere into its colloquially described layers: the D region, the E region, and the F region. As shown in Figure 2, the daytime electron density allows for distinction between the layers as labeled, with the F region subdivided into F1 and F2 layers by the peaks shown.

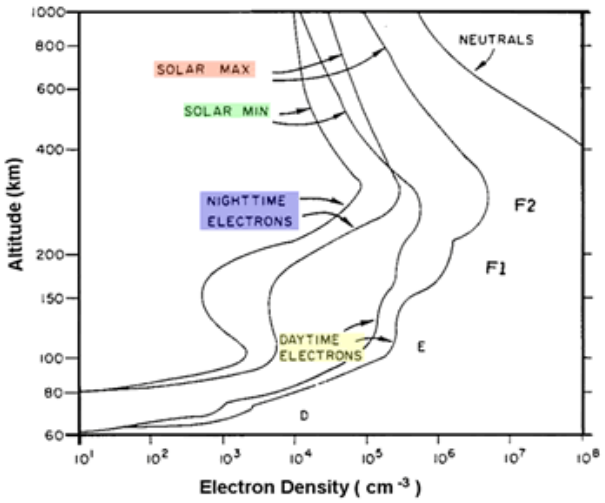

Figure 2: Logarithmic Graph of Daytime Electron Densities in the Ionosphere.

These layers are not easily detectable at nighttime because photoionization does not enhance the density of charged particles when incident solar rays are not present. During the day, as photoionization pumps energy into the ionosphere, that energy exacerbates system dynamics as the larger number of free floating electrons move more quickly in the system and at higher temperatures. Because the photoelectron enhanced particles move more quickly than the Maxwellian velocity distribution for electrons would predict, these particles are referred to as a "high energy tail of photo-electrons" (Yngvesson & Perkins, 1968).

Though the fundamental parameters of interest aide in characterizing the system, they must be considered in tandem with the propagating waves endemic to the region. The primary waves in the measurement techniques investigated in this thesis are electrostatic ion acoustic waves, the electrostatic component of whistler mode waves, and electrostatic Langmuir waves. Since the ionosphere is a dispersive medium, the wave velocity is not distinct. Therefore, wave characterization does not end with Maxwell's Wave Equation (Eq. 1), (where ∇^2 is the Laplace operator, B is the magnetic field, and $\frac{1}{\sqrt{\mu\epsilon}} = c$, the speed of light) but with dispersion relations that explore the frequency dependent effects of propagation (Stix, 1962).

$$\left(\nabla^2 - \mu\epsilon\frac{\delta^2}{\delta t^2}\right)B = 0 \qquad \text{Eq. 1}$$

Wave dispersion can be seen visually if sunlight is passed through a prism. While the light particles continue to travel at the speed of light, the optical observation of a complete visual spectrum implies the presence of waves propagating at different frequencies for different wavelengths (Knight, 2004). This phenomenon prescribes the need for two velocities to define the rate of wave propagation in a dispersive medium: phase velocity and group velocity. Phase velocity, as the name suggests, governs the spatial rate at which the phase of the wave travels. Through a dispersive medium, multiple phase velocities are considered as each describes the phase speed for a lone frequency component of the complete wave. In general, the phase velocity for a simple propagating sinusoid is (Brillouin, 1960):

$$v_p = \frac{\delta x}{\delta t} = \frac{\lambda}{T} = \frac{\omega}{k};\ \omega = \frac{1}{T}; k = \frac{1}{\lambda} \qquad \text{Eq. 2}$$

Where v_p is the phase velocity, x is distance, t is time, T is the period of the wave, ω is the wave's frequency, k is the wave number, and λis the wavelength.

Group velocity, in contrast, describes how the envelope of the wave propagates through the same space. In the same way as phase velocity, multiple group velocities arise, each as a function of wavelength (Brillouin, 1960). The defining equation for group velocity is (Brillouin, 1960):

$$v_g = \frac{\delta\omega}{\delta k} \quad \text{Eq. 3}$$

In a dispersive medium, angular frequency, ω, is a function of the wavenumber, *k*. The relation ω(*k*) for a wave is the aforementioned dispersion relation requisite to decompose the wave analytically into terms that correspond to different physical processes as described below. Ion acoustic waves propagate as longitudinal oscillations of positively charged ions with properties similar to acoustic waves traveling through a neutral gas. Because the medium is charged, ion acoustic wave propagation also entails electromagnetic field interaction and particle collisions that provide salient features in measurement integral to both understanding wave behavior and to deriving particle properties of the medium (Kelley, 2008). The dispersion relation used to describe ion acoustic waves is:

$$\omega^2 = k^2 v_s^2 = k^2 \frac{(\gamma_e K T_e + \gamma_i K T_i)}{M} \quad \text{Eq. 4}$$

Where γ_x is the ratio of specific heats for species x (e are electrons, i are ions), K is Boltzmann's constant, M is ion mass, and T_x is the temperature of the species x.

Spectral measurements of the ionosphere show the existence of an ion acoustic wave component. The two other prominent artifacts evident in the spectra are governed by Whistler mode waves and Langmuir waves, respectively. Whistler mode waves and their relationship to electron gyro resonance was first identified in Salpeter's 1961 article, *Plasma Density Fluctuations in a Magnetic Field* (Salpeter, 1961), and then expounded upon in Trulsen's *Influence of Electrostatic Electron Waves on the Incoherent Scattering Cross Section* (Trulsen, 1978). The dispersion relation for electrostatic electron waves in the magnetized plasma is given by:

$$\omega^2(\omega^2 - \omega_H^2) + \omega_p^2 \Omega^2 \cos^2 \alpha = 0 \quad \text{Eq. 5}$$

When treated analytically, detection of these waves elicits a derivation of eigenfrequencies that have two solution forms. The appropriate selection of analytical relations (Eqs. 6, 7, 8, 9) is contingent on the relationship between the plasma resonance frequency, ω_p, and electron gyrofrequency, Ω. If the plasma is weakly magnetized ($\omega_p^2 >> \Omega^2$), the first set of

equations (Eqs. 6, 7) describe the dispersion of the elementary plasma waves, whereas if the plasma is strongly magnetized ($\omega_p^2 << \Omega$), the second set (Eqs. 8, 9) is used (Trulsen, 1978).

$$\omega_1{}^2 = \omega_p^2(1 + \frac{\Omega^2}{\omega_p^2} sin^2\alpha) \quad \text{Eq. 6}$$

$$\omega_2{}^2 = \Omega^2(1 - \frac{\Omega^2}{\omega_p^2} sin^2\alpha)cos\alpha \quad \text{Eq. 7}$$

$$\omega_1{}^2 = \Omega^2(1 + \frac{\omega_p^2}{\Omega^2} sin^2\alpha) \quad \text{Eq. 8}$$

$$\omega_2{}^2 = \omega_p^2(1 - \frac{\omega_p^2}{\Omega^2} sin^2\alpha)cos\alpha \quad \text{Eq. 9}$$

Equation 7 describes the mode corresponding to the gyro resonance feature in the spectral return from the region. This wave's spectral information is influenced by electrons cyclically spiraling around magnetic field lines.

While gyro resonance and ion acoustic waveforms provide useful avenues for understanding the ionosphere, the propagating wave of interest in this thesis is the Langmuir wave. Langmuir waves describe charge density oscillations of free floating electrons in the plasma (Tonks & Langmuir, 1929). Langmuir waves, like whistler mode waves, are analytically described from the dispersion relation for electrostatic electron waves. The Langmuir wave dispersion relation in the presence of a magnetic field is given by:

$$\omega_r^2 = \omega_p^2 + \frac{3k^2KT}{m^*} \quad \text{Eq. 10}$$

where ω_r is the plasma resonance frequency, ω_p is the plasma frequency, k is the wavenumber, K is Boltzmann's constant, T is the ambient electron temperature, and m^* is the effective mass of an electron. Note that the plasma resonance frequency is dependent on the superposition of two terms. In a cold plasma, the charge density oscillates at the plasma frequency, where:

$$\omega_p = \sqrt{\frac{4\pi n_e e^2}{m^*}} \quad \text{Eq. 11}$$

In this equation, n_e is the electron density and e is the charge of an electron. However, since this thesis investigates the enhancement of Langmuir wave spectral information by photoelectron enhancement, the additional electron pressure in the system governed by thermal energy directly affects plasma resonance, thus the incorporation of the second term on the right hand side of Eq. 10.

Aside from the resonant plasma frequency, the Landau damping merits discussion, as this form of wave damping describes particle and wave energy exchange affecting particle velocities in Langmuir waves (Stix, 1962). Understanding Landau damping begins with the Maxwell-Boltzmann distribution of particle velocities in a fluid. The analytical function describing one dimensional velocity distribution of particles is Gaussian with $\mu_{v_{x,y,z}} = 0$ and $\sigma_{v_{x,y,z}} = \sqrt{\frac{kT}{m}}$. Graphically, the distribution appears as shown in Figure 3.

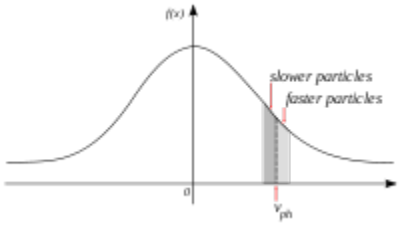

Figure 3: Maxwellian 1D Velocity Distribution with Phase Velocity.

Consider a Langmuir wave propagating through the ionosphere with phase velocity v_{ph}. Electrons traveling in the vicinity of v_{ph} will have meaningful energy exchange with the wave. If v_{ph} is greater than $\mu_{v_{x,y,z}}$, then applying symmetric tolerances of velocities to consider ($\pm \Delta v$) will show a greater number of electrons traveling slightly slower than v_{ph} than traveling slightly faster than v_{ph}. The slower moving electrons will be sped up to v_{ph}, and the faster moving electrons will be slowed to v_{ph}. This results in overall energy loss from the wave and is the driving physical principle behind Landau damping. The dependence of damping on the phase velocity delineates how this wave phenomenon is requisite for understanding electron interactions in the ionosphere.

The propagating waves within the plasma can be modeled as a circuit with internal impedance, Z_p. This load impedance due to Landau damping, while proportional to the damping decrement, is inversely proportional to the plasma resonant frequency expressed in Eq. 10 (Danielson, 2002).

2.3 Incoherent Scatter Radar

Beginning in the late 1950's, (Gordon, 1958; Bowles, 1958; Evans & Lowenthal, 1964; Salpeter, 1960; Yngvesson & Perkins, 1967), radar experiments were used to obtain ionospheric measurements. The radar range equation for volume scatterers is given by (Richards, 2005):

$$P_r = \frac{P_t G^2 \lambda^2 \eta \Delta R \theta_3 \phi_3}{(4\pi)^3 R_0^2 L_s L_a(R_0)} \quad \text{Eq. 12}$$

where P_r is the received power, G is the antenna gain, λ is the wavelength of the transmitted beam, R is the distance between the transmitted beam and the medium, $\theta_3$and $\phi_3$are angles defining the transmitted beam, and $L_s L_a(R_0)$ are two loss factors.

This relationship determines the power of the signal received given a bevy of parameters describing the transmitter, the transmitted wave itself, the properties of the target, and properties of the receiver. Of particular interest is η, which is the volume reflectivity of the scatterer. For a differential volume element, dV, the effective cross section is:

$$d\sigma = \eta dV = \eta R^2 dR d\Omega \quad \text{Eq. 13}$$

JJ Thomson (Thomson, 1906) showed that an electron will scatter electromagnetic waves, and from his work, a radar cross section can be established as the projected area of a perfect sphere scattering energy to the observer. For a single electron, the cross section is:

$$\sigma_e = 4\pi(r_e \sin\psi)^2 \quad \text{Eq. 14}$$

and the complete radar cross section of the volume is:

$$\sigma = \sigma_e \overline{\Delta N^2} P(2kl, 2km, 2kn) \quad \text{Eq. 15}$$

where r_e is the classical electron radius, ψ is the angle between the direction of the incident electric field and the observer, P(x,y,z) is a three dimensional wave-number spectrum of the density variation (a transformation of an autocorrelation function), and N is electron density (Evans, 1969). These functions define the Thomson scattering process that allows incoherent scatter radar experiments to measure meaningful information from the ionosphere.

The incoherent scatter radar spectrum is shown below in Figure 4:

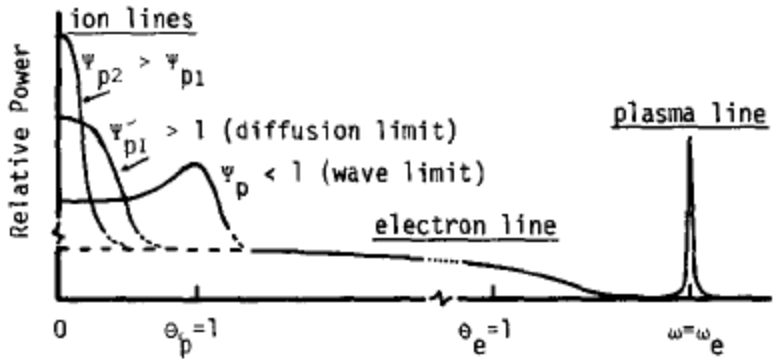

Figure 4: Schematic Representation of Features of the Thomson Scatter Power Spectrum (Mathews & Tanenbaum, 1980)

The features in the spectrum at a particular height and specific time are symmetric about a center frequency equal to the frequency of radio wave transmission. The ion line feature is the spectral component with a low Doppler shift relative to the transmitter frequency. The plasma line feature corresponds to the Langmuir wave and its dispersion relationship described previously – as ω_e is the plasma resonance frequency ω_r in Eq. 10. This feature is the focus of this thesis.

2.4 Plasma Line Background

As incoherent scatter radar has been used for decades to explain ionospheric behavior, the ion line feature has been thoroughly probed for information, while the plasma line has experienced limited attention. The integrated power of the ion line, for example, is directly proportional to the electron density of the plasma (Kelley, 2008). The same information can be obtained experimentally from the plasma line by Eq. 10 and Eq. 11. Note that only the location of the feature is required to obtain the electron density. Noisy experimental data compromise the estimate obtained from the ion line spectral component, while the electron density measurement as governed by the Langmuir wave dispersion relation is unaffected so long as the feature is displayed above the noise level. During the daytime, when the plasma line is enhanced by photoelectrons, the plasma line location is clear and electron density can be deterministically verified, rather than stochastically estimated as in the case of the ion line measurement. Incoherent scatter radar theory pertaining to the plasma line was developed in the 1960's by Evans (Evans, 1969) and Yngvesson and Perkins (Yngvesson & Perkins, 1968); their papers thoroughly investigate the possible uses of the plasma line for this research. Unfortunately, due to the meager spectral width of the plasma line component, deficiencies in sampling rate endemic to rudimentary computational resources have limited progress in experimentally verifying their conclusions. Only recently (Nichols, 2006) (Bhatt, 2008) have publications in scientific literature appeared that utilize the plasma line to obtain electron densities and temperatures.

Though Yngvesson and Perkins' paper (Yngvesson & Perkins, 1968) treats the photoelectron enhanced plasma line features theoretically, some analysis relied on the low fidelity sampled data available to validate their predictions. For example, one of the principle figures in the article shows predicted and measured KT_p values against plasma resonance frequency for two angles of the radar beam relative to the earth's magnetic field as shown in Figure 5:

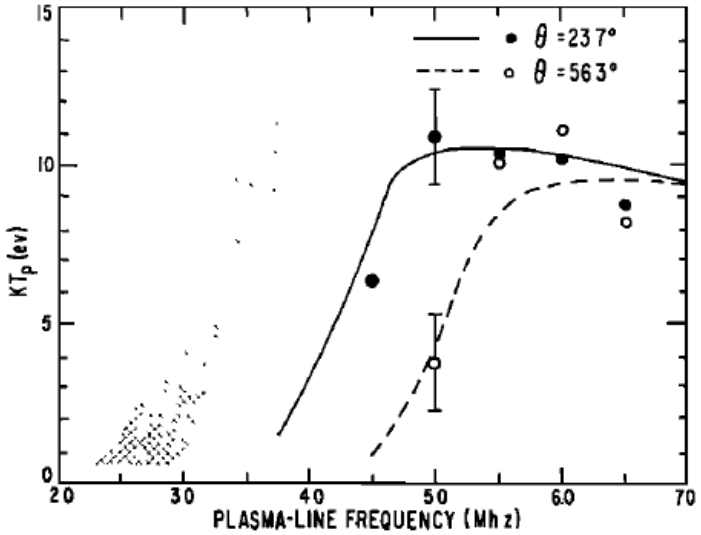

Figure 5: KT_p vs. f_r from Yngvesson and Perkins' paper (Yngvesson & Perkins, 1968).

While the measured values seem to align well with the predicted curve, the low resolution of data makes conclusive statements from the experimental comparison difficult. Chapter 3 of this thesis discusses Yngvesson and Perkins' paper in detail and concludes with a series of objectives that entail reproducing their theoretical results and using recent, high resolution measurements to verify and update the body of plasma line theory.

The experimental data previously alluded to was taken at Arecibo's Radio Observatory in Puerto Rico from January 15th through January 17th, 2010. Chapter 4 of this thesis describes the procedure and setup of the dual beam incoherent scatter radar experiment. Chapter 5 covers signal processing of the radio frequency waves, as remote sensing and detection of ionospheric phenomena requires processing to improve the signal to noise ratio so that measurements are useful. That chapter begins with a system level overview of the incoherent scatter radar process, and entails discussion on radio wave transmission and encoding, target scattering, scattered energy reception, signal decoding, and post processing filtering techniques on the data. Of particular interest are the opportunities to derive electron density, electron temperature, and electron velocity distributions using this dataset. Other anomalous features of the data are displayed as well. All discussions in Chapter 5 are with respect to the experiment described in Chapter 4.

Chapter 6 contains an investigation of signal processing methods used in an effort to cleanly extract the most useful plasma line features; plasma line resonant frequency, peak intensity, and spectral width. Chapter 7 studies the results of the post-processing and looks at physical explanations for the features observed. Chapter 8 concludes the thesis and offers suggestions for future development in using the plasma line spectral component to facilitate understanding of the Earth's ionosphere.

3. Previous Incoherent Scatter Radar Studies

While several authors independently developed incoherent scatter approaches to studying ionospheric plasma yielding equivalent results (Dougherty & Farley, 1960; Fejer, 1960; Salpeter, 1960; Hagfors, 1960; Woodman, 1967), this thesis's theoretical objectives begin with Salpeter's (Salpeter, 1960) decomposition of the power spectra of Thomson backscatter into the observed features of interest (see Figure 4). Yngvesson and Perkins' paper advances this frontier by studying properties of the photoelectrons through a mixture of theoretical physics derivation and experimental analysis (1967).

3.1 Theoretical Plasma Line From Wave/Particle Interactions

Since the Langmuir waves that govern the plasma line are dependent on the electron velocity distribution in the immediate vicinity of the phase velocity, salient features of the plasma line are, too, dependent on velocity distribution limits near the phase velocity defined as:

$$v_\phi = \mp\frac{\nu_r\lambda}{2};\ \nu_r = 2\pi\omega_r \qquad \text{Eq. 16}$$

In order to study the effect of photoelectrons on the Langmuir waves, the electron energies for electron velocity distributions as a function of v_φ are considered, since:

$$E_\phi = \frac{1}{2}mv_\phi^2 = \frac{1}{8}mf_r^2\lambda^2 \qquad \text{Eq. 17}$$

The solar accelerated electrons will dump energy into the Langmuir waves proportional to the one dimensional velocity distribution as a function of the phase velocity as demonstrated graphically in Figure 3. Landau damping complimentarily removes energy from the wave in proportion with the partial derivative of the velocity distribution function with respect to the

phase velocity. Consider the one dimensional Maxwell-Boltzmann distribution for the velocity vector (Knight, 2004):

$$f_v(v_i) = \sqrt{\frac{m}{2\pi kT}} e^{-\frac{mv_\phi^2}{2kT}} \quad \text{Eq. 18}$$

The steady state particle distribution for a plasma wave oscillating at a particular v_φ can be analytically derived to form Equation 19, which is suitable for describing ionospheric phenomena ignoring collisions and magnetic field effects:

$$\frac{mv_\varphi}{KT_\varphi(v_\varphi)} = -[\frac{\delta}{\delta v_\varphi} \ln f(v_\varphi)] \quad \text{Eq. 19}$$

Prior research (Perkins & Salpeter, 1965) incorporated the effect of electron-ion collisions in terms of the intensity, I_p, of Thomson backscatter radiation into one of the two quasisymmetric plasma lines that appear in the incoherent scatter spectrum. I_p are measured relative to the noise level, the expected intensity of radiation scattered by the same volume with no interaction effects as shown in Equation 20:

$$I_p = \frac{2\pi KT_p(v_\phi)}{\lambda^2 ne^2} \quad \text{Eq. 20}$$

The velocity dependent temperature, as expressed, can be understood in a simpler form vis-à-vis the Zeroth law of thermodynamics, where the relationship between kinetic energy and thermal energy is framed by the ideal gas law. In the more complex isotropic plasma Perkins and Salpeter (1965) considered, the velocity dependent temperature is expressed as:

$$T_p(v_\varphi) = T \frac{f_m(v_\varphi) + f_p(v_\varphi) + \chi}{f_m(v_\varphi) - KT\frac{d}{dE_\varphi} f_p(v_\varphi) + \chi} \quad \text{Eq. 21}$$

where:

$$f_m(v_\varphi) = n\sqrt{\frac{m}{2\pi KT}} e^{-\frac{mv_\varphi^2}{2KT}} \quad \text{Eq. 22}$$

$$f_p(E_\varphi) = \int_{E_\varphi}^{\infty} \sqrt{\frac{m}{8E}} \rho(E) dE \quad \text{Eq. 23}$$

and:

$$\chi = \frac{32\pi}{3\lambda^3} \sqrt{\frac{m}{2\pi KT}} \ln(4\pi n D^3) \quad \text{Eq. 24}$$

In these formulae, f_m is the Maxwellian contribution to one dimensional electron velocity distribution of the electrons in the scattering volume as governed by Equation 18, f_p is the

photoelectron contribution to the same distribution, $\rho(E)$ is the number of photoelectrons per unit volume-energy – a variable experimentally determined from the given parameters, and χ describes the dynamics of the Langmuir waves, removing the assumption implied by Equation 19.

Inclusion of geomagnetic field effects and anisotropic photoelectron velocity distributions only require f_m to be modified. This modification is (Salpeter, 1961):

$$f_m = n\sqrt{\frac{m}{2\pi KT}}\sum_{n=-\infty}^{\infty}\frac{e^{-bsin^2\theta}}{\cos\theta}I_n(bsin^2\theta)\,e^{\left(-\frac{(y-n)^2}{2bcos^2\theta}\right)} \quad \text{Eq. 25}$$

where y is the ratio of plasma resonance frequency to electron gyrofrequency, θ is the aspect angle between the radar beam and the magnetic field, and I_n is the Bessel function of imaginary argument describing gyro motion of electrons around magnetic field lines.

The magnetic field does not affect collisions when the Debye length, D, is less than the electron gyroradius, f_c, a criterion fulfilled for the plasma line component, as shown in Equations 6 and 10. Moreover, photoelectron contributions are unaltered since the gyroradius is much larger than the wave number associated with Thomson backscatter. This limit is fulfilled for the same case where Equation 6 applies. Photoelectron anisotropy is accounted for if the requisite f_p pertains to the contribution of photoelectrons to the distribution along the direction vector of the transmitted radar beam. Asymmetry in the upshifted and downshifted peak plasma intensities arises that conveys information about the bulk flow of photoelectrons as governed by Equations 16 and 17.

Just as the plasma line intensity theory must be adapted to include geomagnetic effects, the dispersion relation describing the plasma resonance frequency must subsequently be amended from Equation 10 to produce:

$$\nu_r^2 = \nu_p^2 + \frac{12KT}{\lambda^2 m} + \nu_c^2 \sin^2\theta \quad \text{Eq. 26}$$

The additional term demonstrates dependence of plasma resonance on the angle between the transmitted radio wave and the magnetic field. Yngvesson and Perkins (1968) graphically demonstrated the impact of varying wavelengths and aspect angles on plasma line intensity against plasma frequency as shown in Figure 6:

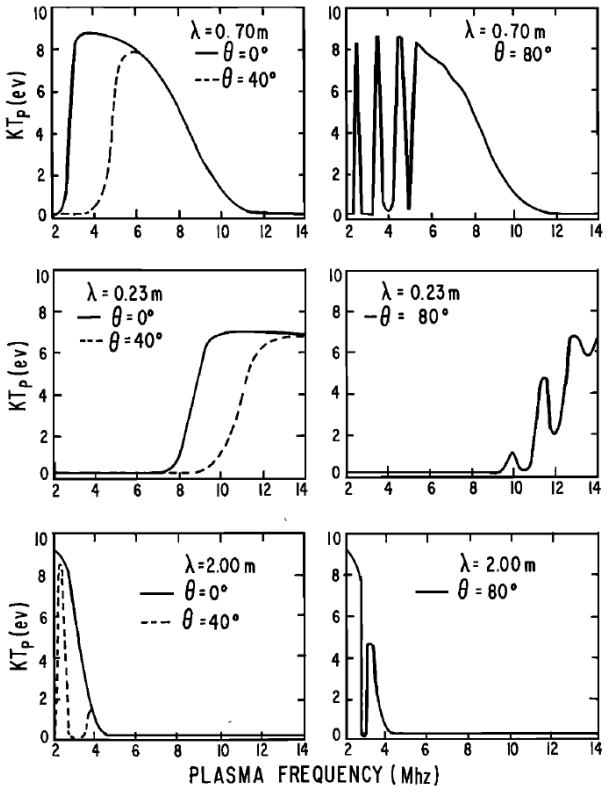

Figure 6: Plasma Line Intensity vs. Plasma Resonant Frequency.

3.2 Experimental Plasma Line from Incoherent Scatter Radar Analysis

Yngvesson and Perkins sought to experimentally verify KT_p measurements as a function of plasma line frequency, ν_p (1967). Radar range equations of the general form provided in Equation 12 were constructed to obtain received plasma line power (Equation 27) and received ion line power (Equation 28):

$$P_r^{(p)} = \frac{P_t \sigma}{h^2}\left(\frac{2\pi K T_p}{\lambda^2 e^2}\right)\left(\frac{2HB_p}{\nu_p}\right)A(\nu) \qquad \text{Eq. 27}$$

$$P_r^{(i)} = \frac{P_t \sigma n c \Delta A(0)}{2h^2\left(1+\frac{T}{T_i}\right)} \qquad \text{Eq. 28}$$

The quotient of these two equations allows an experimentally obtainable expression for KT_p to be obtained as shown in Equation 29:

$$KT_p = \left(\frac{T_A^{(p)}}{T_A^{(i)}}\right)\frac{\lambda^2 e^2 n \nu_p c \Delta}{8\pi\left(1+\frac{T}{T_i}\right)HB_i}\left[\frac{A(0)}{A(\nu)}\right] \qquad \text{Eq. 29}$$

where λ, Δ, B_i, and $\frac{A(0)}{A(\nu)}$ are obtained from the equipment, and n, ν_p, H, and $\frac{T_A^{(p)}}{T_A^{(i)}}$ are determined through simultaneous measurement of the ion line and plasma line spectral components endemic to the complete incoherent scatter spectrum. Of the equipment variables, only $\frac{A(0)}{A(\nu)}$ is not constant, as it is dependent on the frequency modulation of the signal in transit.

By applying Equation 29 to measured incoherent scatter information gathered from the topside ionosphere, Yngvesson and Perkins obtained Figure 7:

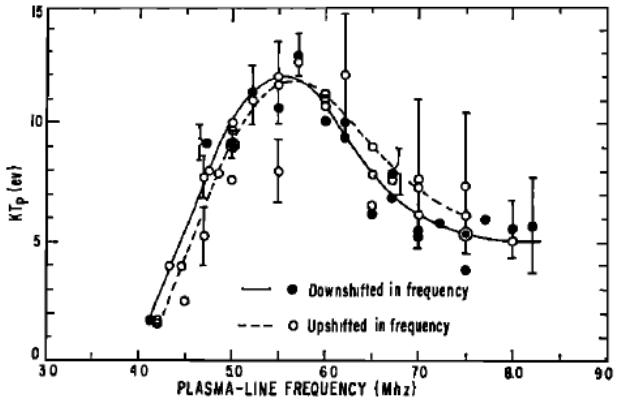

Figure 7: Measured KT_p Values Against ν_p With Corresponding Regression Curves.

Using the regression curves generated on this plot, the photoelectron velocity distribution for a single dimension (f_p) was obtained in accordance with Equation 21. Their formulation (Equation 30) is applied for the duration of their analyses for all altitudes:

$$f_p(E_\varphi) = f_{p1} e^{-\int_{E_1}^{E_\varphi} \frac{dE'}{KT_p(E')}} + \int_{E_1}^{E_\varphi} \left\{ e^{-\int_{E'}^{E_\varphi} \frac{dE''}{KT_p(E'')}} \right\} \left[\frac{1}{KT(E')} - \frac{1}{KT_p(E')} \right] [f_m(E') + \chi(E')] dE' \quad \text{Eq. 30}$$

A contemporary update to this derivation allows for a more robust version of Figure 7 to be generated, as current datasets contain the plasma line component of the spectrum at high frequency and altitude resolutions for a wide altitude range. Species densities and dissociative recombination rates (Kelley, 2008) stratify the ionosphere into the layers mentioned in Chapter 2, Section B, and can be seen via visual comparison of Figures 1 and 8:

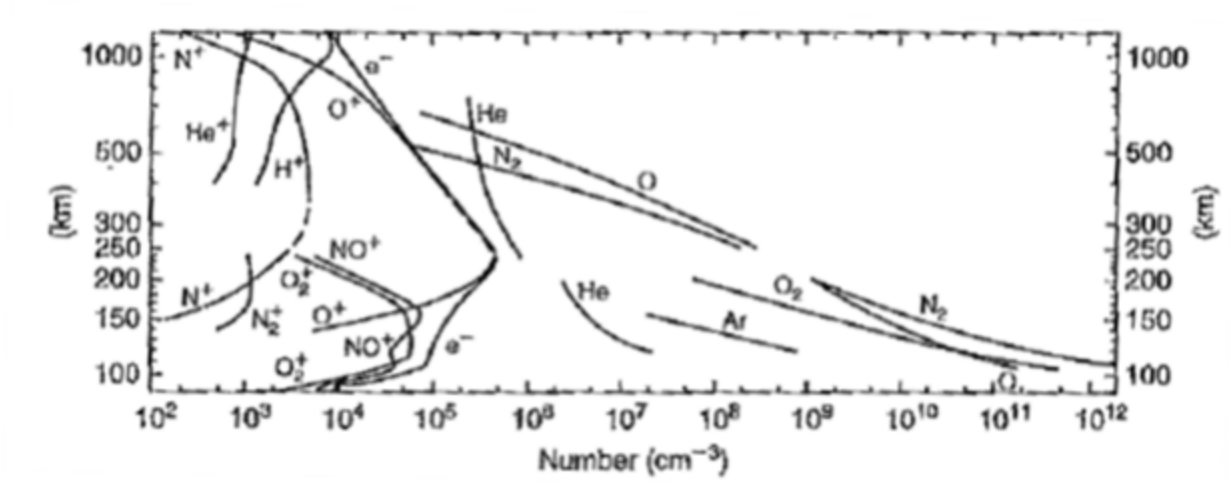

Figure 8: Daytime Atmospheric Composition from Mass Spectrometer Measurements above White Sands, NM (Kelley, 2008).

Following the same approach Yngvesson and Perkins used to obtain the photoelectron contribution to the electron velocity distribution should yield more thorough results (1967). Understanding the experimental photoelectron velocity distribution serves as a springboard for modeling the complete three dimensional electron velocity distribution, F(**v**), using Equations 31 and 32, displayed in Figure 9:

$$F(\boldsymbol{v}) = \begin{cases} F^{+}(|\boldsymbol{v}|^2)\cos\alpha & 0 < \cos\alpha < 1 \\ F^{-}(|\boldsymbol{v}|^2)\cos\alpha & 0 < \cos\alpha < 1 \end{cases} \quad \text{Eq. 31}$$

$$f_p^{\pm}(E_\varphi) = 2\pi\cos\theta \mid v_\varphi \mid \int_{|v_\varphi|}^{\infty} dv\, F^{\pm}(|\boldsymbol{v}|^2) \quad \text{Eq. 32}$$

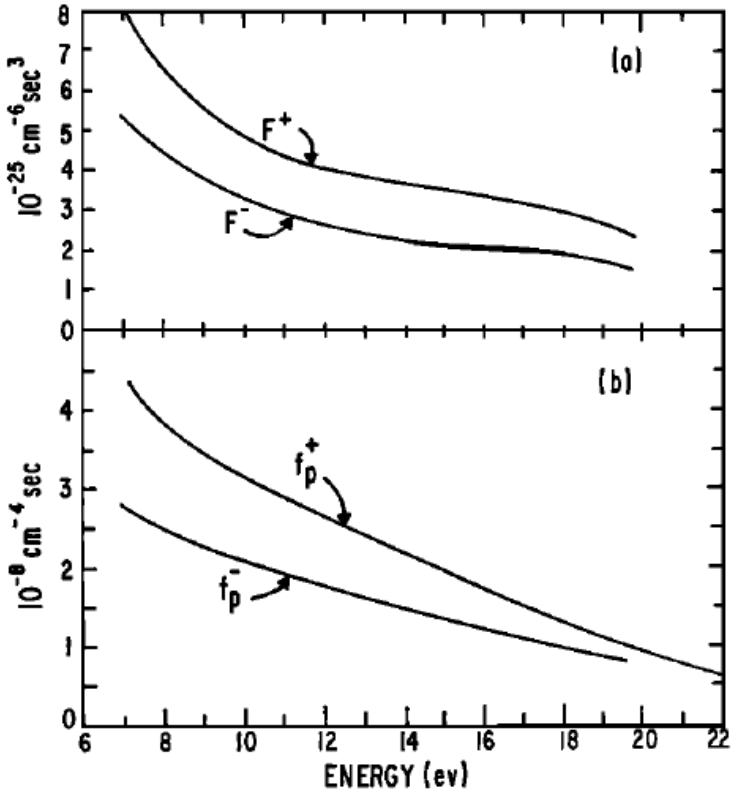

Figure 9: Velocity Distributions in Three Dimensions (a) and One Dimension (b) (Yngvesson & Perkins, 1968).

From the electron velocity distribution, moments can be computed to determine photoelectron energy fluxes and particle fluxes. Though Yngvesson and Perkins obtained fluxes for the topside ionosphere photoelectrons escaping into space – this thesis demonstrates a plan for using similar methodology to produce energy and particle fluxes for photoelectrons in a much larger region of the ionosphere.

3.3 Landau Damping's Effect on Plasma Line Backscatter in a Weakly Ionized Plasma

Salpeter (Salpeter, 1961) derived the generalized Landau damping coefficient that includes magnetic field effects as shown in Equation 33:

$$\gamma_B = \omega_p \sqrt{\frac{\pi}{8}} \alpha^3 \sum_{n=-\infty}^{\infty} \frac{e^{-b\sin^2\theta}}{\cos\theta} I_n(b\sin^2\theta) e^{-\frac{(y-n)^2}{2b\cos^2\theta}} \quad \text{Eq. 33}$$

where $\alpha = \lambda/(4\pi D)$, $b = q^2KT/m\omega_c^2$, and $y = \nu_r/\nu_c$.

When the aspect angle, θ, is 90 degrees with respect to the magnetic field, Landau damping is not observed (Bernstein, 1958). Additionally, when θ is 0 degrees, Landau damping for an unmagnetized plasma is obtained as (Landau, 1946; Stix, 1962):

$$\gamma_0 = \omega_p \sqrt{\frac{\pi}{8}} \alpha^3 e^{\left(-\frac{m v_\varphi^2}{2KT}\right)} \quad \text{Eq. 34}$$

If $b \leq 1$, all terms of the summation are ignored except when n is closest to y, and as Equation 35 shows, the Landau damping coefficient is then inversely proportional to the cosine of the aspect angle between the transmitted radar beam and the magnetic field (Yngvesson & Perkins, 1967):

$$\gamma_B \sim \omega_p \sqrt{\frac{\pi}{8}} \alpha^3 \left(\frac{b \sin^2\theta}{2}\right)^y \frac{1}{y! \cos\theta} \quad \text{Eq. 35}$$

By comparing Equations 33 and 35, an expression is obtained for an intermediate aspect angle where the Landau damping is the same for the magnetized and unmagnetized cases (Yngvesson and Perkins, 1967):

$$\theta_0 \sim \sqrt{\frac{y}{b}} e^{-\frac{y}{4b}} \quad \text{Eq. 36}$$

Yngvesson and Perkins used experimental data to measure onset of nonthermal effects as a function of the aspect angle and verify the Landau damping field free derivations from these measurements as was shown in Figure 1.

Though the data seemed to corroborate well with predicted results, there is not much of the data available to display. Modern plasma line data should provide more complete information that either reinforces Yngvesson and Perkins' derivation or identifies anomalous features that require further study.

4. Experimental Techniques and Setup

The experimental data used in this thesis was collected at Arecibo Radio Observatory. Results in chapters 5 through 7 were generated using data collected from January 16th through January 18th in 2010. Though a dual beam setup was used, the plasma line data available comes from only the Gregorian feed, pointed 15° off zenith. The beam rotated periodically throughout the 3 days' data collection, a phenomenon studied in greater detail in Chapter 5. The transmitted frequency of the radio waves was 430 MHz, and the plasma line component of the measurement is contained within a 5 MHz range between 3 and 8 MHz symmetrically displaced from the center frequency. High resolution measurements were obtained using Sulzer's Coded Long Pulse (CLP) technique (Sulzer, 1986). The CLP waveform permits high resolution range measurements in tandem with high signal-to-noise ratio (SNR). An example binary phase coded waveform is shown below in Figure 10:

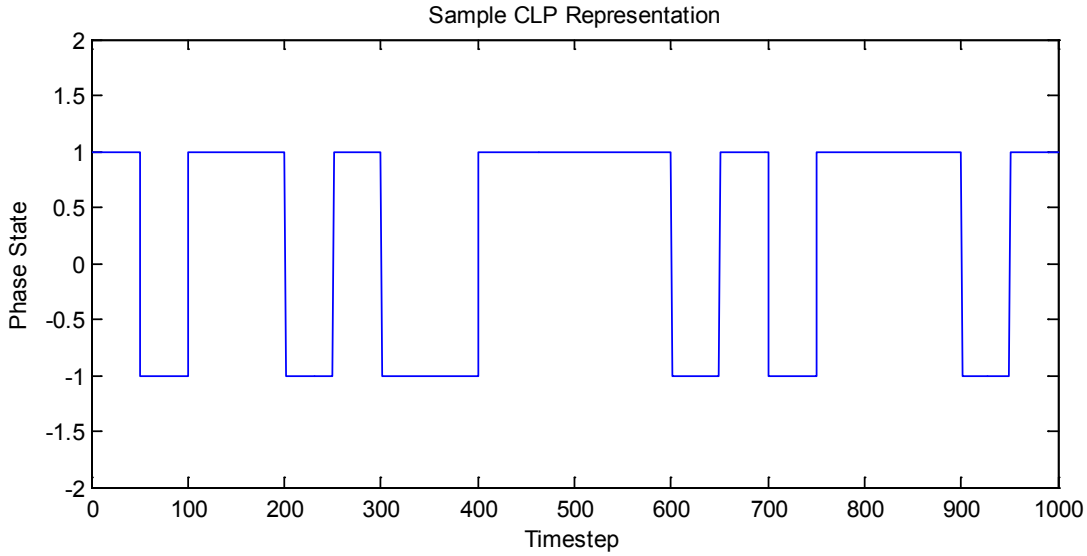

Figure 10: Coded Long Pulse Envelope.

For this experiment, the transmitted pulse length, τ, is 400 μsec., and the chip length is 2 μsec. Since CLP incorporates binary phase shifts, the phase state of the code has a 0.5 chance of changing at each epoch corresponding to an integer multiple of the chip length. This stochastic feature verifies that lag products of the original code are uncorrelated. Figure 11 (Sulzer, 1986)

shows how the superposition of returned signals from different heights will appear at the receiver:

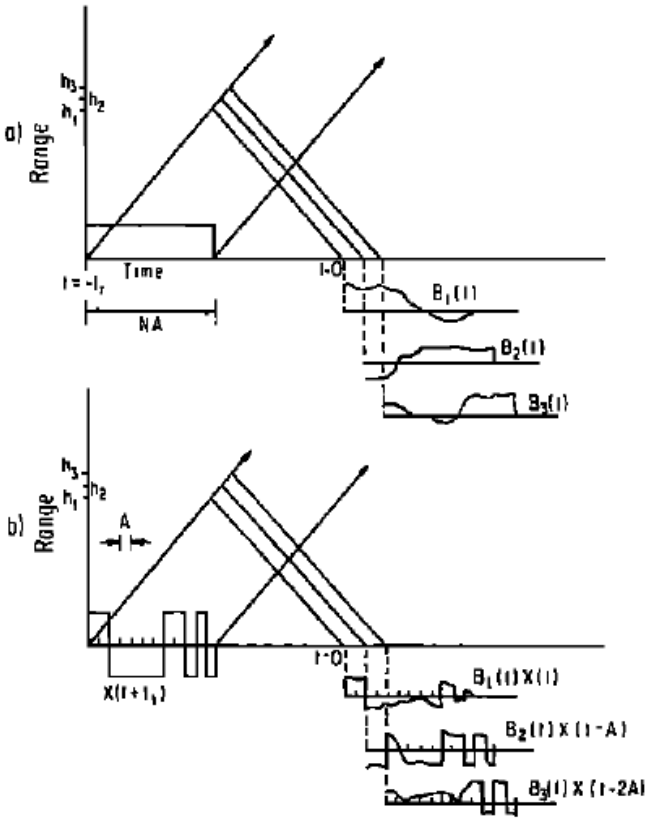

Figure 11: Range-Time Diagrams Displaying the Observed Return Signal with (a) an uncoded pulse and (b) a CLP (Sulzer, 1986).

By computing the lag products of the returned signal with respect to the original code over many interpulse periods, we can recover the returned signal corresponding to a range dictated by the lag of the current product, since all other returns from different ranges at that lag will not correlate. For this dataset, the range resolution is given by:

$$R = \frac{n_{skip}}{f_{range}} \frac{c}{2} \quad \text{Eq. 37}$$

where c is the speed of light, n_{skip} is the number of skipped heights (6) between data points, and f_{range} is the spectral range of measurement (5 MHz). Each time integration has 2250 height bins; applying the vector of height bins to Eq. 38 (direction cosine projection of Eq. 37 with the added

gate delay, τ_{gd} = 600 μsec., given the Gregorian feed angle off zenith) allows us to obtain the complete range of heights available for the data, as:

$$\boldsymbol{R} = \left[\tau_{gd} + \frac{\vec{\imath}_{ht} n_{skip}}{f_{range}}\right] \frac{c}{2} * \cos(15°) \qquad \text{Eq. 38}$$

Figures 12 and 13 were generated as a single temporal slice of data containing information for all available heights and all available frequencies. Comparison with the salient features of the electron density theoretical curves available in Figures 1 and 2 demonstrates some dependence of plasma resonance features on plasma density in the region (analytically expressed through Equations 11 and 26).

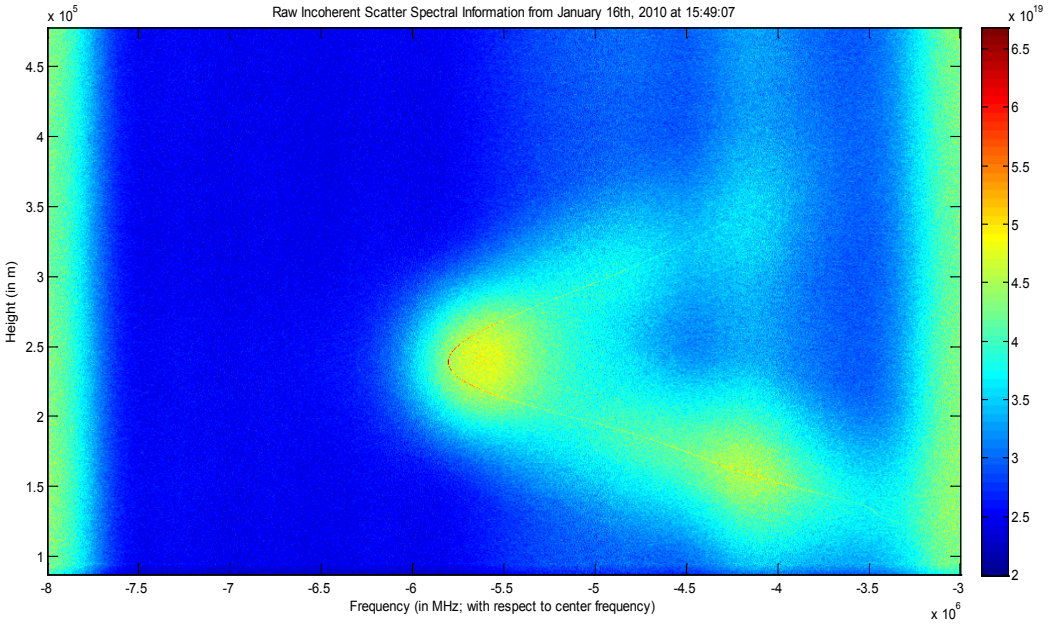

Figure 12: Decoded Received Downshifted Signal Spectra.

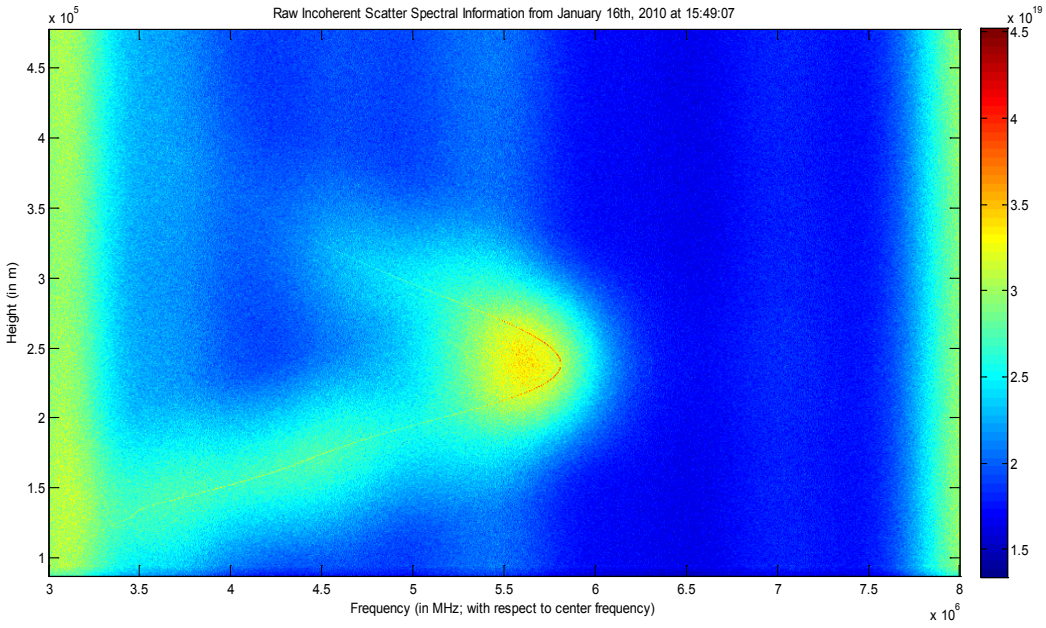

Figure 13: Decoded Received Upshifted Signal Spectra.

These matrices are both the end result of the processing done at Arecibo Radio Observatory and provide the information requisite to replicate and update existing plasma line theory as discussed in Chapter 3. Data logistic information is available in Table 1 below:

Table 1: Experimental Data Logistics

Date (in 2010)	Data Collection Start Time	Data Collection End Time	Number of Temporal Integrations
January 15th	16:21:30	20:00:57	1095
January 16th	4:58:12	20:01:08	4257
January 17th	4:59:57	20:01:12	4493

5. Initial Results

5.1 Resolving Rotating Beam Spectral Smearing

Of interest in processing these data are the plasma line frequency location (giving the plasma resonance frequency) and the plasma line intensity (a function of phase velocity dependent temperature as expressed in Equation 23). Chapter 4 mentions that the radar beam rotated during this experiment. Because the plasma resonance frequency is dependent on the aspect angle between the beam and the geomagnetic field (Equation 26), we analytically derive

$$\frac{dv_r}{d\alpha} = \frac{v_c^2 \sin\alpha \cos\alpha d\alpha}{v_r} \quad \text{Eq. 39}$$

to confirm that the speed of rotation never provides a change in frequency over aspect angle larger than the frequency resolution of the dataset. Otherwise, the plasma resonance frequency will be smeared across multiple frequency bins, deteriorating the integrity of the data. This derivative is still angle-dependent, so Table 2 below summarizes the data for all available days.

Table 2: Rotating Beam Summary Table

Angle Data Coverage for January 15th	Angle Data Coverage for January 16th	Angle Data Coverage for January 17th	Maximum Allowable $\sin\alpha \cos\alpha \, d\alpha$	Maximum Actual $\sin\alpha \cos\alpha \, d\alpha$
16:21:22-20:00:58	4:58:19-20:01:35	4:59:56-20:01:23	0.3856	0.2506

The maximum allowable value refers to the threshold where the spectral smear is equivalent to the frequency resolution. Though maximum experimental change in frequency with respect to angle never exceeds the maximum allowable value as governed by other experimental parameters, the spectral width is still broadened by the rotating beam.

5.2 Noise Removal Using Frequency Analysis

Compressing the frequency location and intensity established from each height of measurement over the course of an entire day yields the results in Figures 14 and 15. The plasma line resonant frequency is the frequency location within the bandwidth of the received information where the maximum uncalibrated plasma line information is recovered. Note that

the temporal spacing between matrices is uneven, so temporal interpolation was utilized to present the data appropriately.

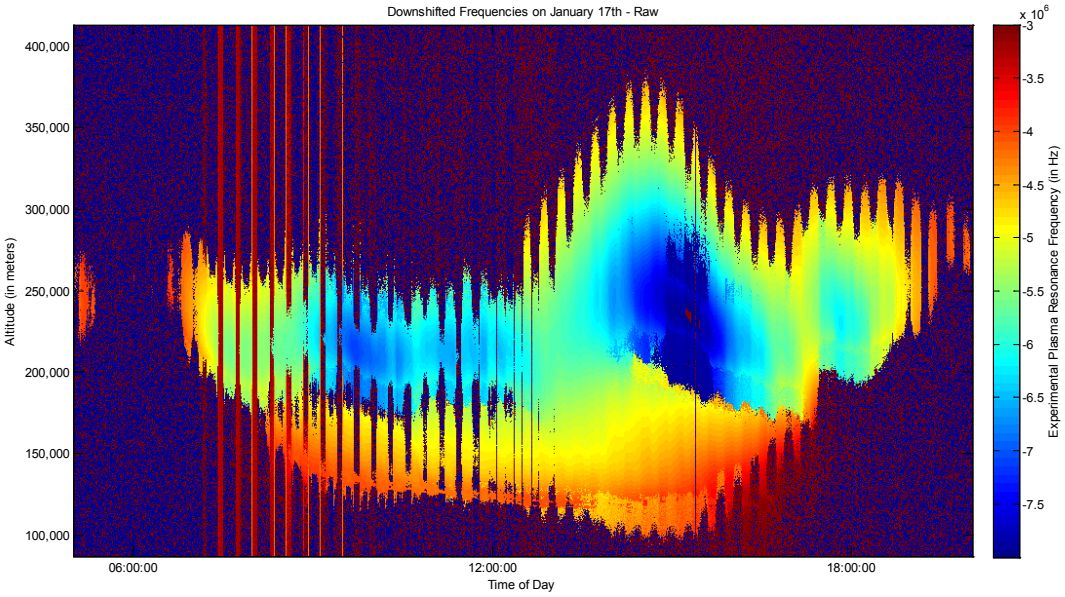

Figure 14: Downshifted Raw Plasma Resonance Frequencies for January 17th, 2010.

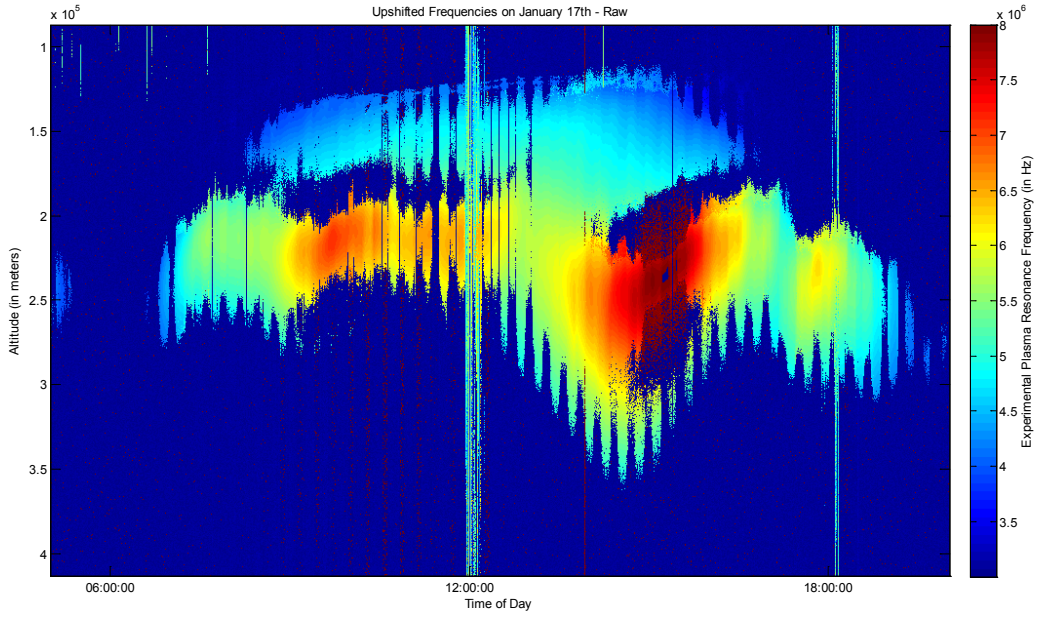

Figure 15: Upshifted Raw Plasma Resonance Frequencies for January 17th, 2010.

Figures 14 and 15 show unfiltered plasma resonance frequency data from January 17th, where noise obscures plasma resonance features. Noise in the information from a complete day can be observed in several ways; at 12:00 LT in Figure 15, there is a solid stripe of noise that shows faux plasma line enhancement independent of height. This sort of noise is easily removable. Additionally, there is noise at the lower limits of the frequency range in Figure 15, as evidenced by the large dark blue spots in the middle of the data. Two approaches have been used to remove the noise, initially. Consider Figures 12 and 13, where by visual inspection, noise can be observed at the frequency limits of the dataset. Generating a histogram of the frequency information contained in Figure 14 allows for isolation of the high and low frequency noise. Using the local minima provided by the noise peak decay evident in Figure 16, processed images that use those local minima to define a frequency band to search for plasma line information in can be generated as shown in Figures 17, 18, and 19.

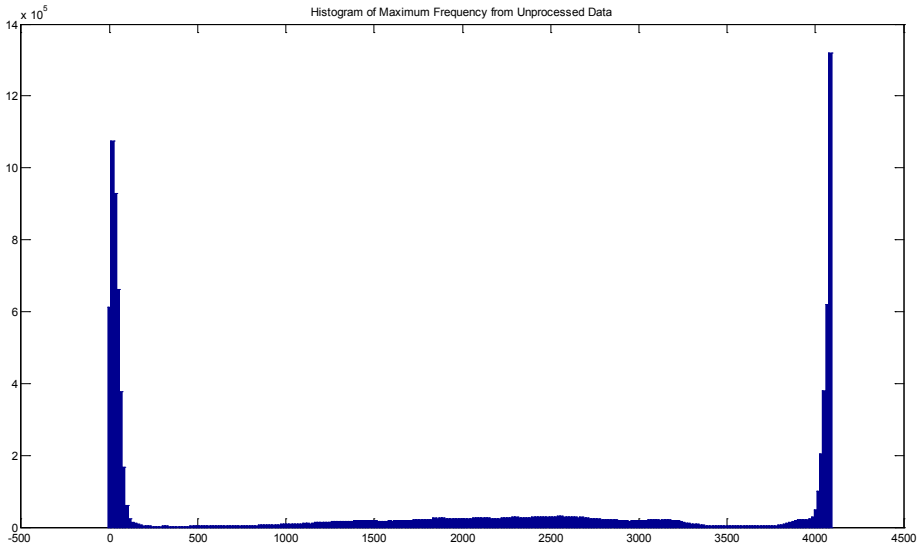

Figure 16: Histogram Frequency Information from January 17th, 2010.

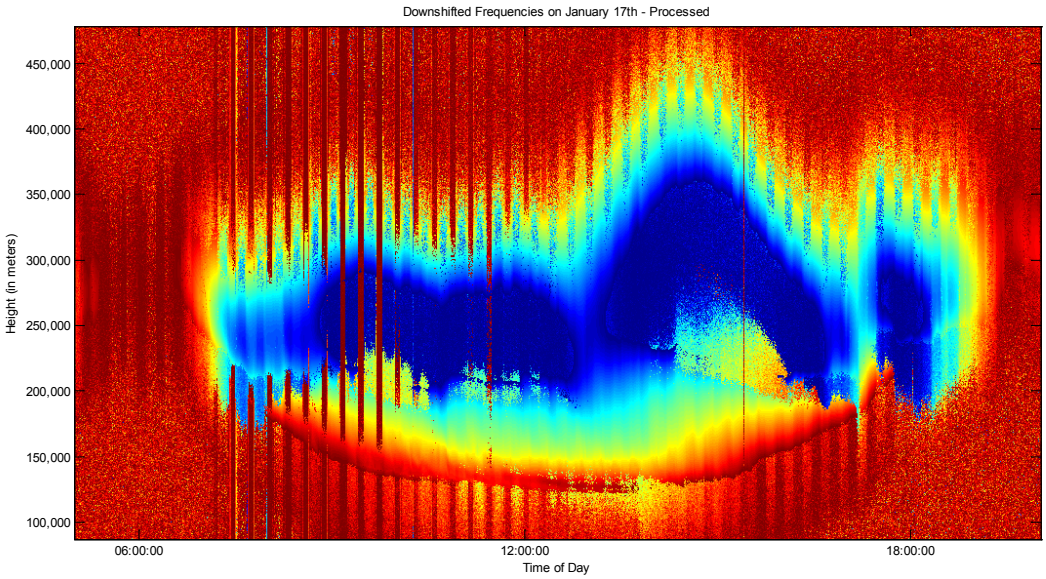

Figure 17: Downshifted Processed Plasma Resonance Frequencies for January 17th, 2010.

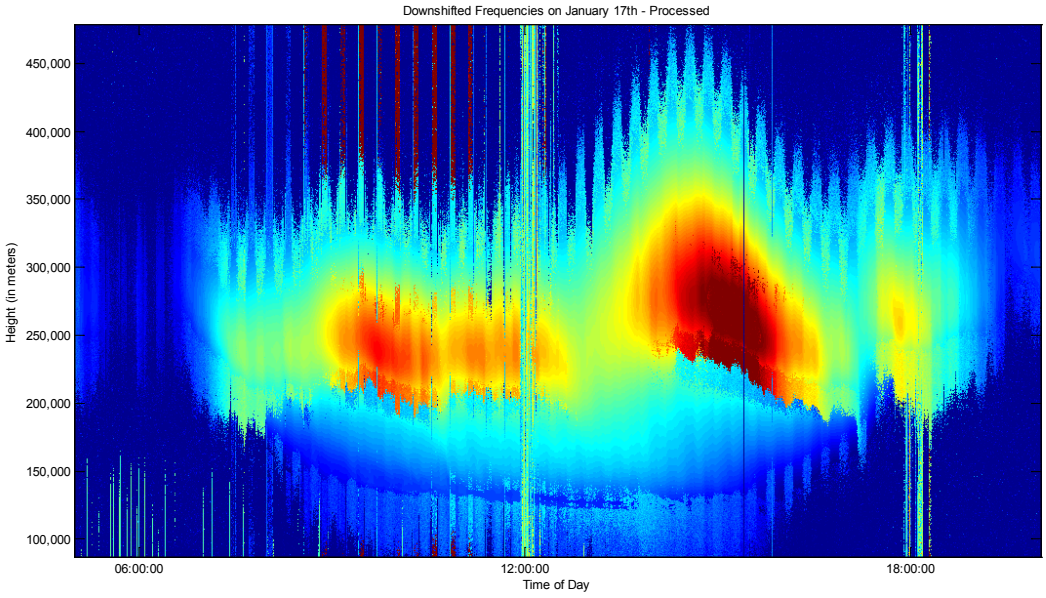

Figure 18: Upshifted Processed Plasma Resonance Frequencies for January 17th, 2010.

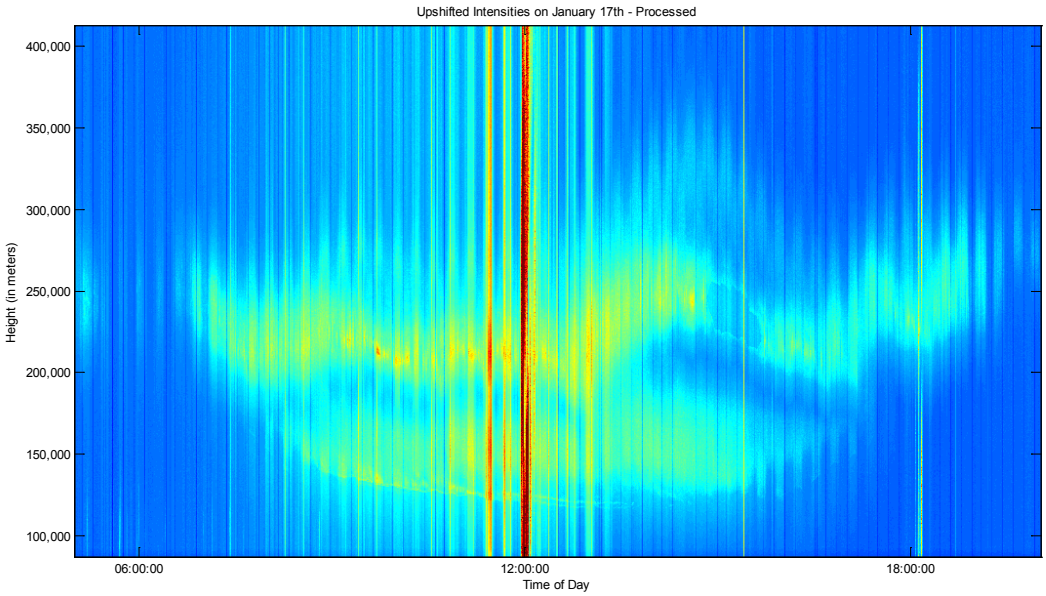

Figure 19: Upshifted Processed Plasma Line Intensities (I_p) for January 17th, 2010.

Figure 20 demonstrates an interference band that lies in an intermediate frequency range. For these cases, a statistical average of the noise level is obtained for the heights where no meaningful plasma line information exists, and the noise level is subtracted from the data, as is shown by comparison of Figures 21 and 22.

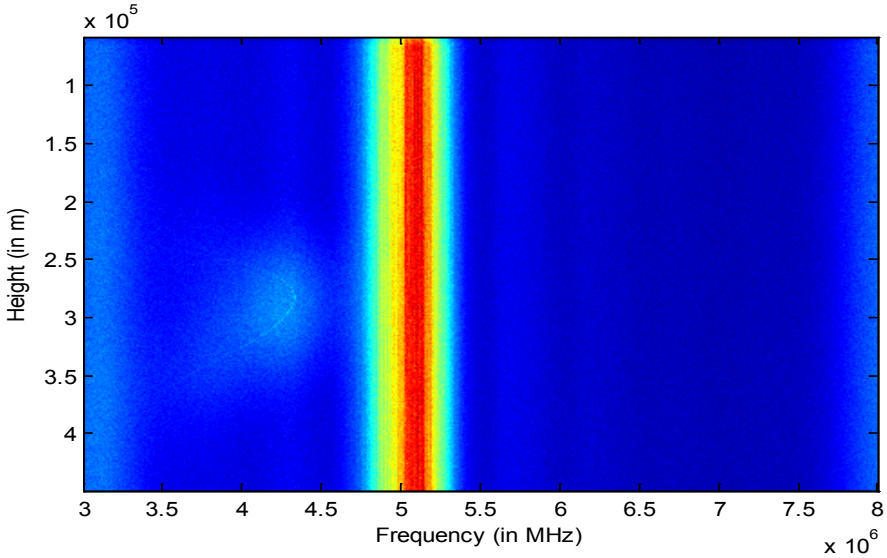

Figure 20: Interference Band in Plasma Line Data.

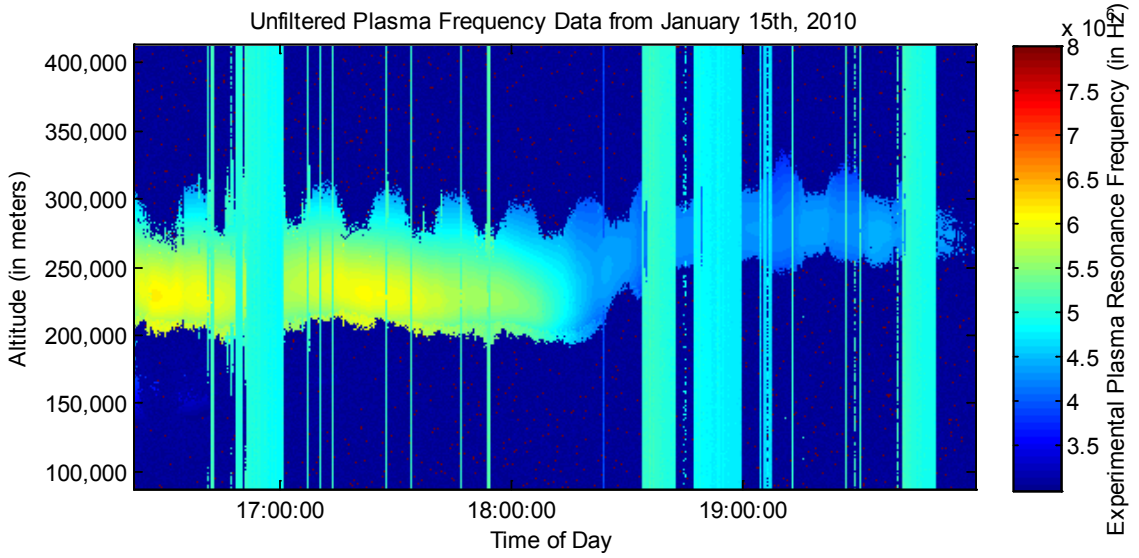

Figure 21: Unfiltered Plasma Line Frequency Data from Jan. 15th, 2010.

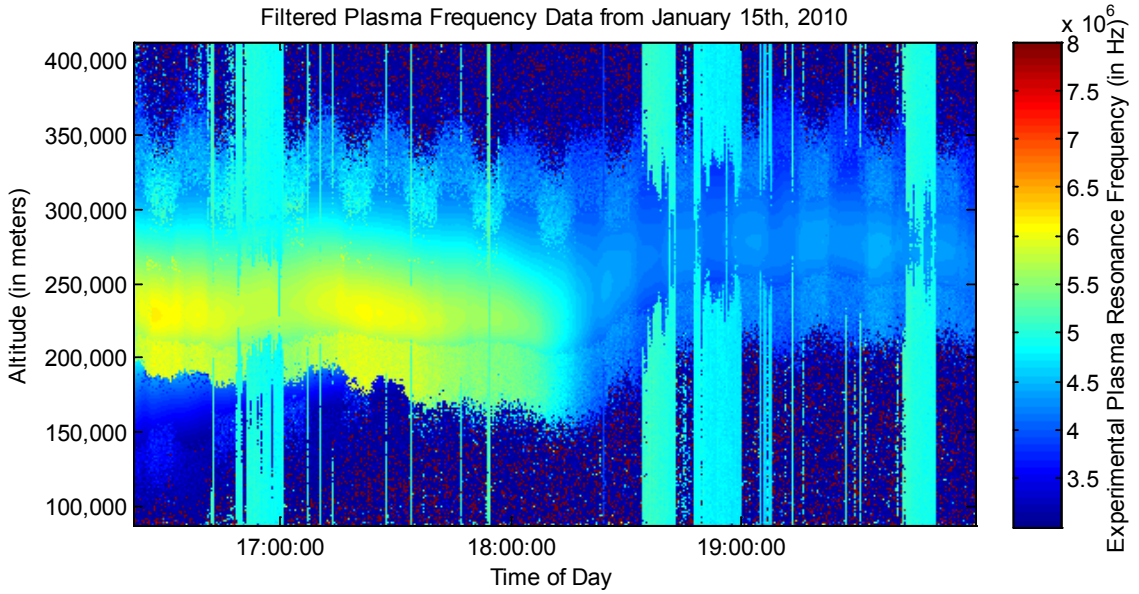

Figure 22: Filtered Plasma Line Frequency Data from Jan. 15th, 2010.

5.3 Salient Features of the Processed Data

This high resolution data requires further processing to eliminate noise, particularly with respect to the plasma intensity. However, already evident features of note include the periodic altitude oscillations. However, since Equation 26 establishes that plasma resonance is a function of aspect angle, and the beam is rotating during this experiment, the angular motion may correspond to the horizontal inhomogeneity.

Additionally, there appears to be some photoelectron enhanced plasma line activity well before the sun rose and after it fell when data was taken over Arecibo. Assessing the dip of the horizon provides Equation 40 to dictate the angle, in radians, between the surface point below the ionosphere and the effective surface point at that altitude where h is the altitude, R is the earth's radius, and d_g is the angle:

$$\cos d_g = \frac{R}{R+h} \qquad \text{Eq. 40}$$

At higher measurement heights, this projects the dip of the horizon to require nearly 20 degrees of adjustment for the altitude. Therefore, though the sun rose and set at 06:02 and 17:12, respectively, using Eq. 40, we expect highest heights of the ionosphere to be sunlit from 04:42 until 18:32. However, there appears to be plasma resonance features until the data collection stopped at 20:00, well after the sun's rays intercept the plasma. This information will be further assessed for ionospheric conjugate point photoelectron activity per prior literature observing this phenomenon (Carlson, 1966).

6. Plasma Line Extraction Techniques

6.1 Data Processing

In post-processing the plasma line data, the objective is to cleanly extract the plasma line maximum intensity, the frequency location of the maximum intensity, and the spectral width of the enhanced plasma line above the noise level. As these three features allow the plasma line to be approximated through statistical estimation, obtaining high resolution estimates of these parameters from the experimental data become the primary objective.

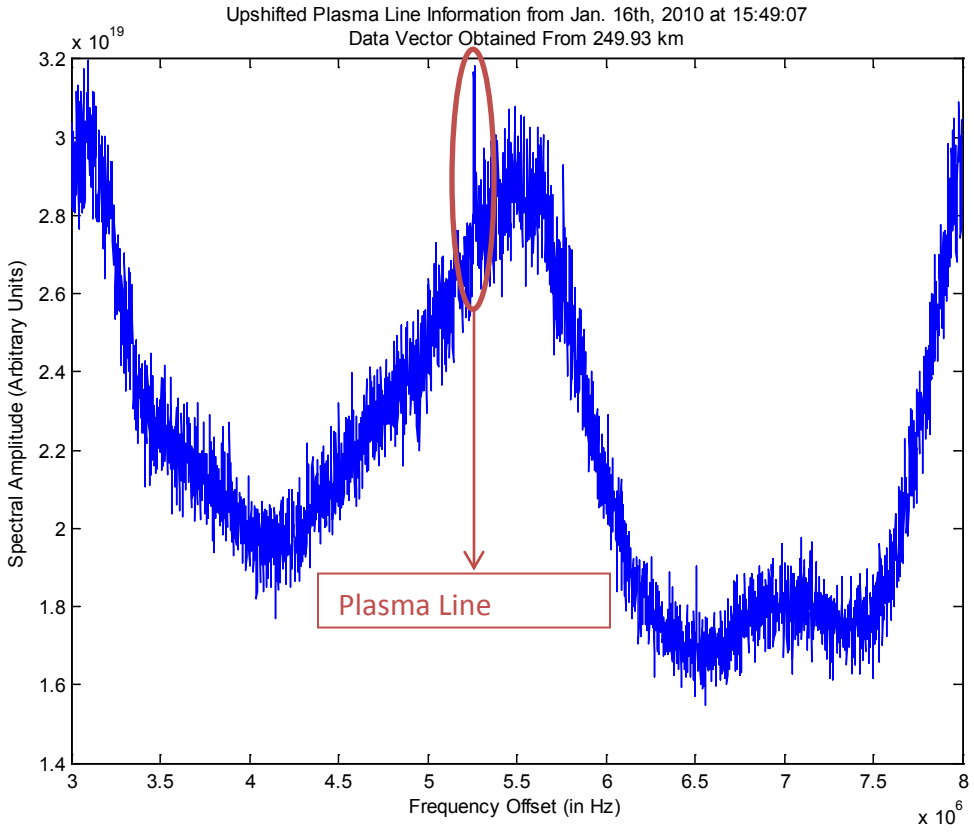

Figure 23: Unfiltered, Raw Plasma Line Information at One Time and Height.

As shown in Figure 23, a slice of the data displaying the plasma line enhancement across the entire frequency bandwidth at a particular time and height contains three primary features. The baseline noise level and clutter hump are both coarsely distributed across the bandwidth of the receiver, but the enhanced plasma line above the noise level contains the salient characteristics requisite to study the physical phenomena of the plasma. Where possible,

detrending baseline noise and clutter permits cleaner extraction of the features of interest. The first signal processing methods applied to the data in post processing are conducted with this in mind.

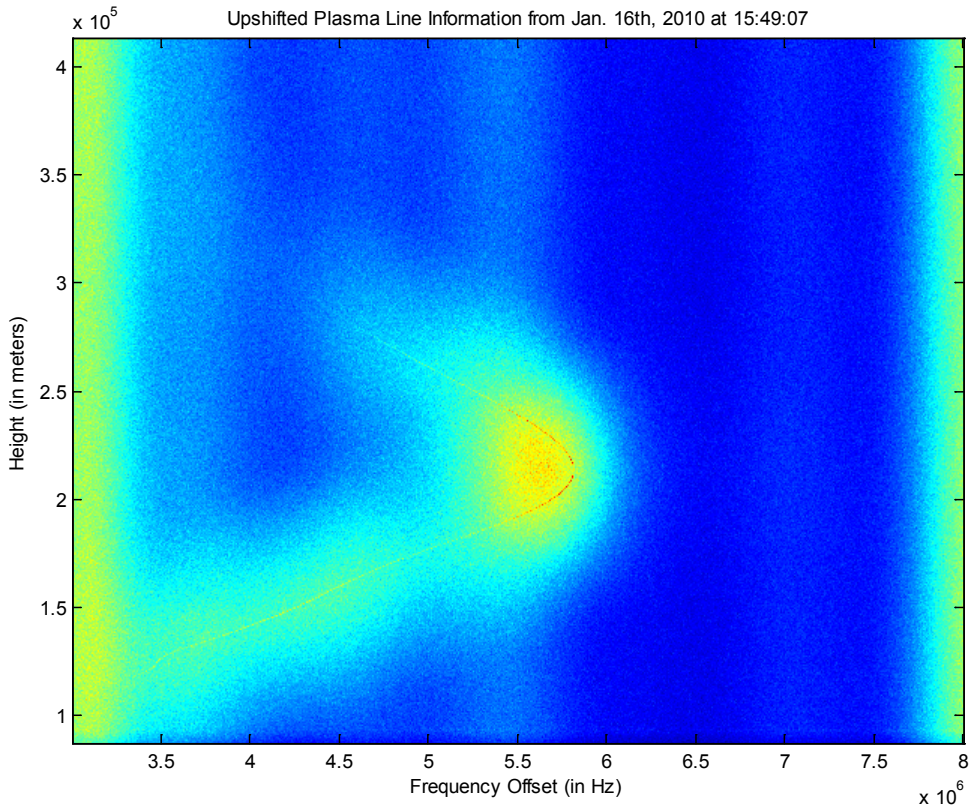

Figure 24: Unfiltered, Raw Plasma Line Time Integration (All Heights).

Figure 24 shows data from one channel with range, frequency, and amplitude all displayed in the image. This image was extracted from the data recovered at 15:49:07 on January 16th. The baseline noise level is common to the entire image. To extract and detrend the baseline noise, the uppermost heights observed in the experiment should be used, as negligible radar information is matriculated back to the receiver from that coded pulse at the uppermost heights for a given time when meaningful signal return is captured at lower heights in the E and F regions.

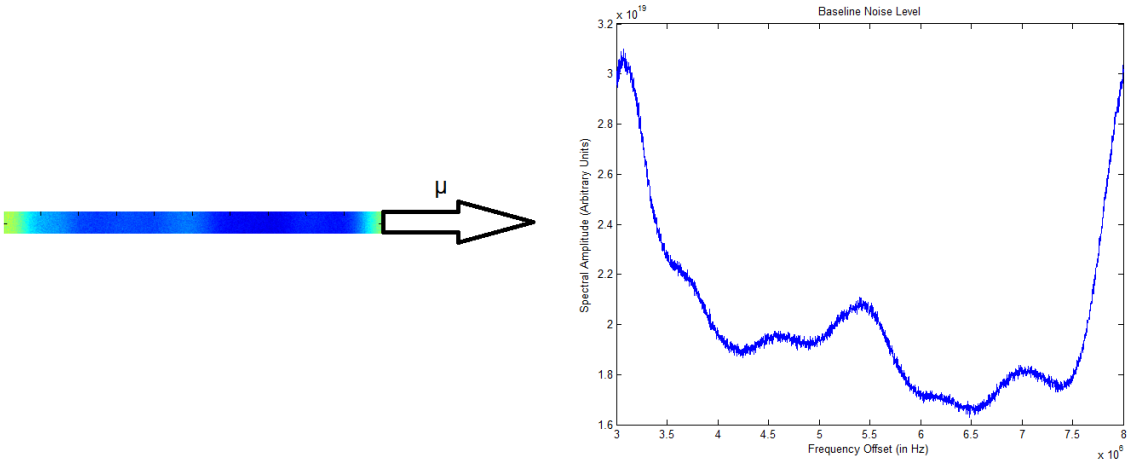

Figure 25: Baseline Noise Level for the Data in Figure 24.

The baseline noise from the uppermost 50 heights is averaged across all frequency bins into a row vector containing an estimate of the baseline noise for each frequency bin in the receiver bandwidth as shown in Figure 25. Each element of the noise vector is then subtracted from the rest of the elements in its column in the image shown in Figure 24, detrending the baseline noise as shown in the comparison of Figures 24 and 26.

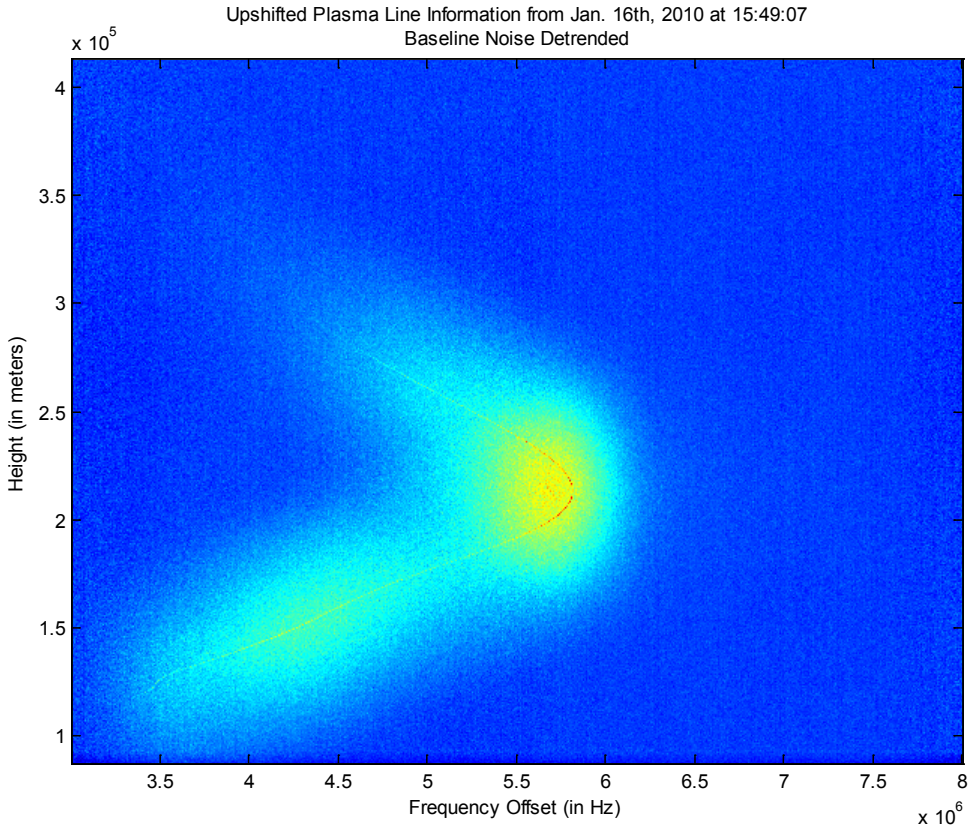

Figure 26: Plasma Line Time Integration with Baseline Noise Removed (All Heights).

While the variance in baseline noise remains, the mean has been effectively removed as shown in Figure 26. Detrending the coarse clutter hump from the data is marginally more involved. A high order least-squares polynomial curve fit has been used to approximate this clutter in past literature (Djuth, et. al, 2010), and since the computational expense of a high order polynomial fit is marginal when compared with the file reading involved in processing many hours of data, a least squares polynomial of order 30 was used to approximate the clutter as shown in Figure 27. The order of the polynomial is high enough to capture the features of the broad hump without compromising the sharp, narrow plasma line.

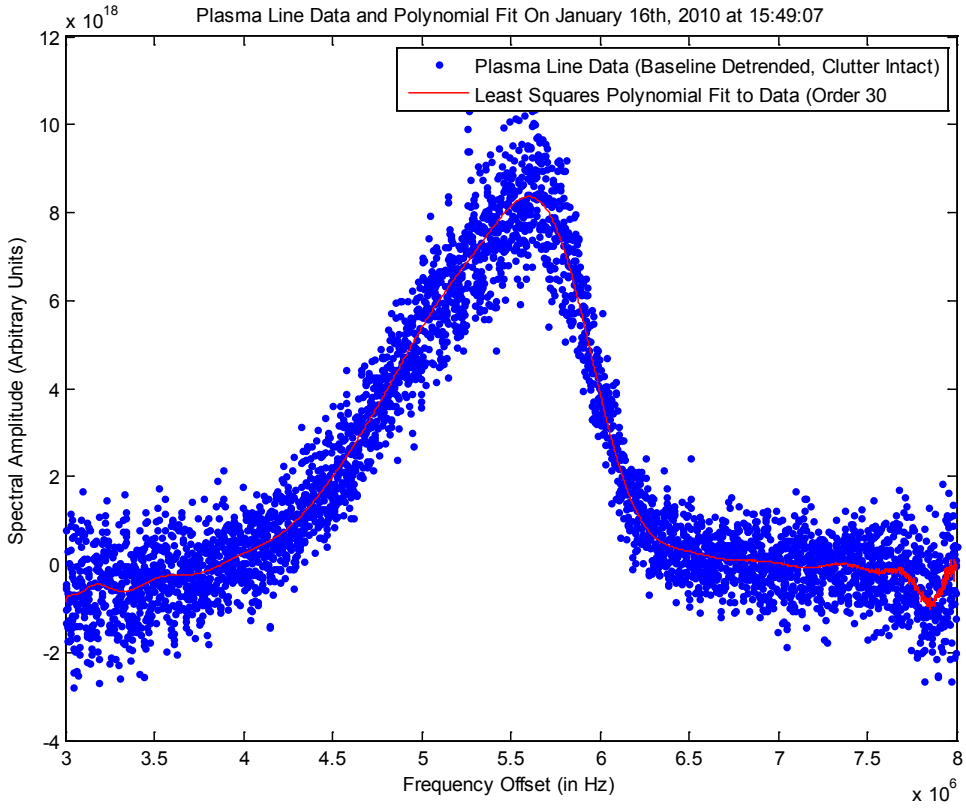

Figure 27: Polynomial Curve Fit to Data to Approximate Clutter.

Figure 28 shows the results of this processing using the same temporal slice from Figures 24 and 26 as an example. Plasma line intensity is retrieved as the residual signal to noise level; plasma line resonant frequency is defined as the frequency location of this maximum, and plasma line spectral width is defined as the full width at full maximum. With most of the noise removed from the data, the plasma line parameters endemic to the data can be better extracted as shown by comparing the 3 images.

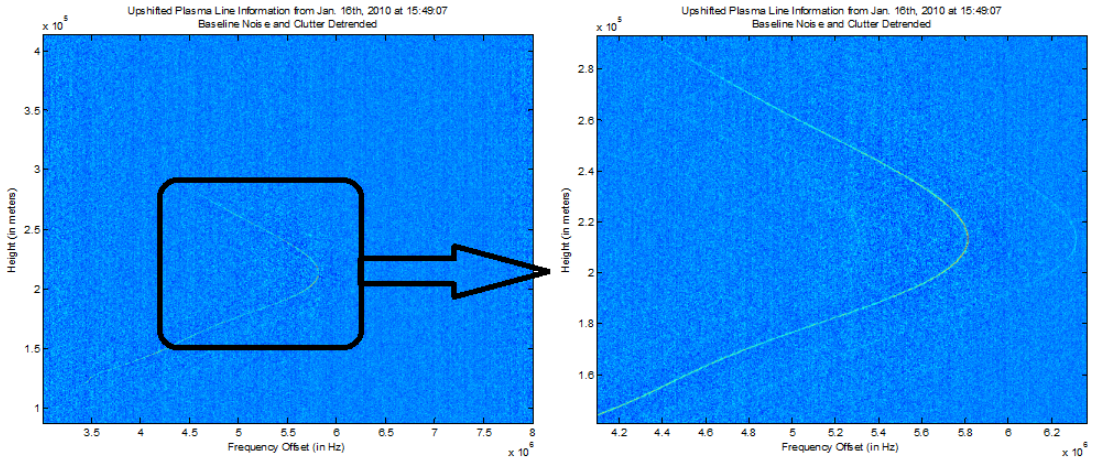

Figure 28: Plasma Line Temporal Integration With Baseline Noise and Clutter Removed (All Heights).

The received plasma line information is uncalibrated, so to study a more meaningful measure of plasma intensity, the plasma line intensities as presented in this thesis are normalized by the baseline noise described earlier. Thusly, signal to noise ratio (SNR) is the metric evaluated for plasma line intensity.

Djuth et. al (2010) states that the spectral shape of the Arecibo plasma line is best approximated by a Lorentzian probability density function with a full width at half maximum of γ/π, though he uses a triangle-squared function in this publication instead. Using the Lorentzian distribution function shown in Equation 41:

$$f(x) = \frac{\propto}{1+\left(\frac{x-x_0}{\omega}\right)^2} \qquad \text{Eq. 41}$$

a two parameter estimation fit was applied to the data as a function of the plasma line frequency, where α and ω are the parameters of interest, and x0 is the location parameter. This method allows for estimation of peak plasma line intensity autonomous of the resolution limits of the frequency cell. Because the data is limited to one sample per frequency bin, the true peak intensity may be clipped as shown in Figure 29.

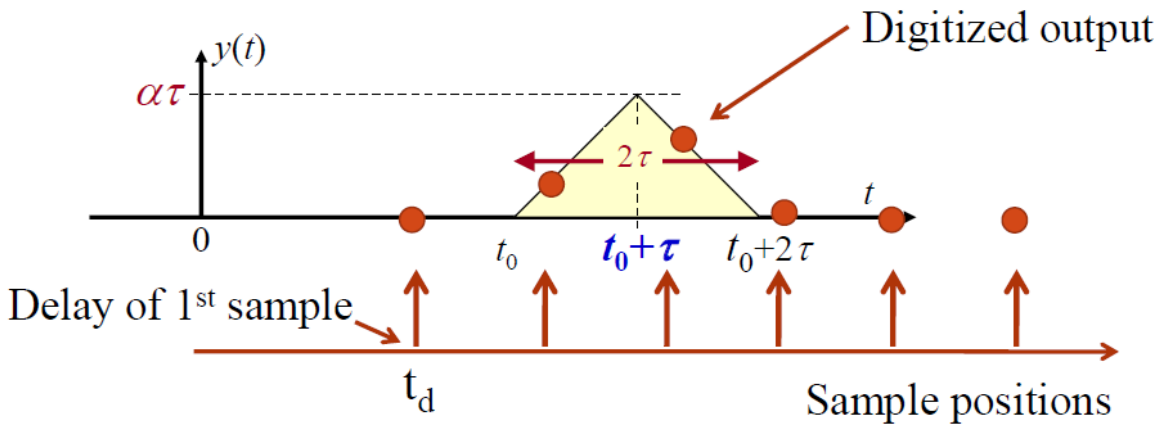

Figure 29: Digital Signal Resolution (CITE DR. ZHOU)

Figure 29 shows the limits of a signal that is digitally sampled in time. However, the same concept is applied to frequency binning as in the plasma line data from Arecibo. The error introduced by frequency binning is half of the frequency bin width, but the nonlinear spectral shape can greatly distort the purported intensity displayed in the processed data when compared with the actual plasma line peak intensity. A demonstration of this concept applied to a vector of plasma line information across the bandwidth of a single channel is available in Figure 30.

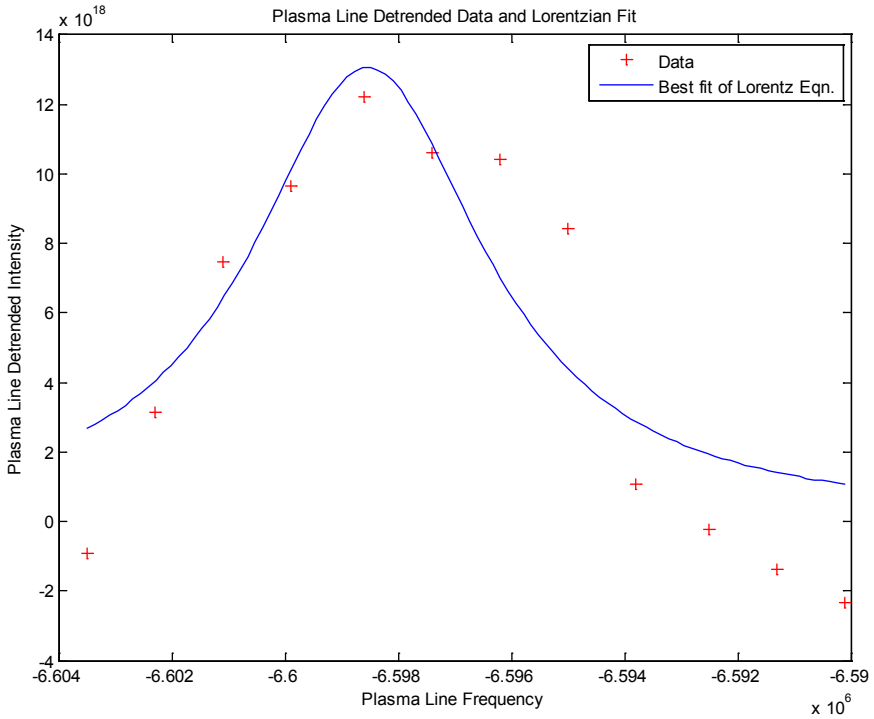

Figure 30: Lorentzian Curve Fitting Example.

This method does not require least squares estimation of the clutter to detrend extemporaneous points from the plasma line information, since the Lorentzian distribution seeks the best curve for the given family of functions given a distribution parameter. The obtained plasma line intensities gathered from the Lorentzian curve fitting over January 22nd, 2010 is shown in Figure 32, and can be compared with the same information collected from the simpler, least squares detrending as shown in Figure 31. The computational speed is greatly increased from Figure 31 to 32, but the perceived benefit is nebulous and unclear.

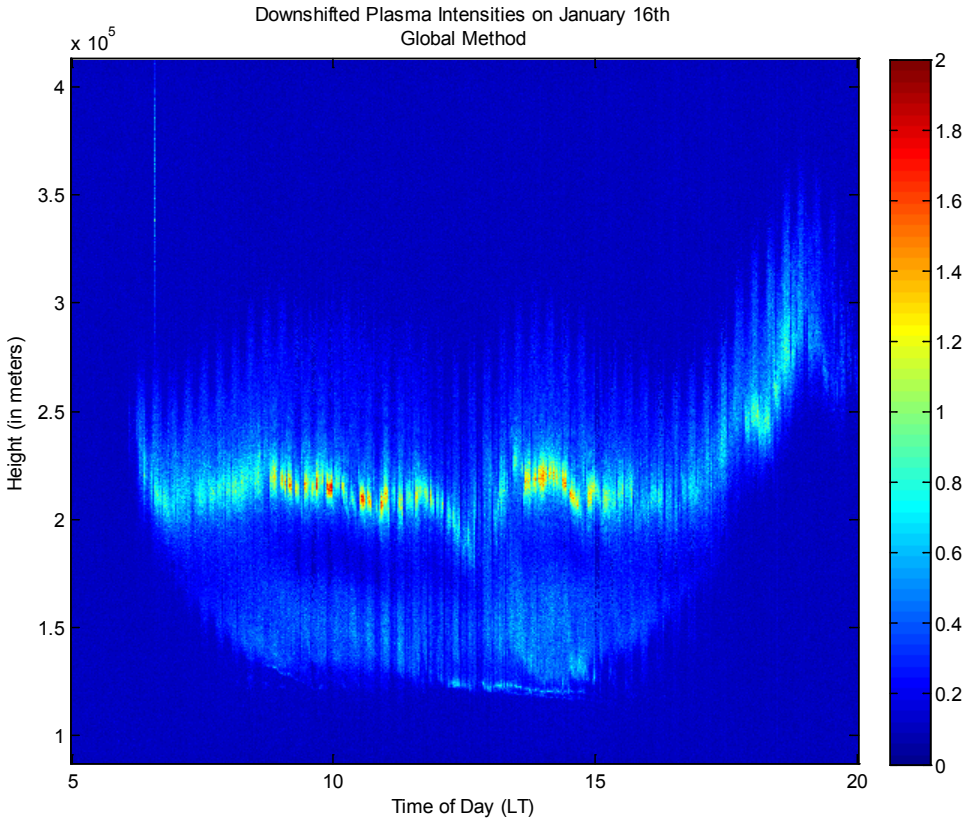

Figure 31: Global Intensities.

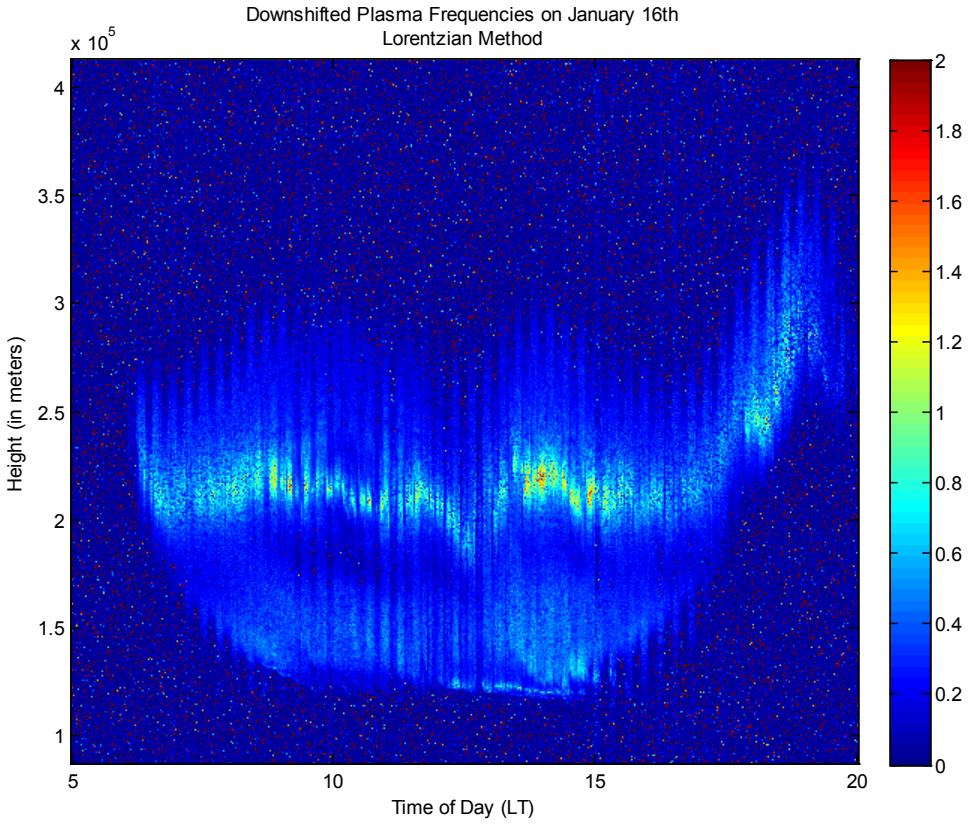

Figure 32: Lorentzian Intensities.

Figures 33 and 34 were procured to visually inspect similarities between these two methods:

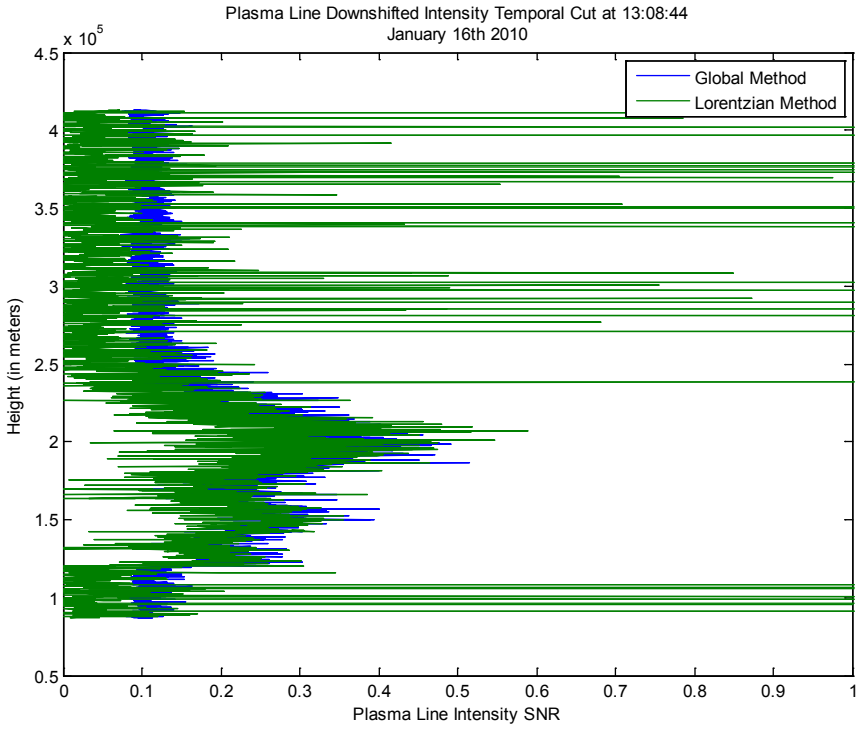

Figure 33: Plasma Line Intensity Temporal Cut.

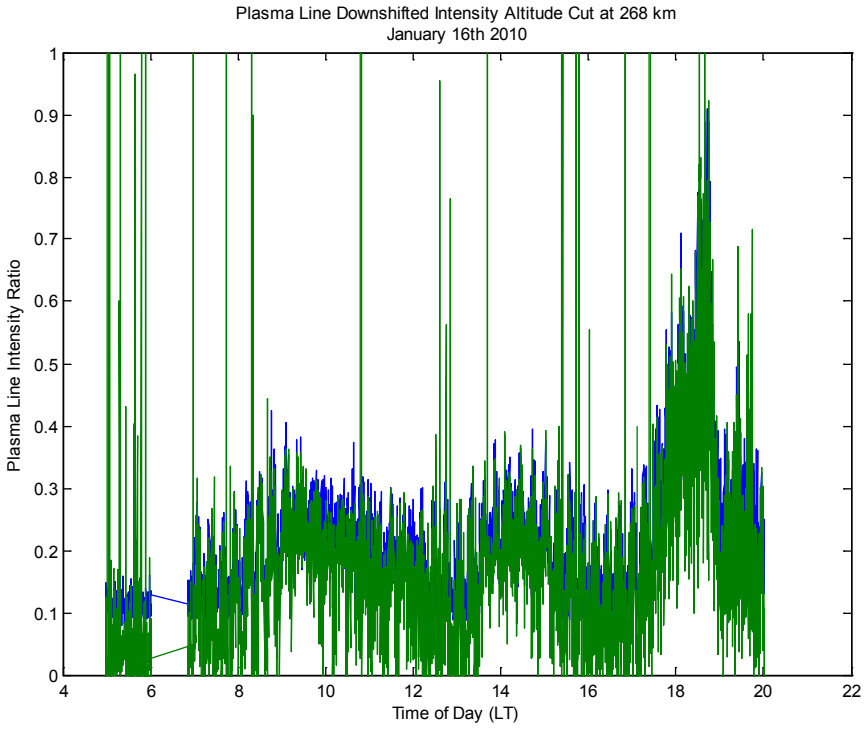

Figure 34: Plasma Line Intensity Altitude Cut.

In an effort to reduce computational expense without sacrificing the improved estimation, moments of the discrete data were taken. Using Equations 42 and 43, the frequency location of the plasma line maximum intensity and an estimator for the plasma line spectral width can be identified, respectively. In these equations, x is the vector of plasma line frequencies at a given height, and y is the vector of plasma line intensities at that height. Equation 42 represents the first raw moment of the data at a particular height, and Equation 43 represents the second central moment. Following from Equation 42, the two nearest plasma line intensities can be weighted and averaged in proportion with the spectral distance from the first moment as estimated.

$$x_0 = \frac{\sum_{i=1}^{x_{max}}(x(i)*y(i))}{\sum_{i=1}^{x_{max}} x(i)} \qquad \text{Eq. 42}$$

$$\sigma = \sqrt{\frac{\sum_{i=1}^{x_{max}}((x(i)-x_0)^2*y(i))}{\sum_{i=1}^{x_{max}} y(i)}} \qquad \text{Eq. 43}$$

As shown in Figures 32 and 35, the results from the Lorentzian curve fitting and the generated moments are similar, yet the computational expense of the latter method is significantly reduced (by a factor of 4).

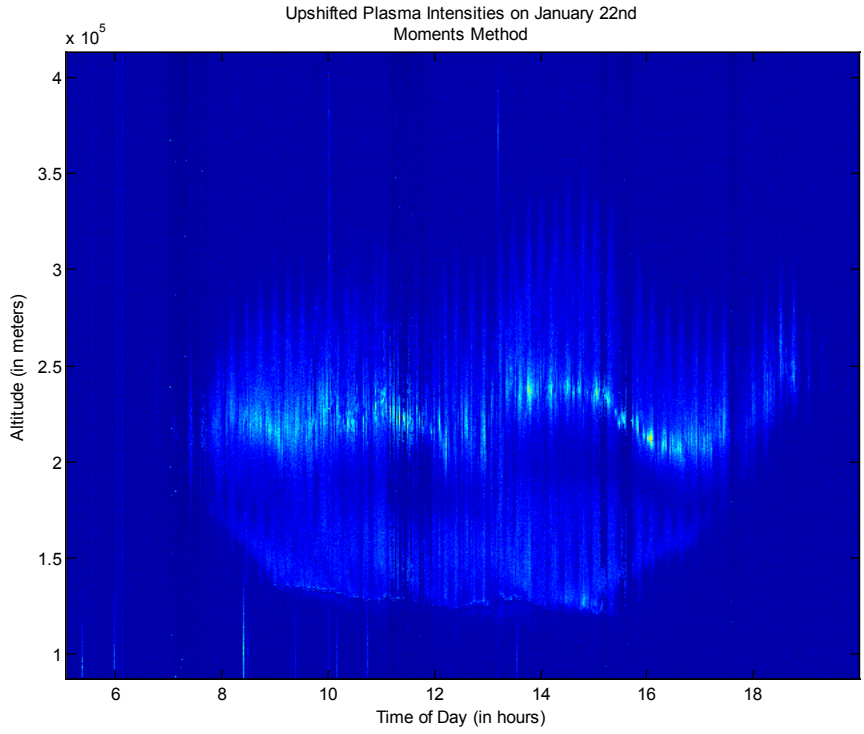

Figure 35: Moment Intensities.

Figures 36 and 37 provide visual inspection of the same cuts displayed in Figures 34 and 35, but by comparing the Global and Moments methods:

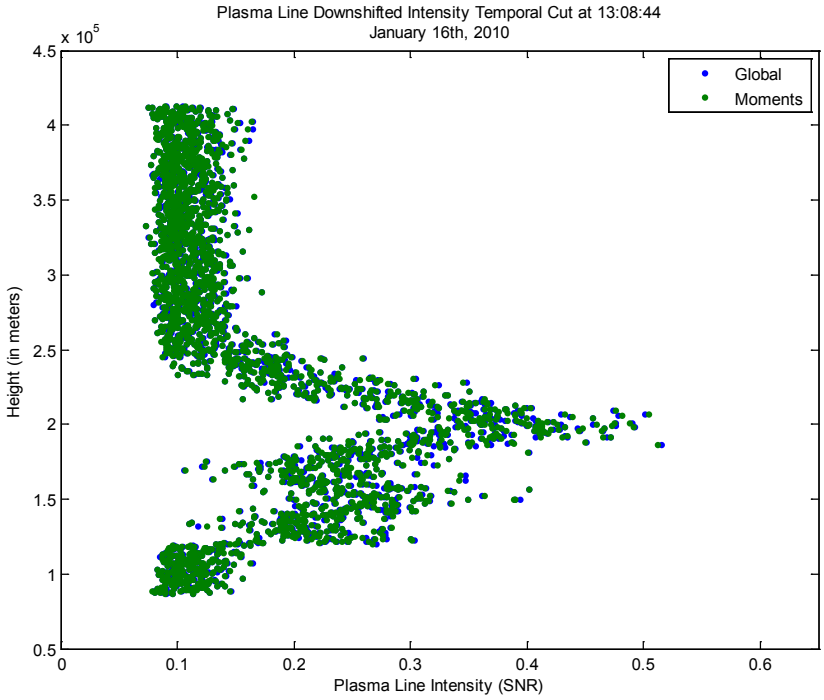

Figure 36: Plasma Line Intensity Temporal Cut.

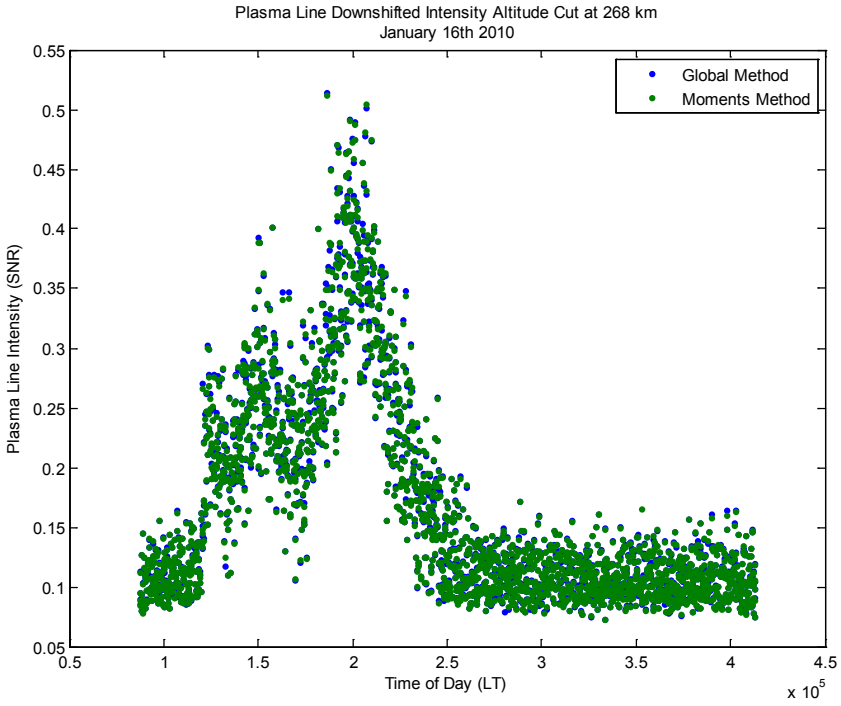

Figure 37: Plasma Line Intensity Altitude Cut.

By visual inspection, it appears that the Moments method more closely approximates the Lorentzian method, but a more robust, quantitative comparison is required to draw this conclusion.

6.2 Method Evaluation

In post-processing, these methods should be evaluated to assess their performance. Evaluation methods used considered computational time, relative bias, and statistical accuracy. Computational bias was assessed using the data on January 16th as a typical day. Relative bias was assessed using January 16th for both the Moments method and the Lorentzian method, each with respect to the frequency and intensity deviances to the global method, since the global method uses the data most directly with minimal curve fitting. Statistical accuracy was studied by observing the differences in plasma frequency and SNR as altitude and time changed. This study, too, uses data from January 16th.

Because the processing code was parallelized, computational time is assess via the performance of a single processor. 129 Processors were used to compute results from 4257

plasma line profiles, so 33 profiles were processed by a single processor. The time for a processor to extract the plasma line using each method is presented in the following table:

Table 3: Computational Time Comparison.

Method	Global	Moments	Lorentzian
Average Compute Time (1 proc.)	28m.33s.	1h.14m.47s.	7h.03m.51s.

Unsurprisingly, both methods that manipulate the data beyond simply extracting plasma line maxima demonstrate longer computational times. However, the method of Moments only increases the computational time by 250% while the Lorentzian method increases the computational time by over 1400%. Should the Lorentzian method prove to be significantly better than the Moments method in terms of statistical accuracy and relative bias from the globally extracted maxima, then this extra time would be warranted. However, the figures and tables below only reinforce the Moments method as preferable to Lorentzian curve fitting.

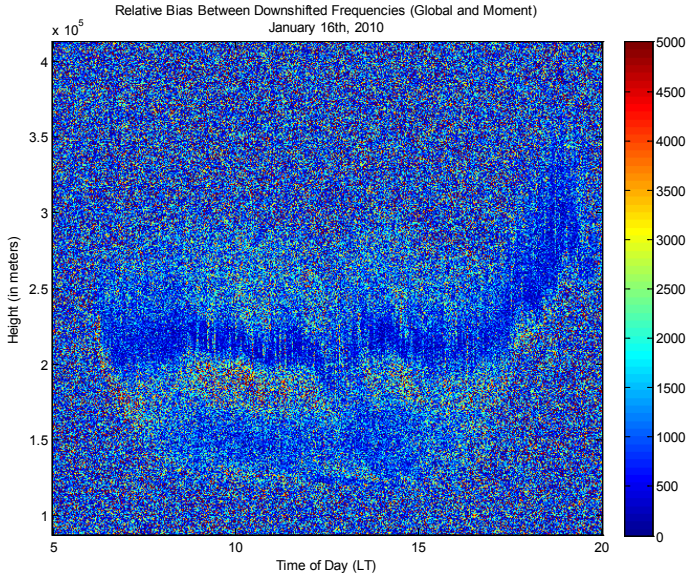

Figure 38: Relative Bias (Frequency) - Global and Moment Methods (in Hz).

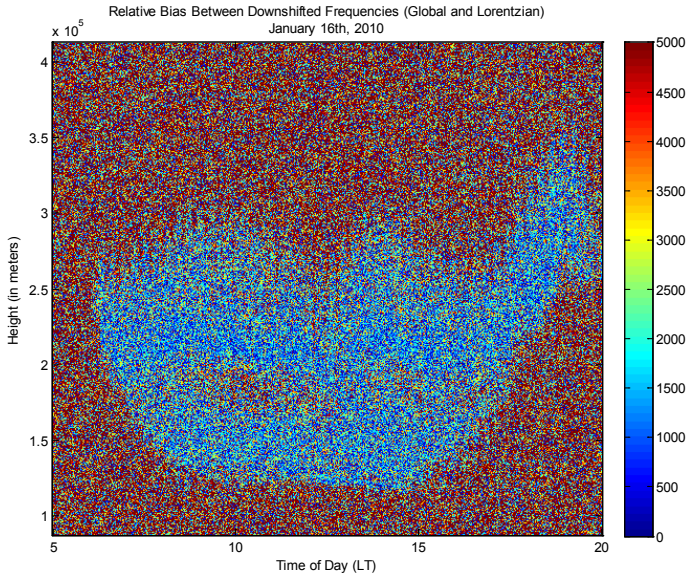

Figure 39: Relative Bias (Frequency) - Global and Lorentzian Methods (in Hz).

Figures 38 and 39 show the relative bias of the Moment and Lorentzian methods compared with the Global method in plasma line frequency. Because the Global method is most closely tied to the data, this is used as the benchmark for comparing relative bias of other methods. Therefore, the larger discrepancy the between the experimentally extracted global plasma line frequency and one of the other methods, the less confidence is expressed in that particular method. By visual inspection, the observed gap from plasma line frequency is significantly larger for the Lorentzian method comparison than for the Moments method comparison for areas where the SNR is highest. Figures 40 and 41, on the other hand, demonstrate a preference for the Lorentzian method, as the gap between Lorentzian and global plasma line intensities is less than for Moments and global plasma line intensities.

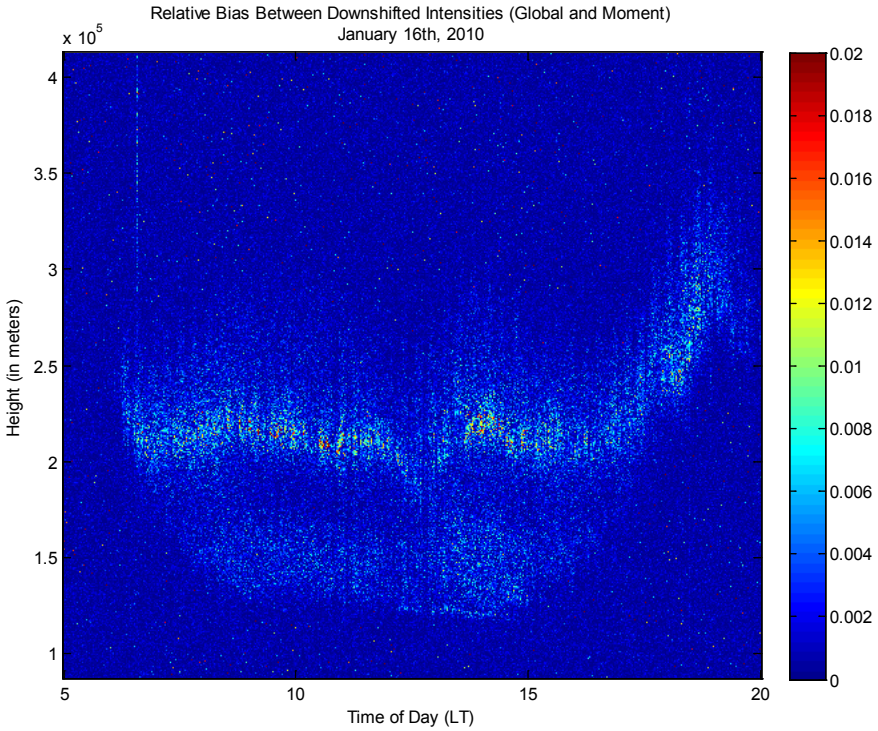

Figure 40: Relative Bias (Intensity) - Global and Moment Methods (in SNR).

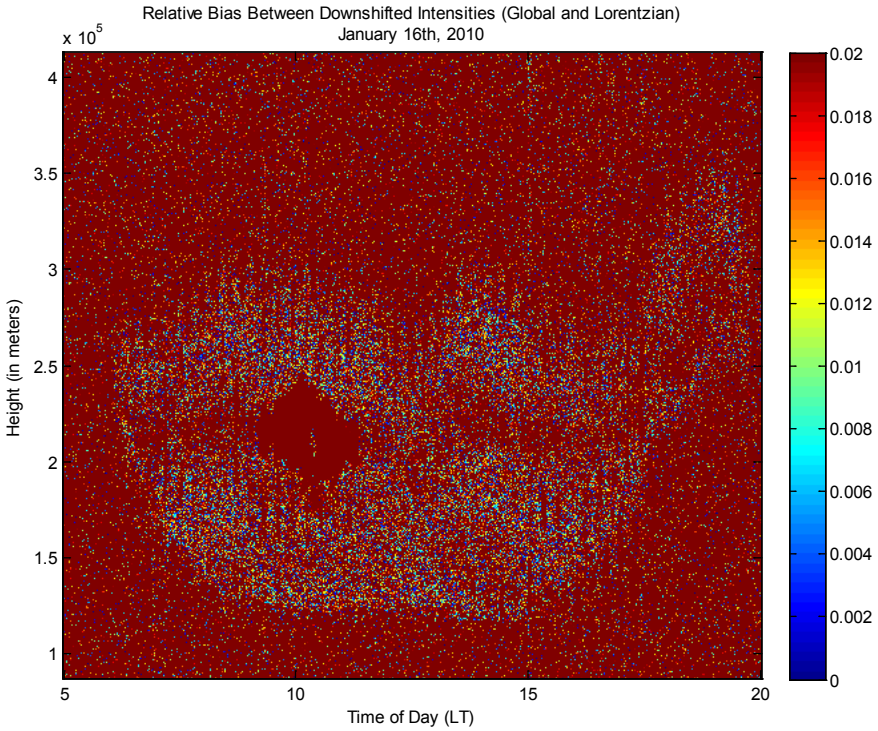

Figure 41: Relative Bias (Intensity) - Global and Lorentzian Methods (in SNR).

A statistical observation of the data elucidates more helpful information. In theory, the plasma line should change minimally and consistently from one altitude bin to the next (300 meters) and from one time integration to the next (10-40 seconds). So computing the temporal and altitude differences in a region where the signal to noise ratio is good allows for a measurement of discrete changes that should be relatively small. The average of these differences was taken for plasma line frequency and intensity using all 3 methods as shown in Table 4:

Table 4: Mean Difference in Plasma Line Frequency and Intensity between Time and Height Bins.

	Global		Moments		Lorentzian	
	Frequency	Intensity SNR	Frequency	Intensity SNR	Frequency	Intensity SNR
Temporal	144190	0.0637	144640	0.0636	147350	0.2522
Altitude	269290	0.1079	269740	0.1077	275500	0.4778

As evidenced by the mean differences shown, the Lorentzian curve fitting method appears to have significantly larger variance from time gate to time gate or from height bin to height bin. This would suggest a lack of statistical accuracy from the Lorentzian method. In short, because of the long computational time and because of the low statistical accuracy, from the studies conducted here, the Global and Moments methods of processing are preferable to the Lorentzian curve fitting method.

7. Post-Extraction Results and Discussion

Once the plasma line information has been extracted, an overview of several days' worth of results can prove fruitful. Displayed below in Figures 42 through 50 are the results from January 15th through the 17th using the Moments method. The same information can be found in the appendices using all 3 methods and including a 4th day of data (January 22nd).

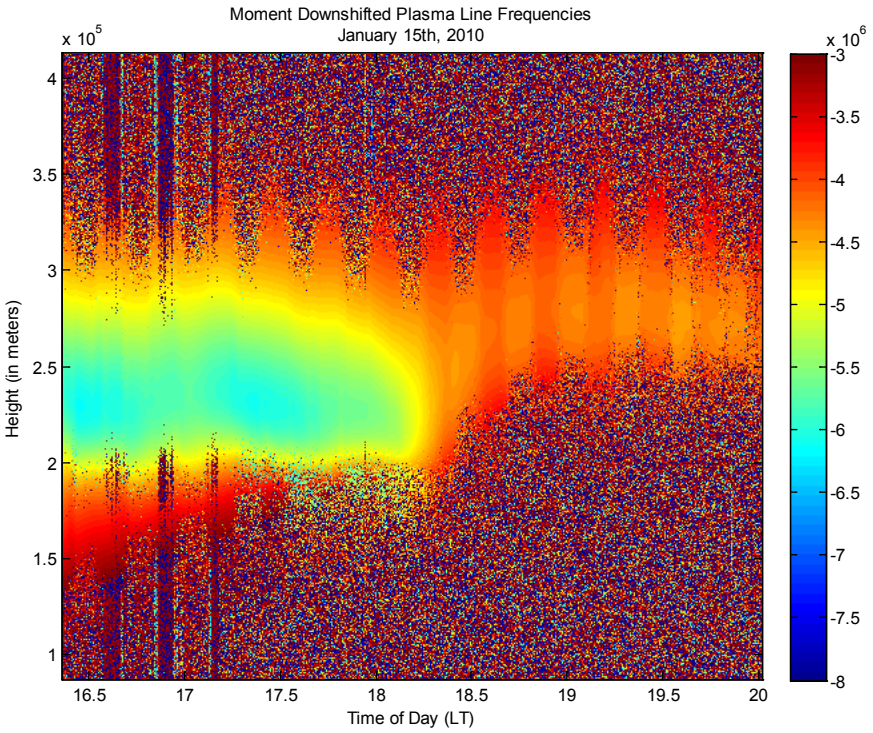

Figure 42: Downshifted Plasma Line Frequencies, January 15th 2010.

7.1 Conjugate Point Electrons

The downshifted plasma line frequencies provide us with results worth discussing. Notable in Figure 42 is that even though the sun has set in Arecibo towards the end of the run, there is still a plasma resonance feature visible. This is due to photoelectrons above the conjugate point in Argentina propagating along magnetic fields from South to North.

On January 17th, the afternoon plasma activity is elevated, as evidenced by the higher deviation from Arecibo's center frequency in comparison with either January 15th or 16th for

most of the afternoon. The frequency deviation from center is directly proportional to electron density. If the resonant frequency of the wave is considered mechanically, the electron density is part of a term analogous to the stiffness of the wave. Conceptually, considering how energy will exchange between electrons packed closely together or far apart as they oscillate confirms that a higher plasma resonance frequency will dictate the existence of more electrons in the same volume. Analytically, this can be expressed through Equations 10 and 11. On January 17th, the plasma activity was high enough to saturate the frequency band of the radar slightly below 250km and slightly later than 15:00:00 LT.

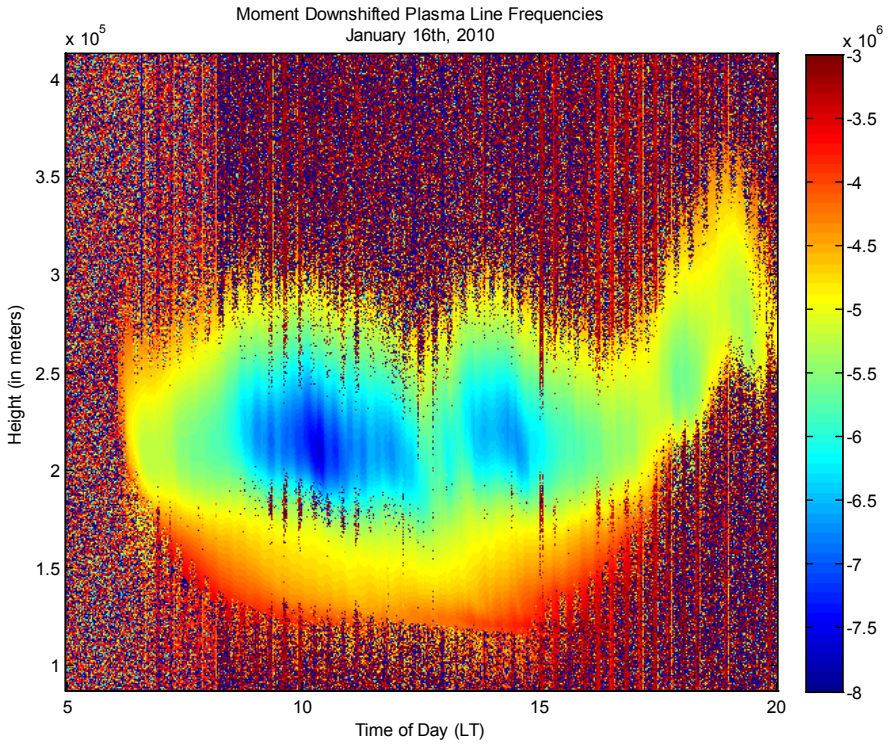

Figure 43: Downshifted Plasma Line Frequencies, January 16th, 2010.

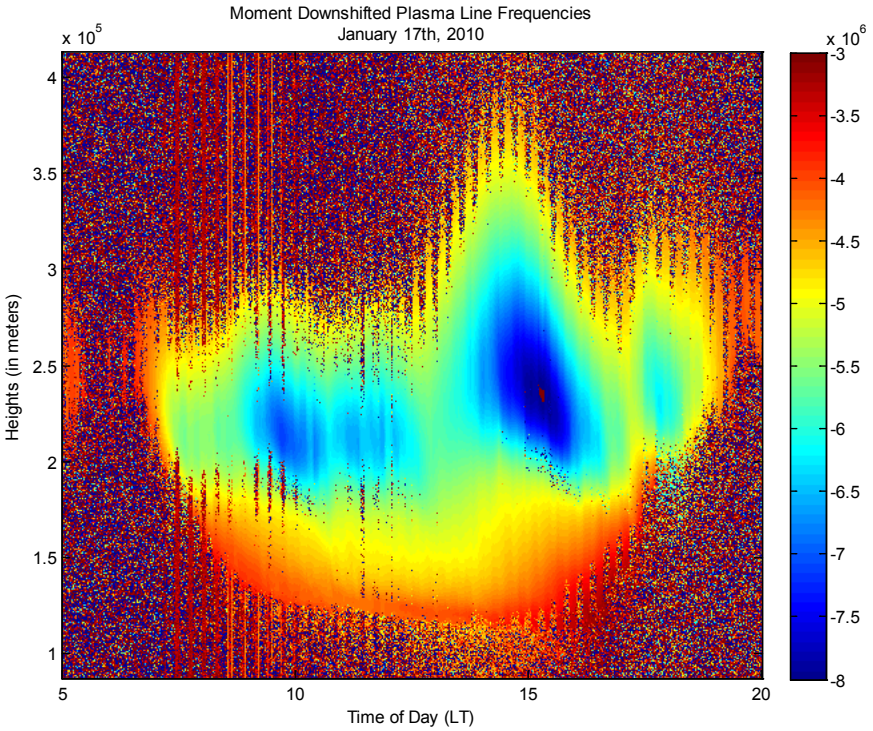

Figure 44: Downshifted Plasma Line Frequencies, January 17th, 2010.

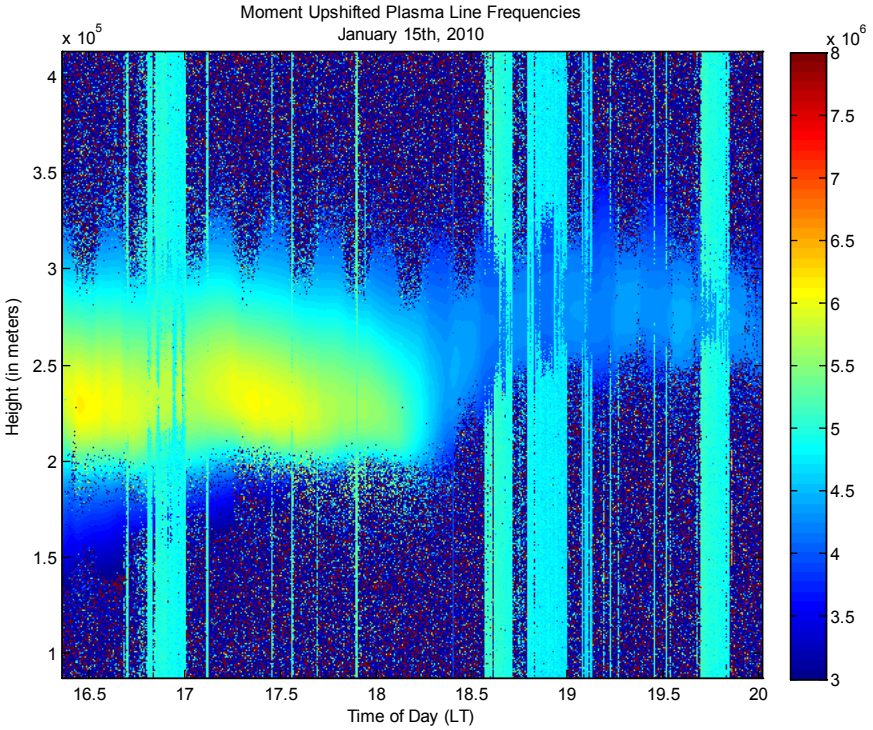

Figure 45: Upshifted Plasma Line Frequencies, January 15th, 2010.

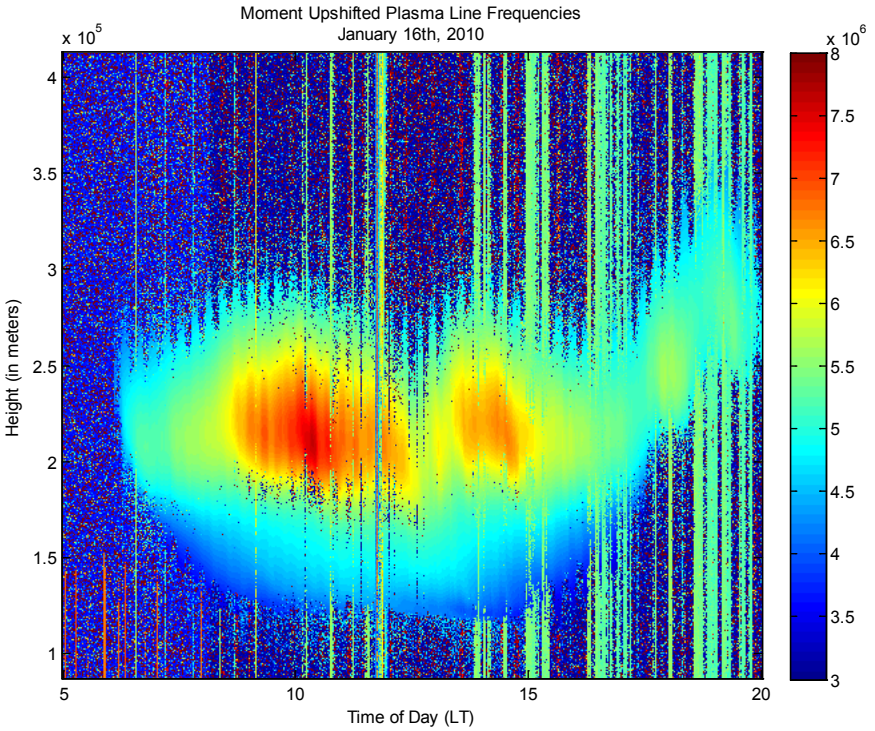

Figure 46: Upshifted Plasma Line Frequencies, January 16th, 2010.

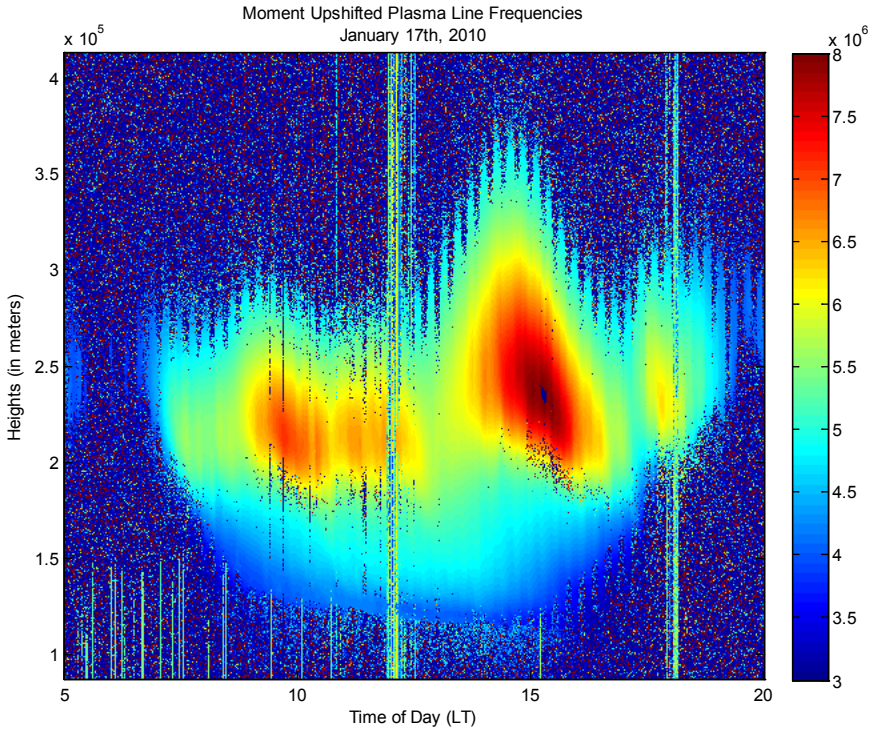

Figure 47: Upshifted Plasma Line Frequencies, January 17th, 2010.

7.2 Upshifted vs. Downshifted Frequencies

The upshifted plasma line frequencies demonstrate nearly identical information. One different observation is that more noise seems to be evident in the upshifted plasma lines as opposed to the downshifted ones. This is discussed in more detail later in the chapter. The plasma line resonant frequency is nearly identical for both lines, but the downshifted and upshifted plasma lines correspond to upward traveling and downward traveling Langmuir waves, so the plasma lines will correspond to different wave vectors. The different wave number is expressed in the thermal term of the plasma wave dispersion relation (Equation 10), and is primarily a function of electron temperature. In this way, electron temperature can be computed using the asymmetry between plasma line resonant frequencies (Nicholls, 2006).

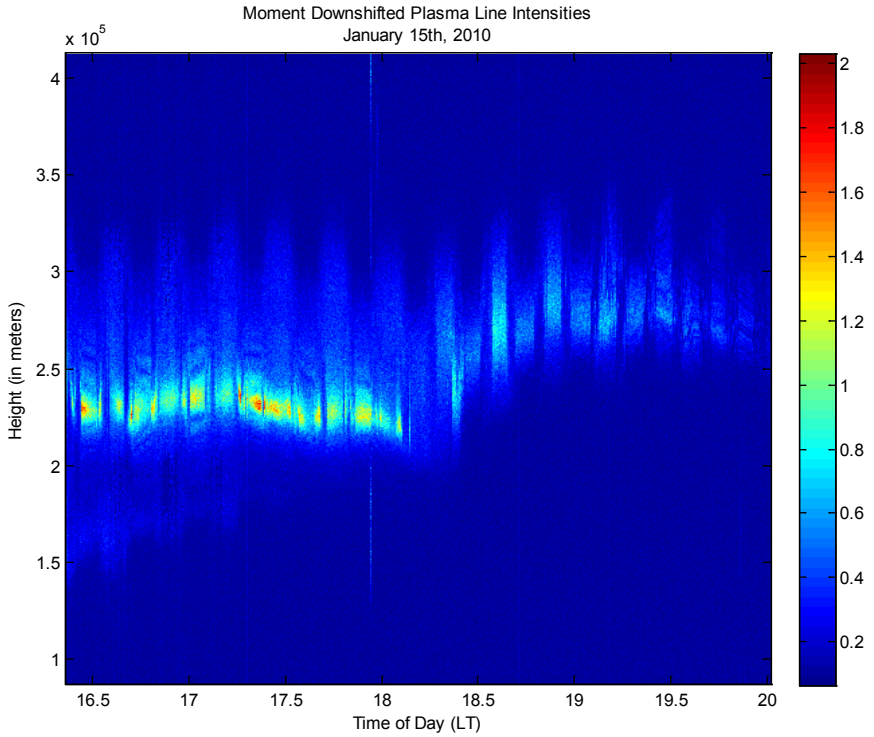

Figure 48: Downshifted Plasma Line Intensities, January 15th, 2010.

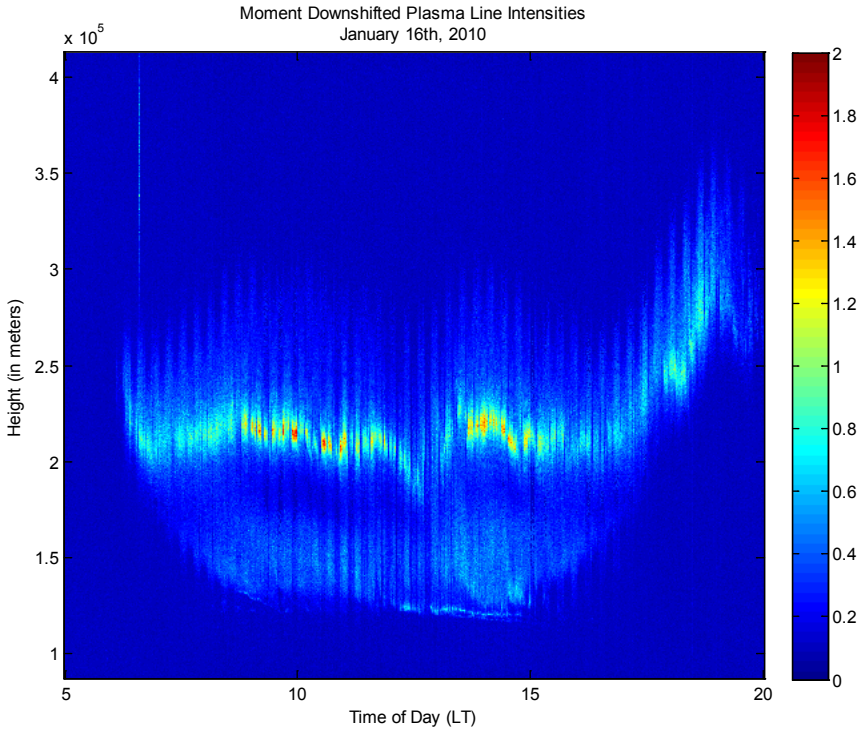

Figure 49: Downshifted Plasma Line Intensities, January 16th, 2010.

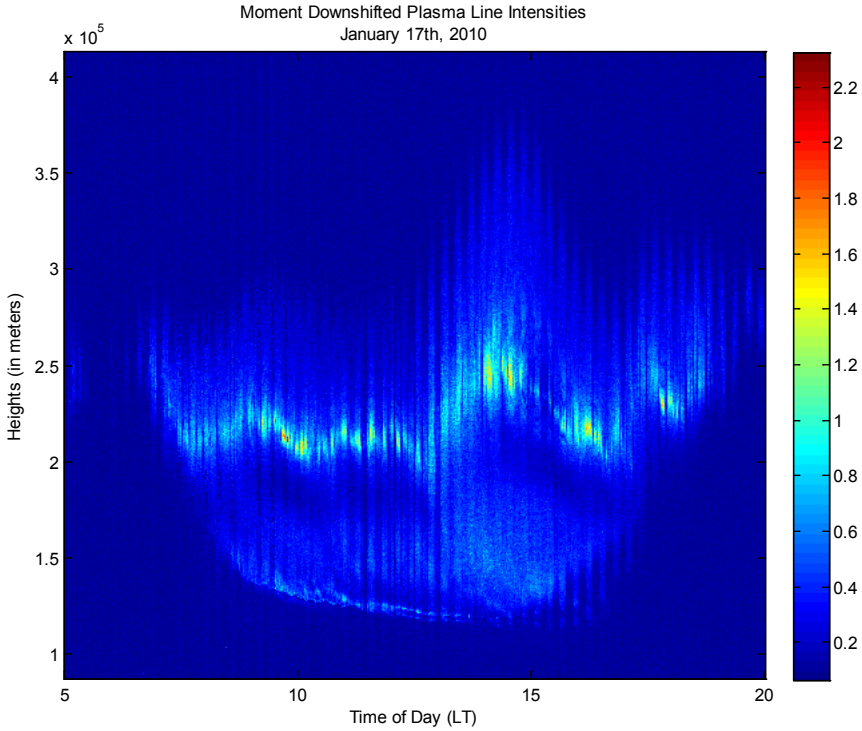

Figure 50: Downshifted Plasma Line Intensities, January 17th, 2010.

7.3 Low Plasma Layer

The plasma line intensity SNR is often too poor to measure the feature above the noise level but superthermal electrons present in the high energy tail will enhance the Langmuir wave intensity up to 50 times above what is predicted simply by evaluating wave intensity as proportional to the electron temperature as discussed in Chapter 3. This is especially evident in the region corresponding to the F layer peak (near 225 km), where a higher electron density (Figure 1) begets more superthermal electrons to further exaggerate the Langmuir wave intensity in the region.

The f0F2 peak is clearly visible here, but it is exceeding low compared with what would be expected from past results. The ion line information from this experiment was used to study vertical ion drift, midnight collapse, and ambipolar diffusion. It was discovered that the vertical drift is consistently downward for the days presented here, pushing the plasma to lower altitudes (Gong, 2011).

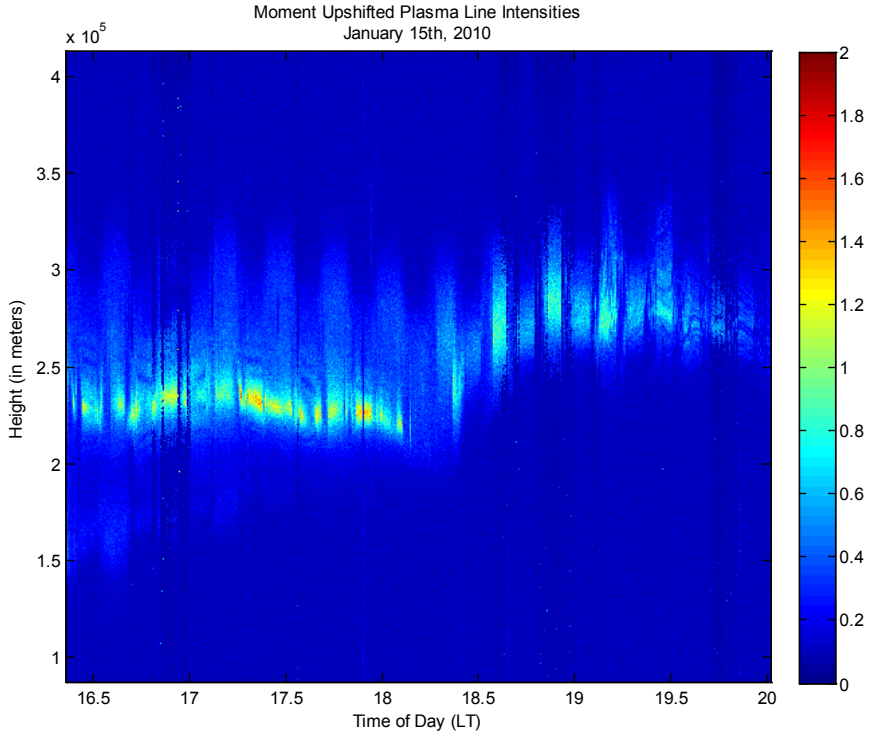

Figure 51: Upshifted Plasma Line Intensities, January 15th, 2010.

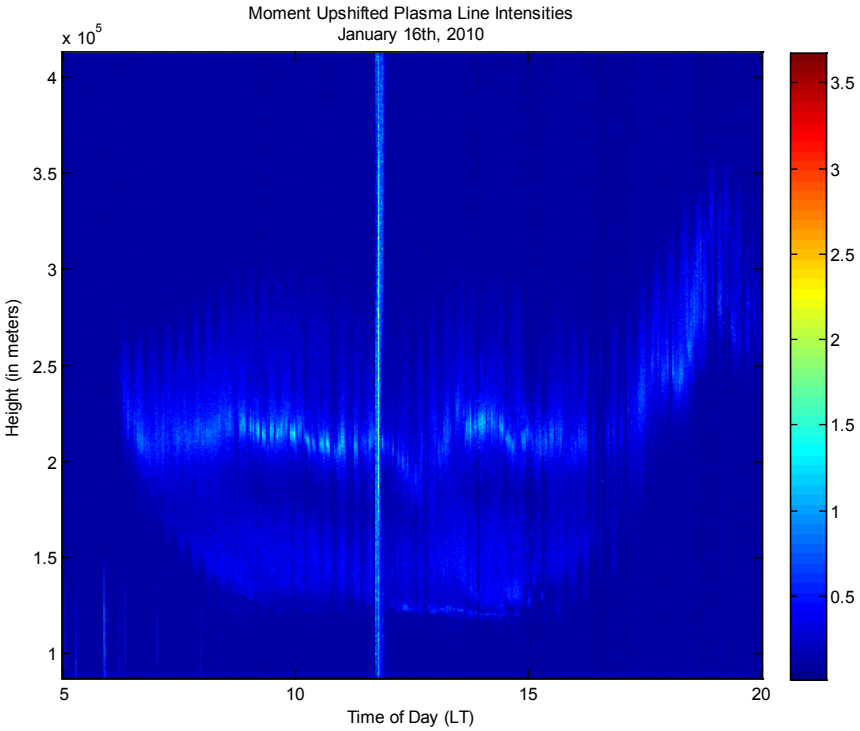

Figure 52: Upshifted Plasma Line Intensities, January 16th, 2010.

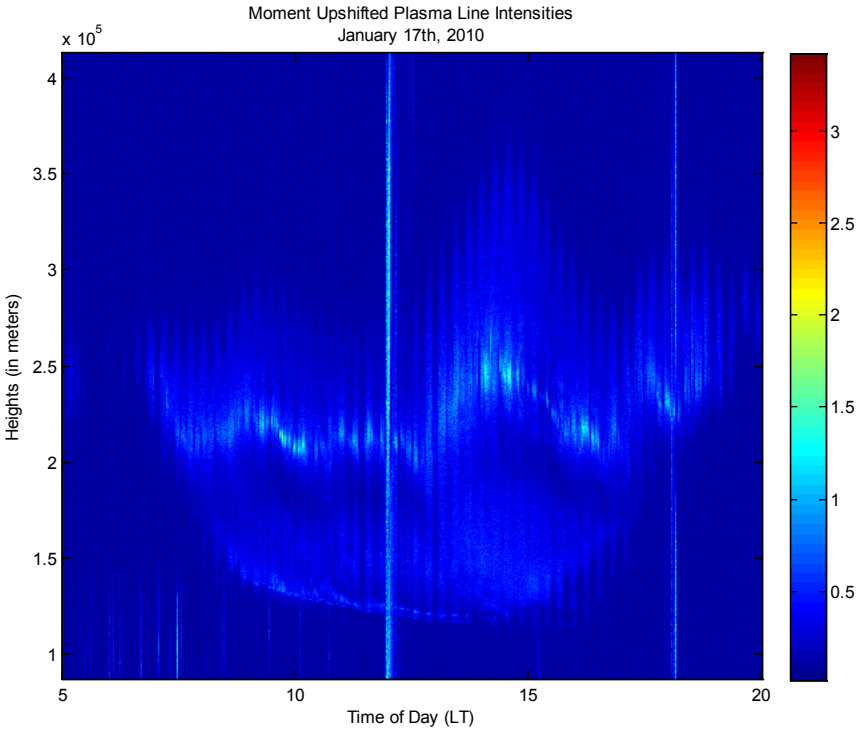

Figure 53: Upshifted Plasma Line Intensities, January 17th, 2010.

7.4 Upshifted vs. Downshifted Intensities

Like the comparison between downshifted and upshifted plasma resonance frequencies, there are copious similarities between downshifted and upshifted plasma line intensities. The primary differentiating aspect is the weaker signal observed at the upshifted plasma frequency. This is best observed in Figure 55, as the ratio of downshifted to upshifted plasma intensities are mostly above 1. Considered from the perspective of Doppler shifts with respect to the center frequency, the downshifted information represents Langmuir waves traveling along a wave vector away from the transmitter, and the upshifted information represents Langmuir waves traveling along a wave vector towards the transmitter. Since the ratio is larger than 1 during the daytime, photoelectron transport is generally propelling away from the radar. Using similar logic, the trend reversal after sunset showing a plasma intensity ratio less than 1 accounts for the conjugate point photoelectrons precipitating into the ionosphere over Arecibo from Argentina.

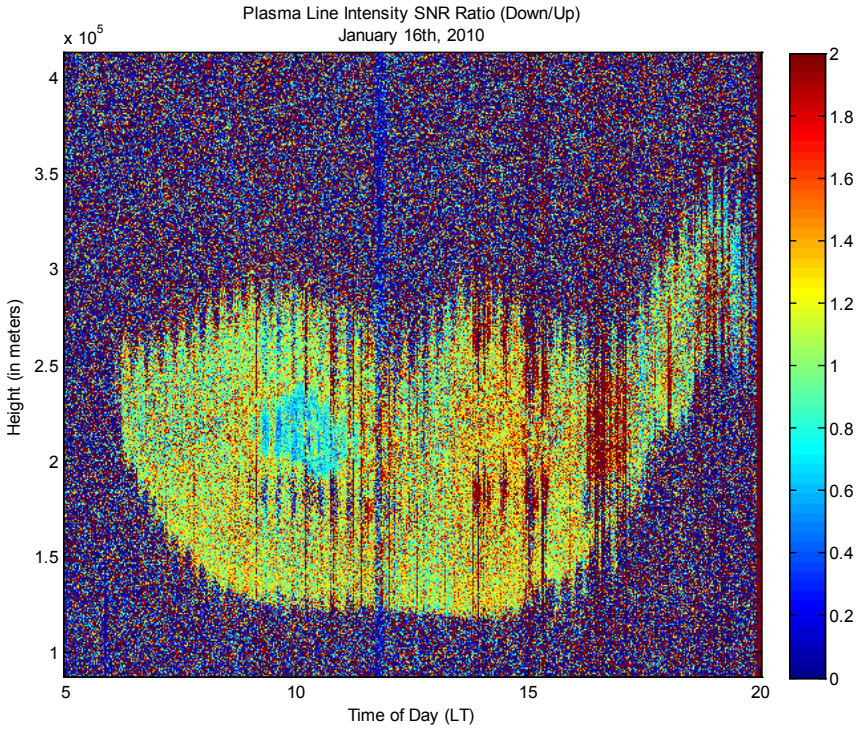

Figure 54: Plasma Line Intensity Ratio, January 16th, 2010.

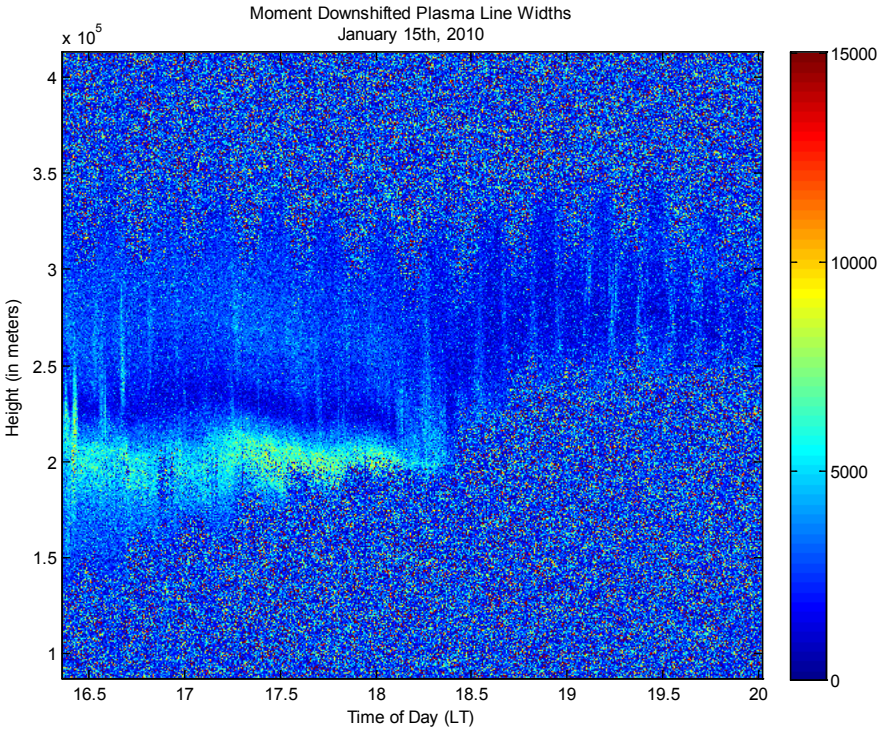

Figure 55: Downshifted Plasma Line Widths, January 15th, 2010.

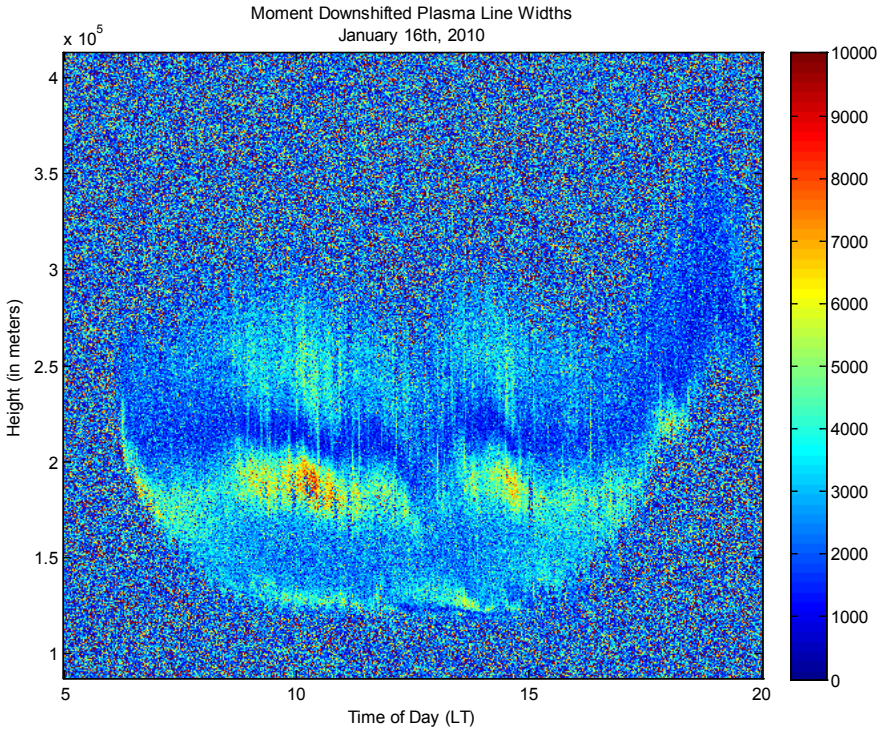

Figure 56: Downshifted Plasma Line Widths, January 16th, 2010.

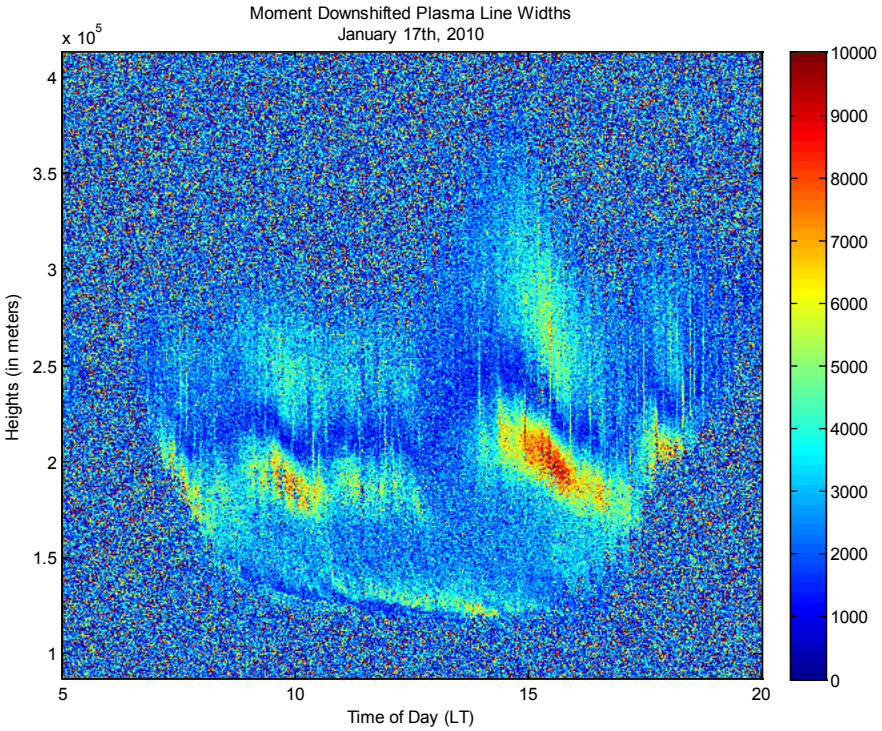

Figure 57: Downshifted Plasma Line Widths, January 17th, 2010.

7.5 Spectral Width Observations

Frank Djuth describes the spectral width of the F-region plasma line as determined by the vertical electron density gradient across the range cell (Djuth, et. al, 1994), and as measured, is proportional to the Langmuir frequency variation across the scattering volume over that time integration. One significant observation is the somewhat inverted relationship between the electron density (proportional to plasma resonance frequency and a high density belies a large plasma line intensity above the noise level) and the spectral width. This is most prominent at the F-region peak, where the plasma line spectral width drops to a single bin.

There is asymmetry above and below the F region peak; the faster the decay of the F region peak over a particular altitude range, the larger the vertical density gradient, and therefore the spectral width is wider. The larger spectral widths below the peak qualitatively match expectations from Figure 1, provided the low peak relative to Figure 1 is accounted for. The upshifted information is similar and is provided below for completeness.

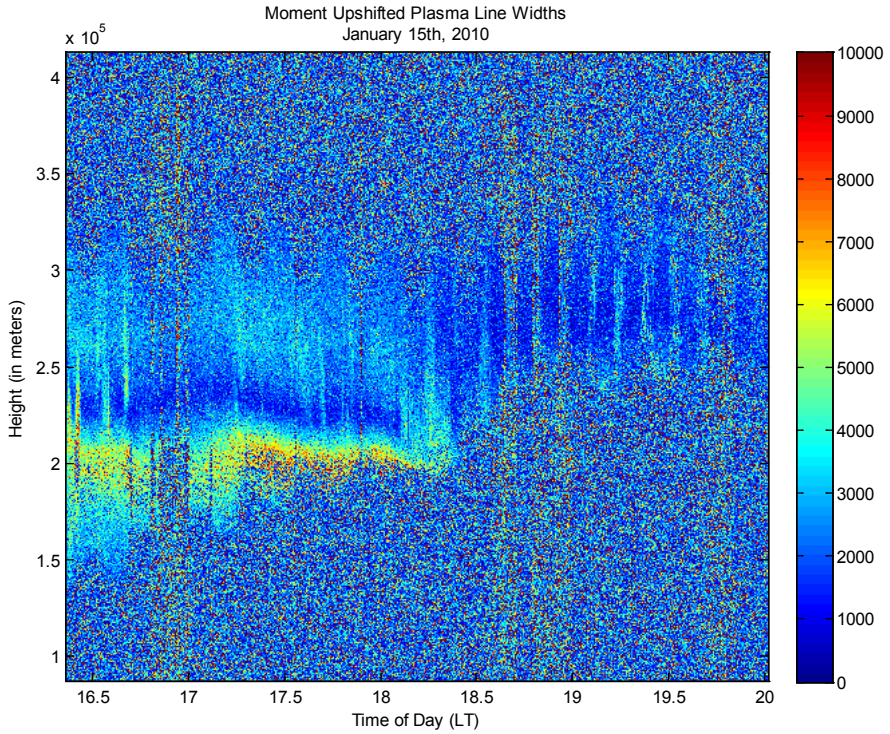

Figure 58: Upshifted Plasma Line Widths, January 15th, 2010.

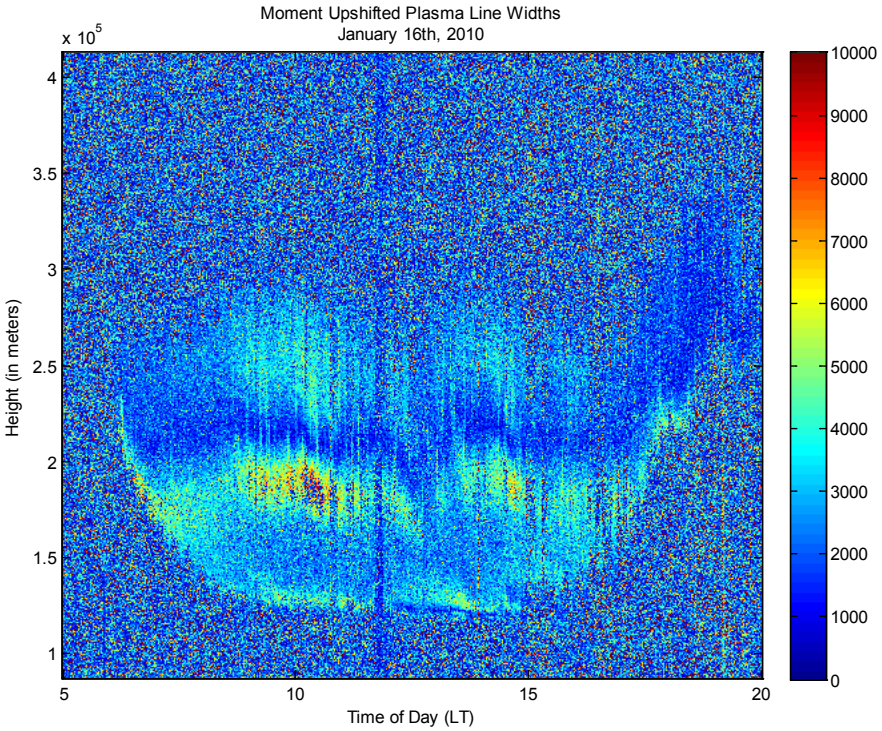

Figure 59: Upshifted Plasma Line Widths, January 16th, 2010.

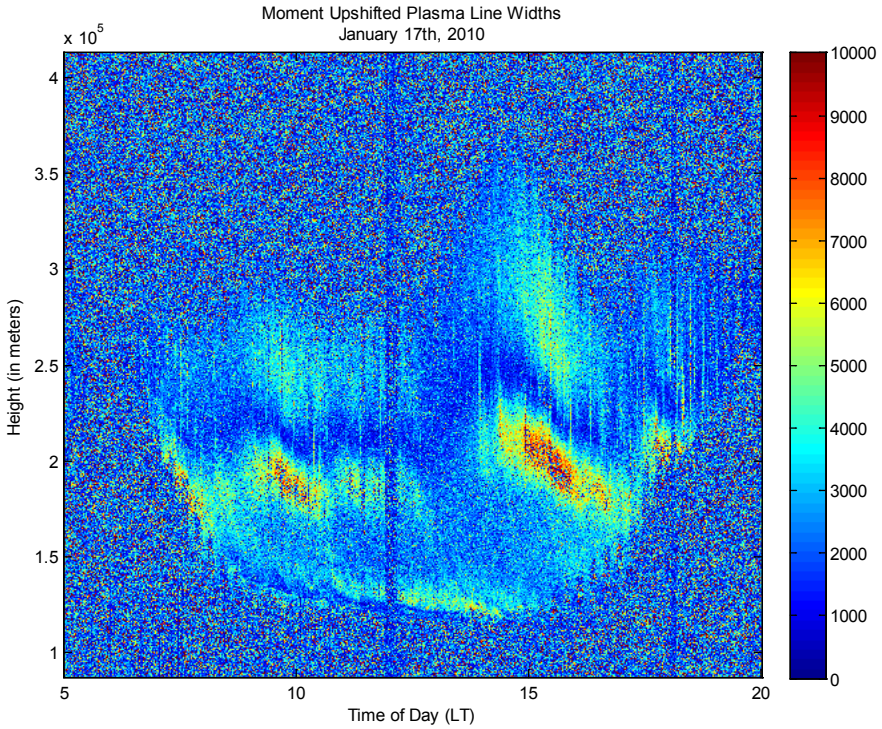

Figure 60: Upshifted Plasma Line Widths, January 17th, 2010.

7.6 *Ionospheric Tilting and Horizontal Inhomogeneity*

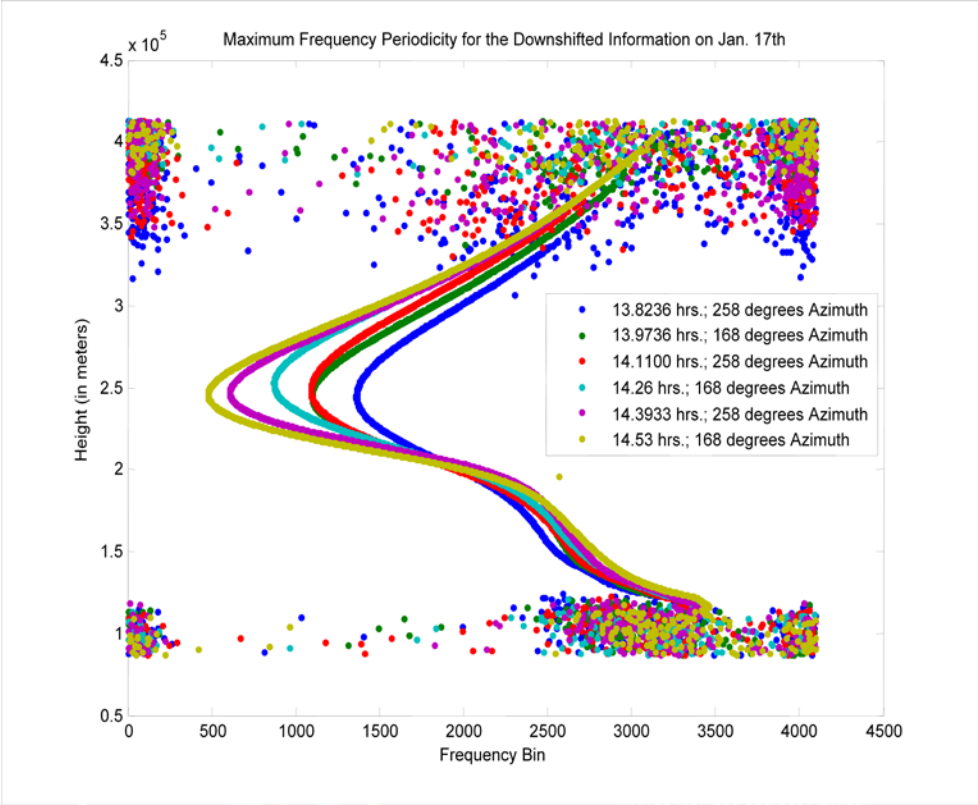

Figure 61: Horizontal Inhomogeneity

In Figure 61, the differently colored lines correspond to plasma line information obtained from the radar at the extreme limits of the rotating beam. Two phenomena are observed that suggest strong transmitting angle dependence for the plasma line information. The stronger deviation from the center frequency at 168 degrees Azimuth as opposed to 258 degrees Azimuth for the same cycle would indicate a significantly higher electron density. Consider the difference between the information posted at 13.8236 hours as opposed to at 13.9736 hours. However, several minutes later, the electron density appears to have regressed in spite of the electron density continuing to grow over the subsequent half hour. This suggests that electron density and azimuth angle are both predictors of plasma line resonant frequency as Eq. 26 delineates. Additionally, at 168 degrees Azimuth, higher signal to noise ratio is evident at extremely high and low altitudes. Decoupling this trend to resolve both plasma line frequency and intensity dependence on radar beam transmission angle requires further study.

8. Conclusions and Future Work

8.1 Conclusions

This thesis focuses on the presentation and discussion of prominent results from one ISR experiment's plasma line data, focusing on the visible data from January 15th-17th and January 22nd of 2010. The primary difference between the data from the first few days (15th-17th) and the last day (22nd) is the ISR beam rotation coverage. From the 15th through the 17th, the beam is only in rotation for 90 degrees. On the 22nd, the beam is rotating through 360 degrees of motion.

Many similar plasma line studies were limited in coverage by computational speed and storage capacities. As a result of current encoding techniques and cheap storage, a large bandwidth can now be observed over the entire altitude range where meaningful Langmuir wave interaction with the radar beam is expected to occur. This elicits a need for improved signal processing techniques.

Two signal processing techniques (a method using Lorentzian curve fitting and one using moments of discrete data) were compared with the results from simply extracting the plasma line via removal of baseline noise level and clutter. These methods were compared by computational time allotted, by relative bias to the global maximum, and by rate of change both temporally and by range gate. The features that were compared, and that are of primary interest in informing the scientific community of the plasma physics endemic to the region, are the plasma line resonant frequency, the plasma line peak intensity, and the plasma line spectral width. These features provide similar information (electron density, electron temperature, etc) as the ion line ISR spectral component, but provide deterministic rather than stochastic parameters, as the plasma line information is independent of noise level, provided the plasma line can be viewed above the noise level at all. The ion line, on the other hand, requires complex curve fitting and integration techniques to deconstruct into physical parameters, deteriorating the accuracy of the measurement with any noise detected at all.

From the comparison techniques used, the simple global appears to be preferable to the Lorentzian method and the Moments method due to minimal improvement in accuracy with much larger computational time. Three days' worth of data were used to explore several salient features of the dataset using the Moments method. Special attention was given to the low plasma

layer, vertical inhomogeneity as expressed by the spectral width, and the presence of conjugate point photoelectrons as predicted by Carlson (1966).

8.2 Future Studies

As the primary driver for this experiment was the ion line data and not the plasma line data, there are several days of experimental data for which adequate plasma line information was not successfully recovered to summarize a day's Langmuir wave behavior. Some saturation of the frequency band was observed when the plasma line enhancement was exceptionally strong, causing some clipping and aliasing of the plasma line. Furthermore, most of the data available has limited quadrant coverage in beam rotation. Seasonal dependence of photoelectron plasma line enhancement would additionally serve as an interesting study. Additionally, some salient features of these data may require further study. In short:

1. Adjust and broaden the frequency band for greater coverage in order to successfully capture all plasma line features across several days for all heights where meaningful signal return is expected.
2. Analyze ionospheric tilting direction to investigate horizontal gradient more thoroughly.
3. Ensure adequate profile capture sufficient to analyze all days for which data is available (on the order of a few thousand plasma line time integrations per day).
4. Study the plasma line in the summer to compare with winter results.
5. Should the La Plata, Argentina AMISR facility be installed, corroborating their measurements with Arecibo's ISR to better analyze conjugate point photoelectrons would be beneficial to facilitate understanding.
6. Further investigation into the possible presence of an ionospheric descending layer ~125km in the current dataset is warranted.

9. BIBLIOGRAPHY

Bernstein, I. B. (1958). An energy principle for hydromagnetic stability problems. *Proc. R. Soc. London*, *A*(244), 17.

Bhatt, A. N., Nicholls, M. J., Sulzer, M. P., Kelley, M. C. (2008). Observations of plasma line splitting in the ionospheric incoherent scatter spectrum. *Physical Review Letters*, *100*(4).

Bowles, K. L. (1958). Observation of vertical-incidence scatter from the ionosphere at 41 mc/sec. *Physical Review Letters*, *1*(12), 454-455.

Brillouin, L. (1960). *Wave propagation and group velocity*. Academic Press.

Carlson, H. C. (1966). Ionospheric heating by magnetic conjugate-point photoelectrons. *Journal of Geophysical Research*, *71*(1), 195-199.

Danielson, J. R. (2002). *Measurement of Landau Damping of Electron Plasma Waves in the Linear and Trapping Regimes* (Doctoral dissertation). Retrieved from http://sdpha2.ucsd.edu/pdf_files/danielson_thesis.pdf

Djuth, F. T., Sulzer, M. P., & Elder, J. H. (1994). Application of the coded long-pulse technique to plasma line studies of the ionosphere. *Geophysical Research Letters*, *21*(24), 2725-2728.

Djuth, F. T., Sulzer, M. P., Elder, J. H., & Wickwar, V. B. (1997). High-resolution studies of atmosphere-ionosphere coupling at arecibo observatory, puerto rico. *Radio Science*, *32*(6), 2321-2344.

Djuth, F. T., Sulzer, M. P., Elder, J. H., Gonzales, S. A., Mathews, J. D., & Walterscheid, R. L. (2004). A continuum of gravity waves in the arecibo thermosphere?. *Geophysical Research Letters*, *31*.

Djuth, F. T., Sulzer, M. P., Zhang, L. D., Livneh, D. J., Mathews, J. D., Walterscheid, R. L., Seker, I., & Smith, S. M. (2010). Arecibo. *Journal of Geophysical Research*, *115*,

Dougherty, J. P., & Farley, D. T. (1960). A theory of incoherent scattering of radio waves by a plasma.*Proc. R. Soc. London*, *259*(1296), 79-99.

Evans, J. V., & Lowenthal, M. (1964). Ionospheric backscatter observations. *Planetary Space Science*,*12*, 915-944.

Evans, J. V. (1969). Theory and practice of ionosphere study by thomson scatter radar. *Proceedings of the IEEE*,*57*(4), 496-530.

Fejer, J. A. (1960). Scattering of radio waves by an ionized gas in thermal equilibrium. *Canadian Journal of Physics*, *38*, 1114-1133.

Gong, Y. (2012). Incoherent scatter study of dynamics in the ionosphere E- and F-region at Arecibo (A Master's thesis). Miami University, Oxford, OH.

Gong, Y., & Zhou, Q. (2011). Incoherent scatter radar study of the terdiurnal tide in the e- and f-region heights at arecibo. *Geophysical Research Letters*,*38*, 1-5. Retrieved from http://www.agu.org/pubs/crossref/2011/2011GL048318.shtml

Gordon, W. E. (1958). Incoherent scattering of radio waves by free electrons with applications to space exploration by radar. *Proceedings of the IRE*,*46*(11), 1824-1829.

Hagfors, T. USAF, Air Force Research Division. (1961).*Density fluctuations in a plasma in a magnetic field with applications to the ionosphere* (AD-248447). Arlington: Armed Services Technical Information Agency.

Kelley, M. (2008). *The earth's ionosphere*. (2nd ed., Vol. 96). Burlington, MA: Academic Press.

Knight, R. D. (2004). *Physics for scientists and engineers: A strategic approach with modern physics*. (2 ed.). Boston, MA: Addison-Wesley.

Landau, L. D. (1946). On the vibrations of the electronic plasma. *J Phys USSR*, *10*(25), 574.

Nicholls, M. J., Sulzer, M. P., Aponte, N., Seal, R., Nikoukar, R., & Gonzalez, S. A. (2006). High-resolution electron temperature measurements using the plasma line asymmetry. *Geophysical Research Letters*, *33*(L18107), 1-5.

Perkins, F. W., Salpeter, E. E., & Yngvesson, K. O. (1965). Incoherent scatter from plasma oscillations in the ionosphere. *Physical Review Letters*,*14*(15), 579-581.

Richards, M. A. (2005). *Fundamentals of radar signal processing*. (p. 59). New York, NY: McGraw-Hill.

Salpeter, E. E. (1960). Electron density fluctuations in a plasma. *Physical Review*, *120*(5), 1528-1535.

Salpeter, E. E. (1961). Energy and pressure of a zero-temperature plasma. *The Astrophysical Jounal*,*134*(3), 669-682.

Stix, T. H. (1962). *The theory of plasma waves*. New York, NY: McGraw-Hill.

Sulzer, M. P. (1986). A radar technique for high range resolution incoherent scatter autocorrelation function measurements utilizing the full average power of klystron radars. *Radio Science*, *21*(6), 1033-1040.

Thomson, J. J. (1906). *Conductivity of electricity through gases*. Cambridge, England: Cambridge University Press.

Tonks, L., & Langmuir, I. (1929). Oscillations in ionized gases.*Physical Review*, *33*, 195-211.

Trulsen, J., & Bjorna, N. (1978). Influence of electrostatic electron waves on the incoherent scattering cross-section. *Physica Scripta*, *17*, 11-14.

Woodman, R.F., Incoherent scattering of electromagnetic waves by a plasma. Ph.D. dissertation, Harvard Univ., Cambridge, MA, 1967.

Yngvesson, K. O., & Perkins, F. W. (1968). Radar thomson scatter studies of photoelectrons in the ionosphere and landau damping. *Journal of Geophysical Research*, *73*(1), 97-110.

APPENDICES

APPENDIX I – SCRIPTS USED

Global Method – plasmalineoverHeightandTime2.m

```
function[single_image_heights]=plasmalineoverHeightandTime2(fname)
% Reads in Coded Long Pulse plasma line spectra computed by ASP
% from the Echotek system (new header not equal to VME header)
fid=fopen(fname,'r','b');
sphdr=fread(fid,1024,'float32');
if (sphdr(1) < 2000) | (sphdr(1) > 2.1e6)   % not a big endian file
 fclose(fid);
 fid=fopen(fname,'r','l');
 sphdr=fread(fid,1024,'float');
end
dates=sphdr(1);
dtimes=sphdr(2)
nhts=sphdr(3);
nfft=sphdr(4);

sps=fread(fid,inf,'float32');
spsa=fftshift(reshape(sps(1:nhts*nfft),nfft,nhts),1);
spsb=fftshift(reshape(sps(nhts*nfft+1:end),nfft,nhts),1);
fclose(fid);

freq_res1 = 5e6/4095;
added_freq1 = 0:freq_res1:5e6;
added_freq2 = -5e6:freq_res1:0;
x_axis1 = 3e6 + added_freq1;
x_axis2 = -3e6 + added_freq2;
y_axis = (((600e-6+((1:2250)*5/(5e6)))*((3e8)/2))*cosd(15));
ave2 = mean(spsb(:,2200:2250),2); % remove baseline noise
spsb = spsb-ave2(:,ones(1,2250));
ave1 = mean(spsa(:,2200:2250),2);
spsa = spsa-ave1(:,ones(1,2250));
x = 1:4096;
x = x';
newSpsa = zeros(4096,2250);
newSpsb = zeros(4096,2250);
tic
spectralWidtha = zeros(1,2250);
spectralWidthb = zeros(1,2250);
for i = 1:2250
spsacoeffs = polyfit(x,spsa(:,i),30);
spsbcoeffs = polyfit(x,spsb(:,i),30);
spsafit = polyval(spsacoeffs,x);% establist clutter
spsbfit = polyval(spsbcoeffs,x);

 detrendedSpsa = spsa(:,i)-spsafit;
 detrendedSpsb = spsb(:,i)-spsbfit;
 [I0spsa x0spsa] = max(detrendedSpsa(1:end));
 [I0spsb x0spsb] = max(detrendedSpsb(1:end));
 c1(i) = I0spsa/(ave1(x0spsa)); c2(i) = I0spsb/(ave2(x0spsb)); i1(i) = x0spsa; i2(i) =
x0spsb;
 firstHalfSpsa = fliplr(detrendedSpsa(x0spsa:-1:1));
 secondHalfSpsa = detrendedSpsa(x0spsa+1:end);
```

```
 firstHalfSpsb = fliplr(detrendedSpsb(x0spsb:-1:1));
 secondHalfSpsb = detrendedSpsb(x0spsb+1:end);

 firstHalfWidtha = intersect(find(diff(firstHalfSpsa) > 0),find(firstHalfSpsa < 0));
 if(isempty(firstHalfWidtha))
     firstHalfWidtha = 1;
 else
     firstHalfWidtha = firstHalfWidtha(1);
 end
 secondHalfWidtha = intersect(find(diff(secondHalfSpsa) > 0),find(secondHalfSpsa < 0));
 if(isempty(secondHalfWidtha))
     secondHalfWidtha = 0;
 else
     secondHalfWidtha = secondHalfWidtha(1);
 end
 totalWidthIndicesa = x0spsa-(firstHalfWidtha-1):x0spsa+secondHalfWidtha;
 spectralWidtha(i) = length(totalWidthIndicesa);

 mask = zeros(4096,1);
 mask(totalWidthIndicesa) = 1;
 newSpsa(:,i) = mask.*detrendedSpsa;


 firstHalfWidthb = intersect(find(diff(firstHalfSpsb) > 0),find(firstHalfSpsb < 0));
 if(isempty(firstHalfWidthb))
     firstHalfWidthb = 1;
 else
     firstHalfWidthb = firstHalfWidthb(1);
 end
 secondHalfWidthb = intersect(find(diff(secondHalfSpsb) > 0),find(secondHalfSpsb < 0));
 if(isempty(secondHalfWidthb))
     secondHalfWidthb = 0;
 else
     secondHalfWidthb = secondHalfWidthb(1);
 end
 totalWidthIndicesb = x0spsb-(firstHalfWidthb-1):x0spsb+secondHalfWidthb;
 spectralWidthb(i) = length(totalWidthIndicesb);

 mask = zeros(4096,1);
 mask(totalWidthIndicesb) = 1;
 newSpsb(:,i) = mask.*detrendedSpsb;


end

whos
single_image_heights = [c1' i1' spectralWidtha' c2' i2' spectralWidthb'];
```

Lorentzian Method – plasmalineoverHeightandTime.m

```
function[single_image_heights]=plasmalineoverHeightandTime(fname)
% Reads in Coded Long Pulse plasma line spectra computed by ASP
% from the Echotek system (new header not equal to VME header)
fid=fopen(fname,'r','b');
sphdr=fread(fid,1024,'float32');
if (sphdr(1) < 2000) | (sphdr(1) > 2.1e6)   % not a big endian file
 fclose(fid);
 fid=fopen(fname,'r','l');
 sphdr=fread(fid,1024,'float');
end
dates=sphdr(1);
dtimes=sphdr(2)
nhts=sphdr(3);
nfft=sphdr(4);

sps=fread(fid,inf,'float32');
spsa=fftshift(reshape(sps(1:nhts*nfft),nfft,nhts),1);
%spsb=fftshift(reshape(sps(nhts*nfft+1:end),nfft,nhts),1);
fclose(fid);

ave = mean(spsa(:,2200:2250),2);
spsa = spsa-ave(:,ones(1,2250));
x = 1:4096;
x = x';
newSpsa = zeros(4096,2250);
spectralWidth = zeros(1,2250);

frequency = zeros(1,2250);
intensity = zeros(1,2250);
for i = 1:2250
spsacoeffs = polyfit(x,spsa(:,i),30);
spsafit = polyval(spsacoeffs,x);% establist clutter
detrendedSpsa = spsa(:,i)-spsafit;


[I0spsa x0spsa] = max(detrendedSpsa(1:end));

firstHalfSpsa = fliplr(detrendedSpsa(x0spsa:-1:1));
secondHalfSpsa = detrendedSpsa(x0spsa+1:end);

firstHalfWidth = intersect(find(diff(firstHalfSpsa) > 0),find(firstHalfSpsa < 0));
if(isempty(firstHalfWidth))
    firstHalfWidth = 1;
else
    firstHalfWidth = firstHalfWidth(1);
end
secondHalfWidth = intersect(find(diff(secondHalfSpsa) > 0),find(secondHalfSpsa < 0));
if(isempty(secondHalfWidth))
    secondHalfWidth = 0;
else
    secondHalfWidth = secondHalfWidth(1);
end
totalWidthIndices = x0spsa-(firstHalfWidth-1):x0spsa+secondHalfWidth;
spectralWidth(i) = length(totalWidthIndices)*(5e6/4096);

  if(totalWidthIndices(1) <= 5)
     a = 1;
     b = totalWidthIndices(end)+5;
  elseif (totalWidthIndices(end) >=4091)
      a = totalWidthIndices(1)-5;
```

```
      b = 4096;
  else
      a = totalWidthIndices(1)-5;
      b = totalWidthIndices(end)+5;
  end

 predictor = a:b;
 indicator = detrendedSpsa(predictor);
 xnaught = sum(predictor*indicator)/sum(indicator);
 predictor1 = ((a:b) * (5e6/4096)) - (8e6 + 5e6/4096);
 xnaught = (xnaught * 5e6/4096) - (8e6 + 5e6/4096); %SPSA
 %xnaught = (xnaught* 5e6/4096) + 3e6; %SPSB
 scaleFactor = 1e-16;
 indicator = indicator*scaleFactor;
 xinit = [1e19,1e4];
 xinit(1) = xinit(1) * scaleFactor;
 lorentzCoeffs = ...
    lsqcurvefit(@(parameters,xdata)lorentz(xdata,parameters,xnaught),...
    xinit, predictor1, indicator' );
 yFit = lorentz(predictor1,lorentzCoeffs,xnaught);
 lorentzIntensity = lorentz(xnaught,lorentzCoeffs,xnaught);
 yFit = yFit/scaleFactor;
 indicator = indicator/scaleFactor;
 lorentzIntensity = lorentzIntensity/scaleFactor;
 lorentzCoeffs(1) = lorentzCoeffs(1)/scaleFactor;
 detrendedSpsb(predictor) = yFit;
 intensity(i) = lorentzIntensity;
 frequency(i) = xnaught;
mask = zeros(4096,1);
mask(totalWidthIndices) = 1;
newSpsa(:,i) = mask.*detrendedSpsa;
end
for j = 1:2250
       freqfloor = (frequency(j)- (3e6))*4096/5e6;
       freqfloor = mod(floor(freqfloor),4096);
       if(freqfloor == 0)
              freqfloor = 4096;
              freqceil = 1;
       else
              freqceil = freqfloor+1;
       end
       intensity(j) = intensity(j)/((ave(freqfloor)+ave(freqceil))/2);
end

single_image_heights = [intensity' frequency' spectralWidth'];


end


function y = lorentz( x, parameters, x0 )
% note that x (the x-axis data) can be a vector

% rename for clarity
a = parameters(1);
w = parameters(2);

numerator = a * ones( size(x) );
temp = ( x - x0 ) / w;
denominator = 1 + temp.*temp;
y = numerator ./ denominator;
end
```

Moments Method – plasmalineoverHeightandTime.m

```
function[single_image_heights]=readplspec(fname)
%function[hts,dtimes,sps,azs,zen,dates]=readplspec(fname)
% Reads in Coded Long Pulse plasma line spectra computed by ASP
% from the Echotek system (new header not equal to VME header)
fid=fopen(fname,'r','b');
sphdr=fread(fid,1024,'float32');
if (sphdr(1) < 2000) | (sphdr(1) > 2.1e6)   % not a big endian file
 fclose(fid);
 fid=fopen(fname,'r','l');
 sphdr=fread(fid,1024,'float');
end
dates=sphdr(1);
dtimes=sphdr(2)
nhts=sphdr(3);
nfft=sphdr(4);

sps=fread(fid,inf,'float32');
spsa=fftshift(reshape(sps(1:nhts*nfft),nfft,nhts),1);
spsb=fftshift(reshape(sps(nhts*nfft+1:end),nfft,nhts),1);
fclose(fid);
freq_res1 = 5e6/4095;
added_freq1 = 0:freq_res1:5e6;
added_freq2 = -5e6:freq_res1:0;
x_axis1 = 3e6 + added_freq1;
x_axis2 = -3e6 + added_freq2;
y_axis = (((600e-6+((1:2250)*5/(5e6)))*((3e8)/2))*cosd(15));
ave2 = mean(spsb(:,2200:2250),2); % remove baseline noise
spsb = spsb-ave2(:,ones(1,2250));
ave1 = mean(spsa(:,2200:2250),2);
spsa = spsa-ave1(:,ones(1,2250));
x = 1:4096;
x = x';
newSpsa = zeros(4096,2250);
newSpsb = zeros(4096,2250);
tic
spectralWidtha = zeros(1,2250);
spectralWidthb = zeros(1,2250);
for i = 1:2250
spsacoeffs = polyfit(x,spsa(:,i),30);
spsbcoeffs = polyfit(x,spsb(:,i),30);
spsafit = polyval(spsacoeffs,x);% establist clutter
spsbfit = polyval(spsbcoeffs,x);

 detrendedSpsa = spsa(:,i)-spsafit;
 detrendedSpsb = spsb(:,i)-spsbfit;
[I0spsa x0spsa] = max(detrendedSpsa(1:end));
 [I0spsb x0spsb] = max(detrendedSpsb(1:end));

 firstHalfSpsa = fliplr(detrendedSpsa(x0spsa:-1:1));
 secondHalfSpsa = detrendedSpsa(x0spsa+1:end);

 firstHalfSpsb = fliplr(detrendedSpsb(x0spsb:-1:1));
 secondHalfSpsb = detrendedSpsb(x0spsb+1:end);

 firstHalfWidtha = intersect(find(diff(firstHalfSpsa) > 0),find(firstHalfSpsa < 0));
 if(isempty(firstHalfWidtha))
     firstHalfWidtha = 1;
 else
     firstHalfWidtha = firstHalfWidtha(1);
```

```
 end
 secondHalfWidtha = intersect(find(diff(secondHalfSpsa) > 0),find(secondHalfSpsa < 0));
 if(isempty(secondHalfWidtha))
     secondHalfWidtha = 0;
 else
     secondHalfWidtha = secondHalfWidtha(1);
 end
 totalWidthIndicesa = x0spsa-(firstHalfWidtha-1):x0spsa+secondHalfWidtha;
 spectralWidtha(i) = length(totalWidthIndicesa);

 mask = zeros(4096,1);
 mask(totalWidthIndicesa) = 1;
 newSpsa(:,i) = mask.*detrendedSpsa;


 firstHalfWidthb = intersect(find(diff(firstHalfSpsb) > 0),find(firstHalfSpsb < 0));
 if(isempty(firstHalfWidthb))
     firstHalfWidthb = 1;
 else
     firstHalfWidthb = firstHalfWidthb(1);
 end
 secondHalfWidthb = intersect(find(diff(secondHalfSpsb) > 0),find(secondHalfSpsb < 0));
 if(isempty(secondHalfWidthb))
     secondHalfWidthb = 0;
 else
     secondHalfWidthb = secondHalfWidthb(1);
 end
 totalWidthIndicesb = x0spsb-(firstHalfWidthb-1):x0spsb+secondHalfWidthb;
 spectralWidthb(i) = length(totalWidthIndicesb);

 mask = zeros(4096,1);
 mask(totalWidthIndicesb) = 1;
 newSpsb(:,i) = mask.*detrendedSpsb;


end

c1 = zeros(1,2250); c2 = zeros(1,2250); i1 = zeros(1,2250); i2 = zeros(1,2250);
spectralWidth1 = zeros(1,2250); spectralWidth2 = zeros(1,2250);

for i = 1:2250
    currVec = newSpsa(:,i);
    predictor = find(currVec)';
    indicator = currVec(predictor)';
    i1(i) = (predictor*indicator')/(sum(indicator));
    for j = 1:length(predictor)
        tempstorer1(j) = ((predictor(j)-i1(i))^2)*indicator(j);
        tempstorer2(j) = indicator(j);
    end
    c1(i) = max(currVec);
    spectralWidth1(i) = sqrt(abs(sum(tempstorer1)/sum(tempstorer2)));
    clear tempstorer1; clear tempstorer2;
    currVec = newSpsb(:,i);
    predictor = find(currVec)';
    indicator = currVec(predictor)';
    i2(i) = (predictor*indicator')/(sum(indicator));
    for j = 1:length(predictor)
        tempstorer1(j) = ((predictor(j)-i2(i))^2)*indicator(j);
        tempstorer2(j) = indicator(j);
    end
    c2(i) = max(currVec);
    spectralWidth2(i) = sqrt(abs(sum(tempstorer1)/sum(tempstorer2)));
```

```
end

c1 = c1./(ave1(mod(ceil(i1),4096)+1)');
c2 = c2./(ave2(mod(ceil(i2),4096)+1)');

single_image_heights = [c1' i1' spectralWidth1' c2' i2' spectralWidth2'];
end
```

Driver Program – PEPLintensity.m

```
clear all
% for production use, replace this with the path to the shared directory
% to be on the safe side, rename the directory names that have empty
% spaces in it
baseString='/shared/zhouq_shared/T2483spectra/January162010/t2483_16jan2010_s555e972_';
left = getenv('LEFTARG');
right = getenv('RIGHTARG');
procnum = getenv('PROC');
leftBound = str2num(left);
rightBound=str2num(right);
size=rightBound-leftBound+1
intensities = zeros(size,2250);
frequencies = zeros(size,2250);
widths = zeros(size,2250);

k=1;
for i=leftBound:rightBound
    if i>999
        myFileString=strcat(baseString,num2str(i));
    elseif i>99 && i<1000
        myFileString=strcat(baseString,'0',num2str(i));
    elseif i>9 && i<100
        myFileString=strcat(baseString,'00',num2str(i));
    else
        myFileString=strcat(baseString,'000',num2str(i));
    end
    allInformation = plasmalineoverHeightandTime(myFileString);
    intensities(k,:) = allInformation(:,1);
    frequencies(k,:) = allInformation(:,2);
    widths(k,:) = allInformation(:,3);
    k=k+1;
%    imagesc(intensities)
end
%write to file
save(strcat('intensities_',num2str(procnum),'.mat'),'intensities','-mat');
save(strcat('frequencies_',num2str(procnum),'.mat'),'frequencies','-mat');
save(strcat('widths_',num2str(procnum),'.mat'),'widths','-mat');
%% serially (in one single instance of Matlab)
%% if processing less than 4257 files, you need to
%% adjust the allocation for the total intensities
% total=zeros(4257,2250);
%for i=1:numprocs
%   mystring=strcat('intensities_',num2str(i));
%   load mystring % this brings in the variable 'intensities' for each
%   instance
%   total((i-1)*interval_size+1,i*interval_size)=intensities
%end
```

Shell Script - launchScripts.sh

```
#!/bin/bash -l

NumFiles=4257
StartIndex=0
num_procs=129
# use double brackets to evaluate
interval_size=$(($NumFiles/$num_procs))


for i in $(seq 1  1 $num_procs)
do

rm batchfile_$i


#determine the intervals


#define env variables



#write the file
echo "### name of the job" >> batchfile_$i
echo "#PBS -N Julio_script_$i" >> batchfile_$i
echo "#PBS -l walltime=80:00:00" >> batchfile_$i
echo "#PBS -l nodes=1:ppn=1" >> batchfile_$i
echo "#PBS -q batch" >> batchfile_$i
echo "module load matlab-r2012a" >> batchfile_$i

# generate portions of file indices to be processed by one Matlab instance
j=$(($i-1))
leftargA=$(($j*$interval_size))
leftarg=$(($StartIndex+$leftargA))
rightargA=$(($i*$interval_size-1))
rightarg=$(($StartIndex+$rightargA))
echo $leftarg
echo $rightarg


# these variable will be read in from within the matlab executable
echo export LEFTARG=$leftarg >> batchfile_$i
echo export RIGHTARG=$rightarg >> batchfile_$i
echo export PROC=$i >> batchfile_$i
echo pwd >> batchfile_$i
echo cd /shared/zhouq_shared/T2483spectra/January162010 >> batchfile_$i
echo pwd >> batchfile_$i
echo "time ./PEPLintensity2" >> batchfile_$i

qsub batchfile_$i

#make sure the env variables are properly read by matlab before the next job is
submitted

sleep 2
done
```

APPENDIX II – PROCESSED PLASMA LINE IMAGES

JANUARY 15TH, 2010

Plasma Line Frequencies

Downshifted

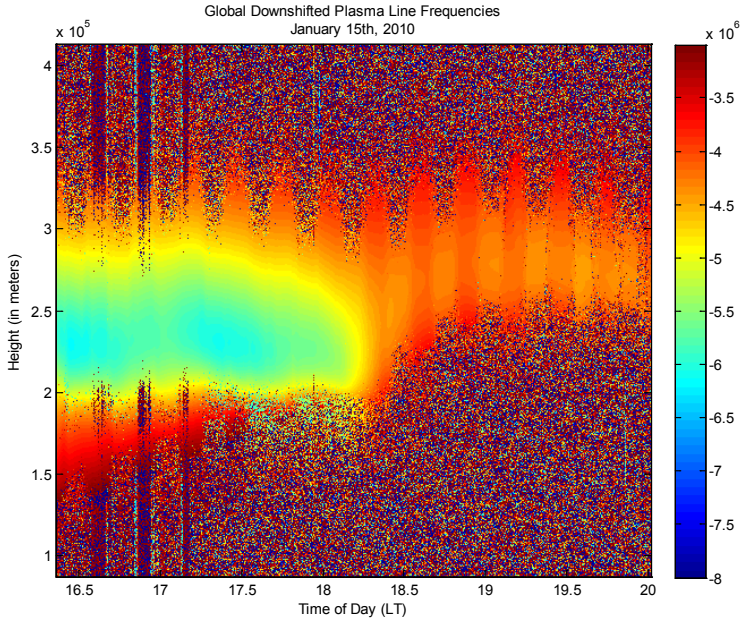

Figure 62: Global Downshifted Plasma Line Frequencies; January 15th, 2010.

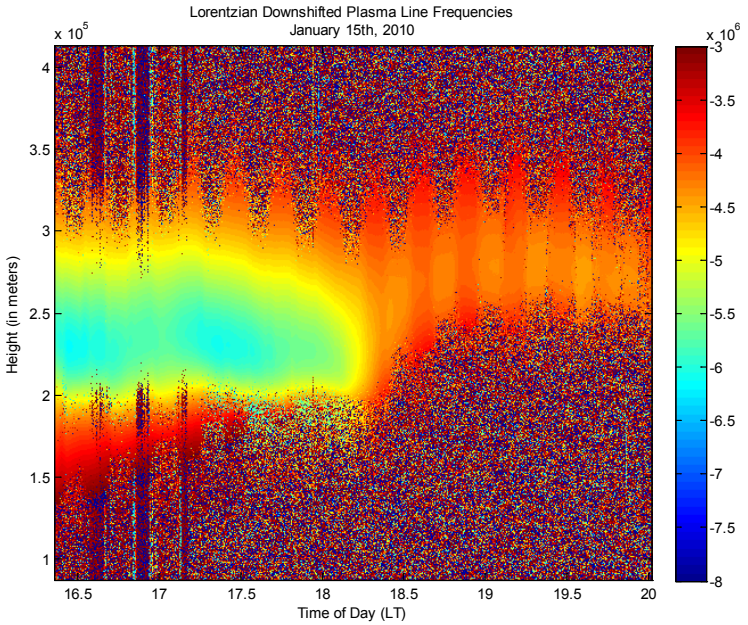

Figure 63: Lorentzian Downshifted Plasma Line Frequencies; January 15th, 2010.

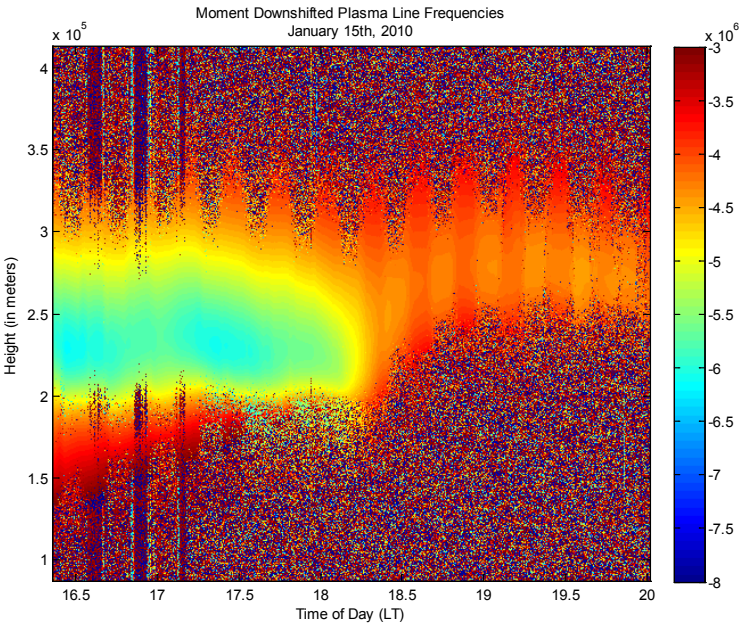

Figure 64: Moment Downshifted Plasma Line Frequencies; January 15th, 2010.

Plasma Line Intensities

Downshifted

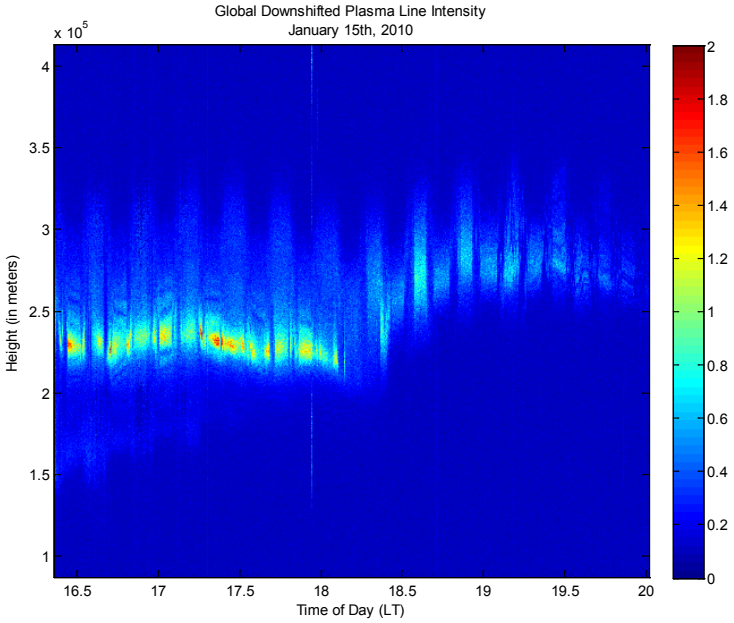

Figure 65: Global Downshifted Plasma Line Intensities; January 15th, 2010.

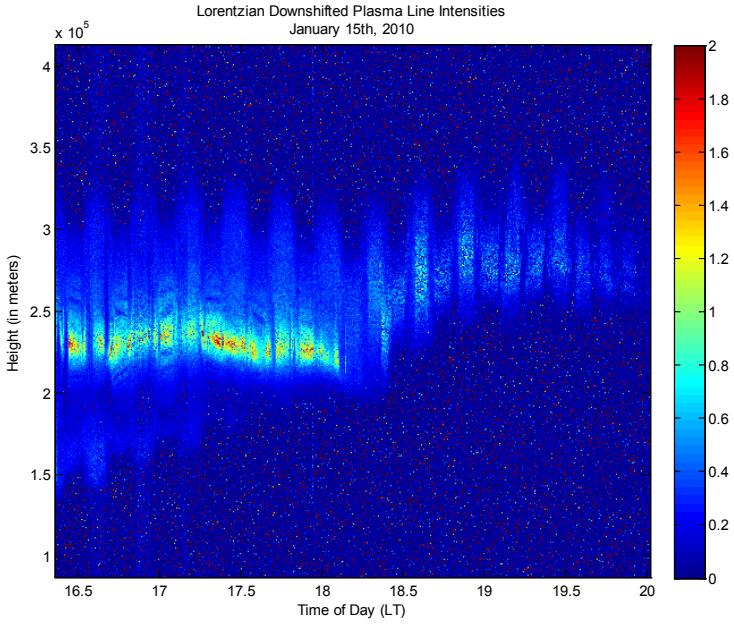

Figure 66: Lorentzian Downshifted Plasma Line Intensities; January 15th, 2010.

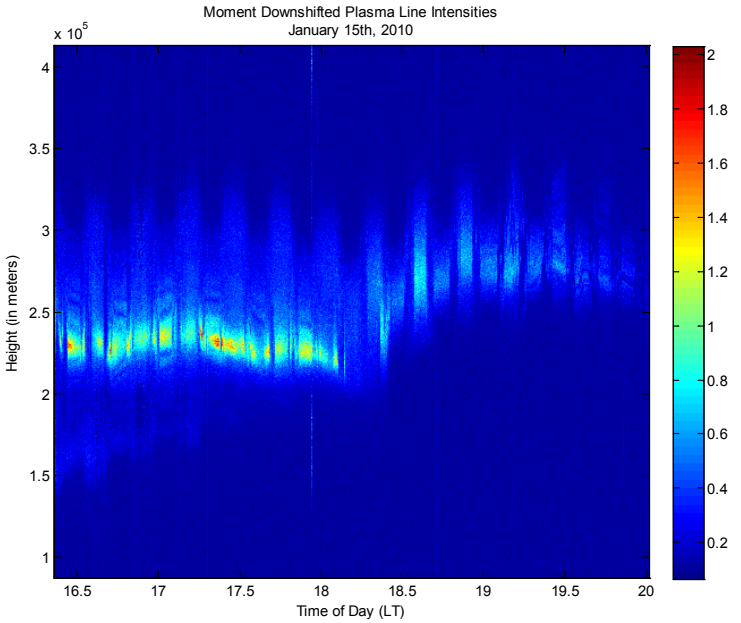

Figure 67: Moment Downshifted Plasma Line Intensities; January 15th, 2010.

Plasma Line Widths

Downshifted

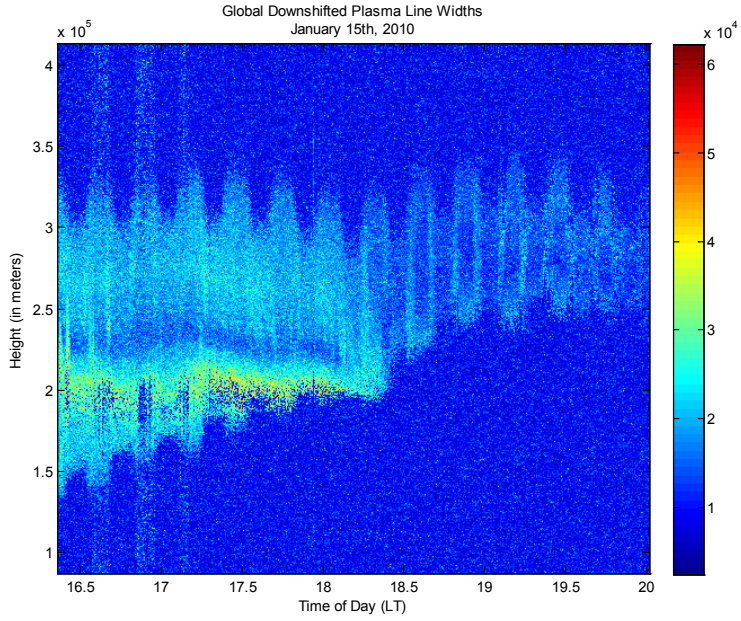

Figure 68: Global Downshifted Plasma Line Widths; January 15th, 2010.

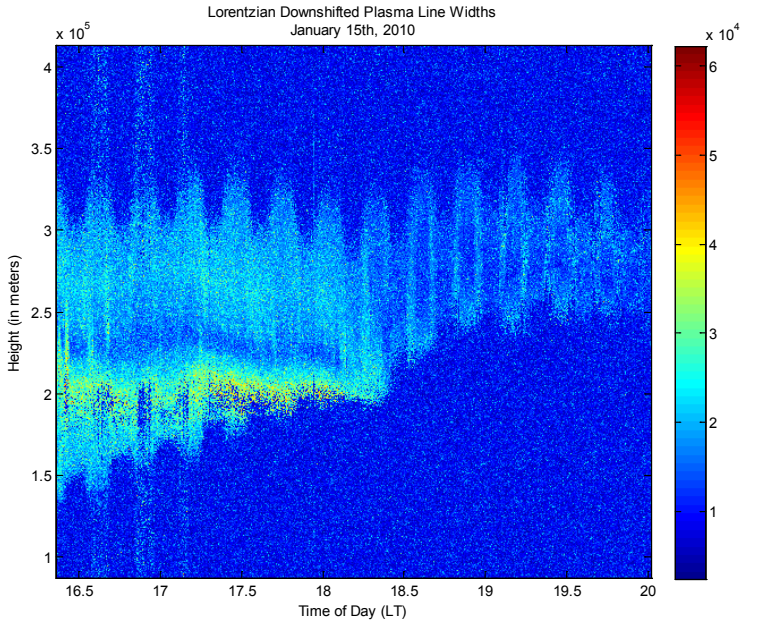

Figure 69: Lorentzian Downshifted Plasma Line Widths; January 15th, 2010.

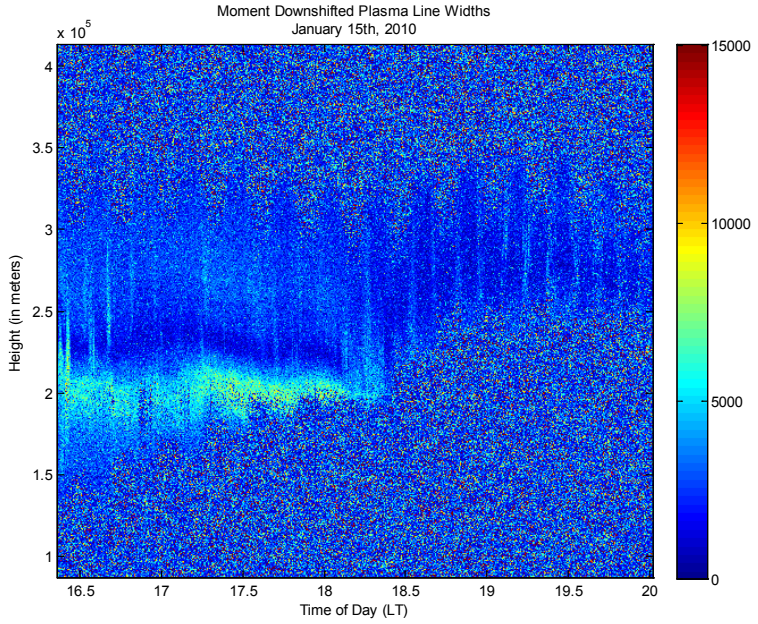

Figure 70: Moment Downshifted Plasma Line Widths; January 15th, 2010.

Plasma Line Frequencies

Upshifted

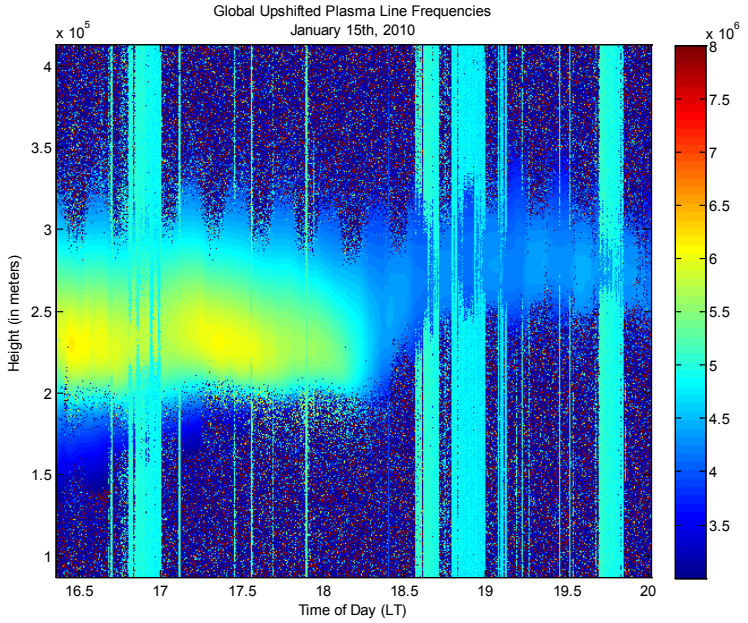

Figure 71: Global Upshifted Plasma Line Frequencies; January 15th, 2010.

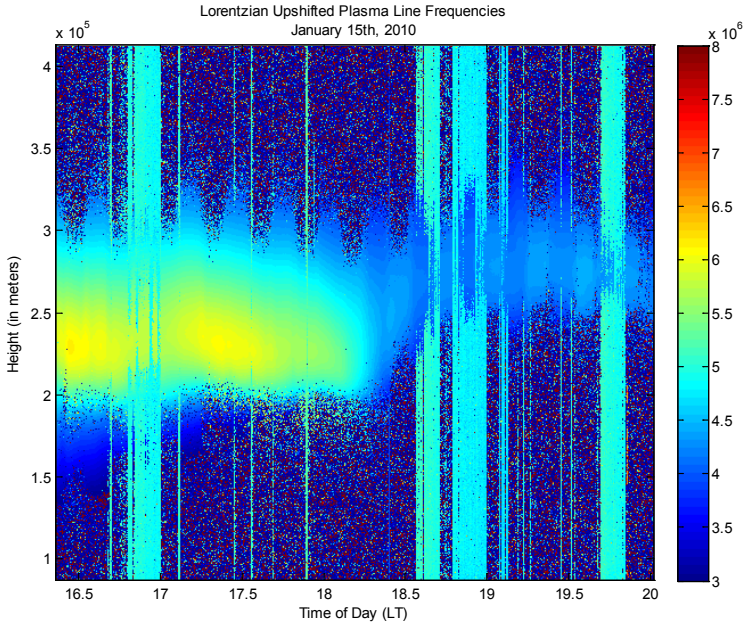

Figure 72: Lorentzian Upshifted Plasma Line Frequencies; January 15th, 2010.

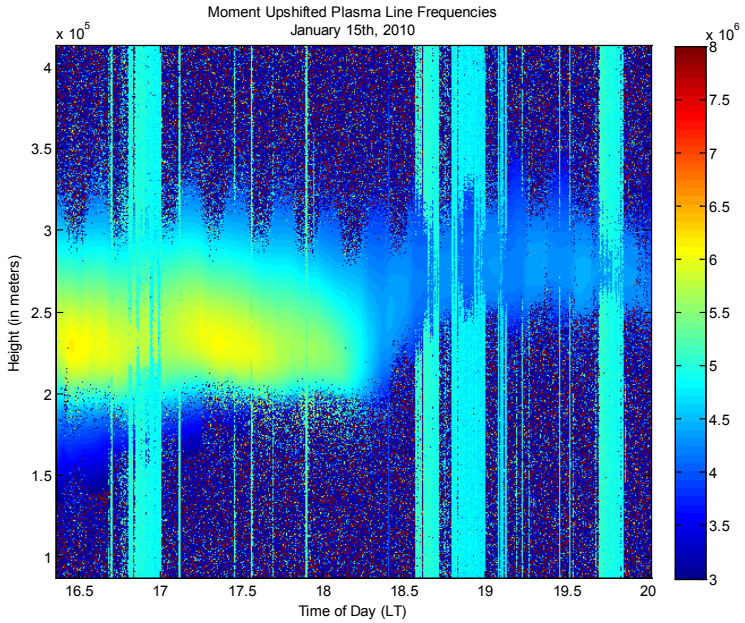

Figure 73: Moment Upshifted Plasma Line Frequencies, January 15th, 2010.

Plasma Line Intensities

Upshifted

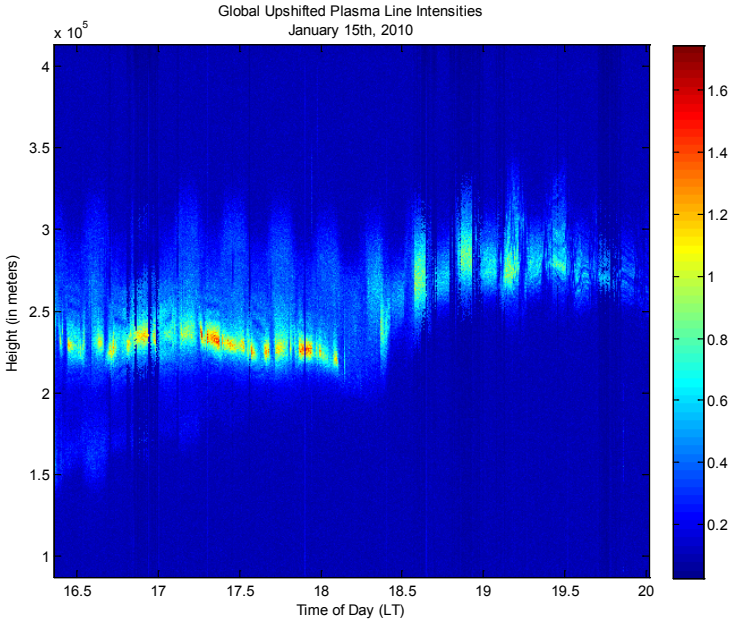

Figure 74: Global Upshifted Plasma Line Intensities; January 15th, 2010.

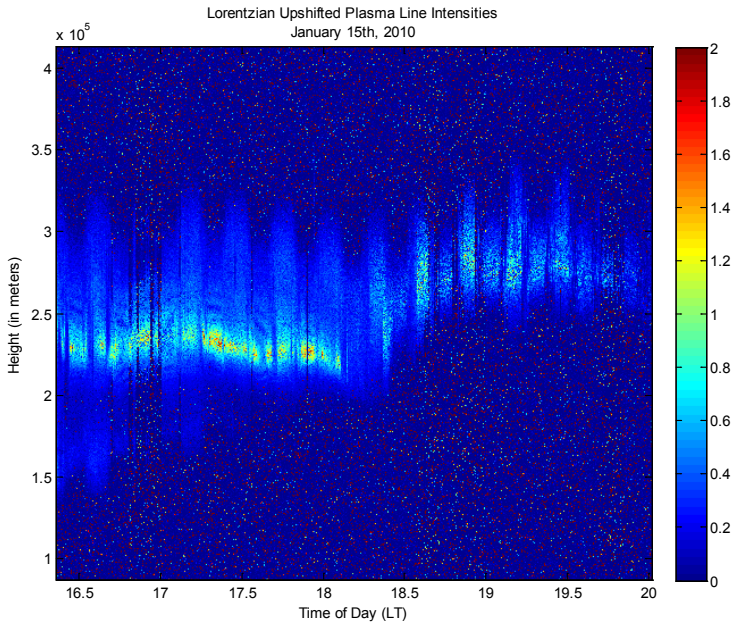

Figure 75: Lorentzian Upshifted Plasma Line Intensities; January 15th, 2010.

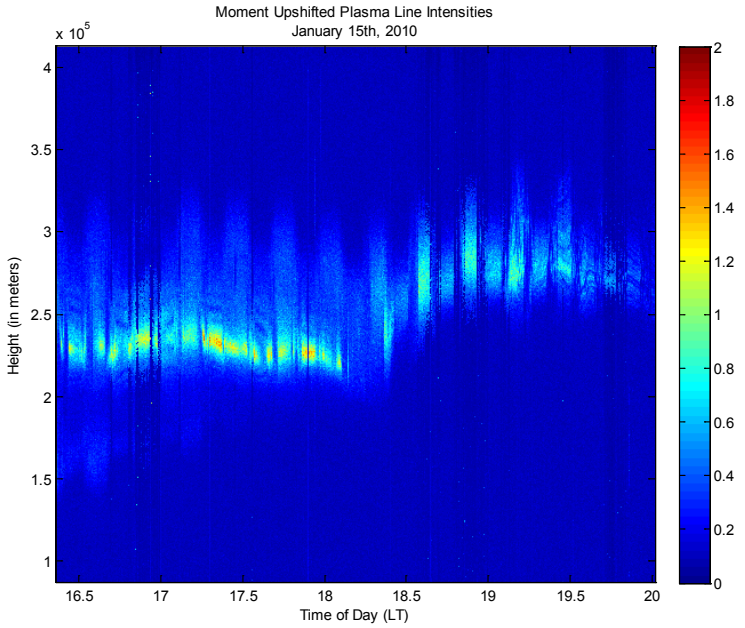

Figure 76: Moment Upshifted Plasma Line Intensities; January 15th, 2010.

Plasma Line Widths

Upshifted

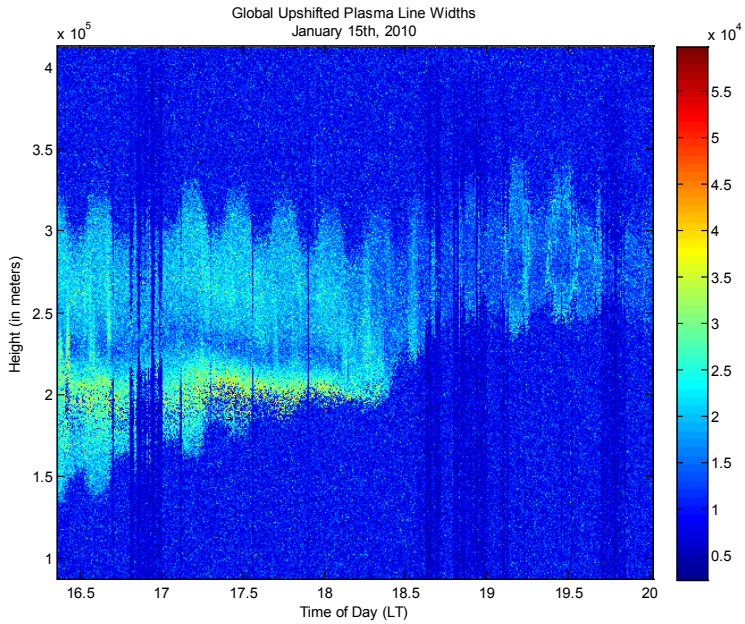

Figure 77: Global Upshifted Plasma Line Widths; January 15th, 2010.

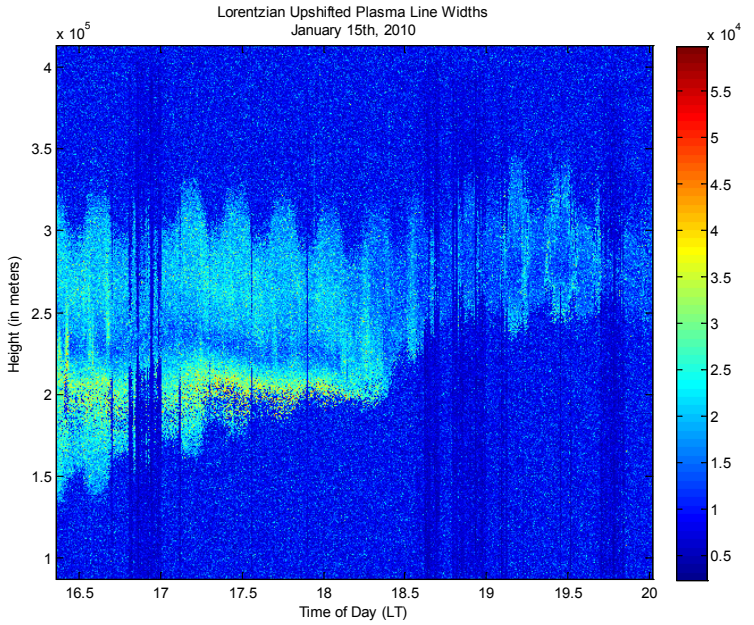

Figure 78: Lorentzian Upshifted Plasma Line Widths; January 15th, 2010.

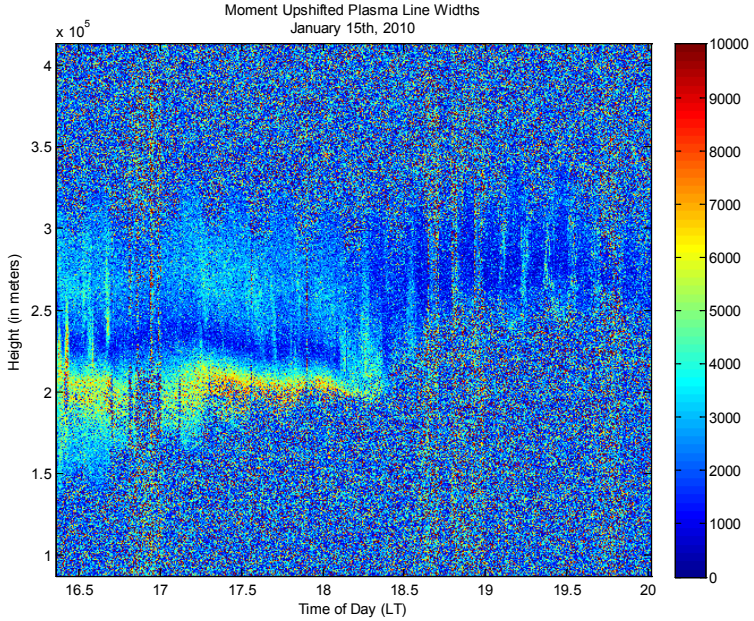

Figure 79: Moment Upshifted Plasma Line Widths; January 15th, 2010.

JANUARY 16TH, 2010

Plasma Line Frequencies

Downshifted

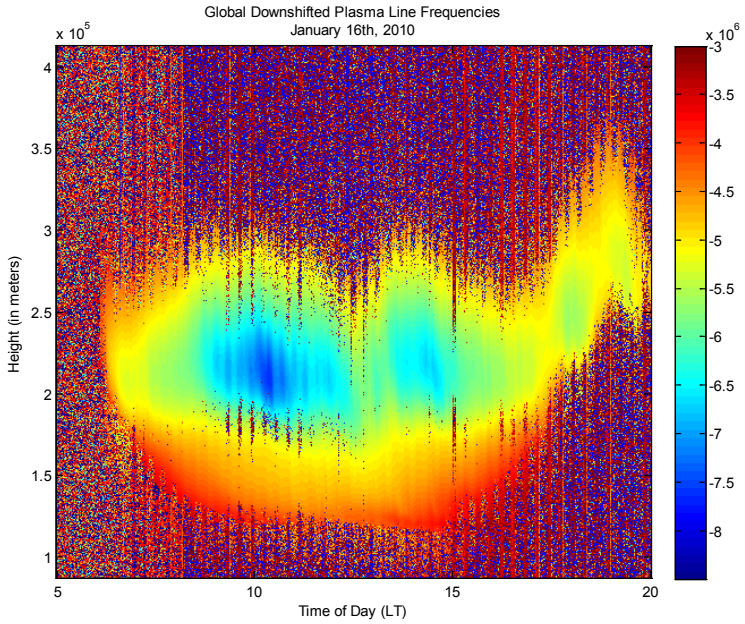

Figure 80: Global Downshifted Plasma Line Frequencies; January 16th, 2010.

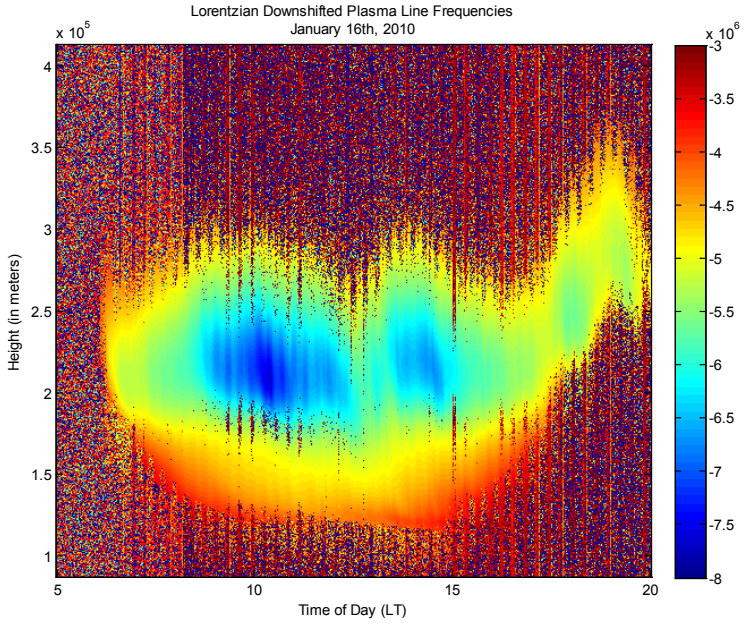

Figure 81: Lorentzian Downshifted Plasma Line Frequencies; January 16th, 2010.

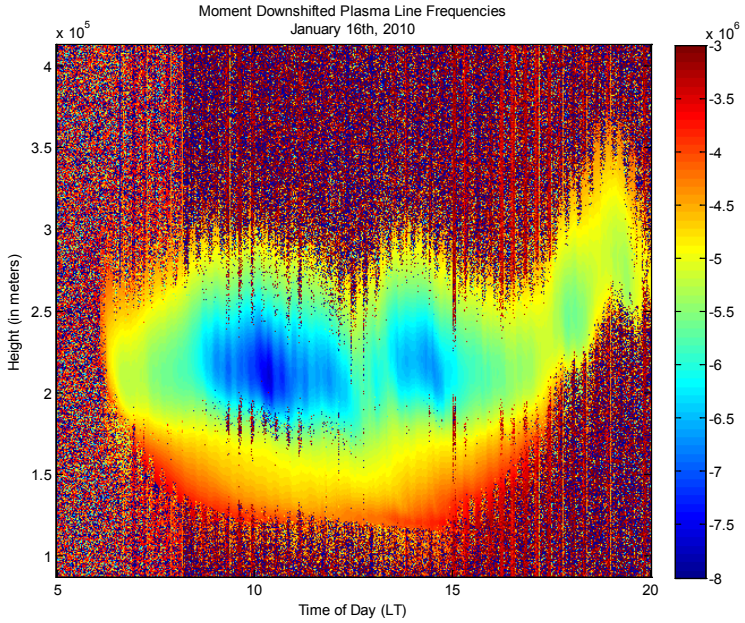

Figure 82: Moment Downshifted Plasma Line Frequencies; January 16th, 2010.

Plasma Line Intensities

Downshifted

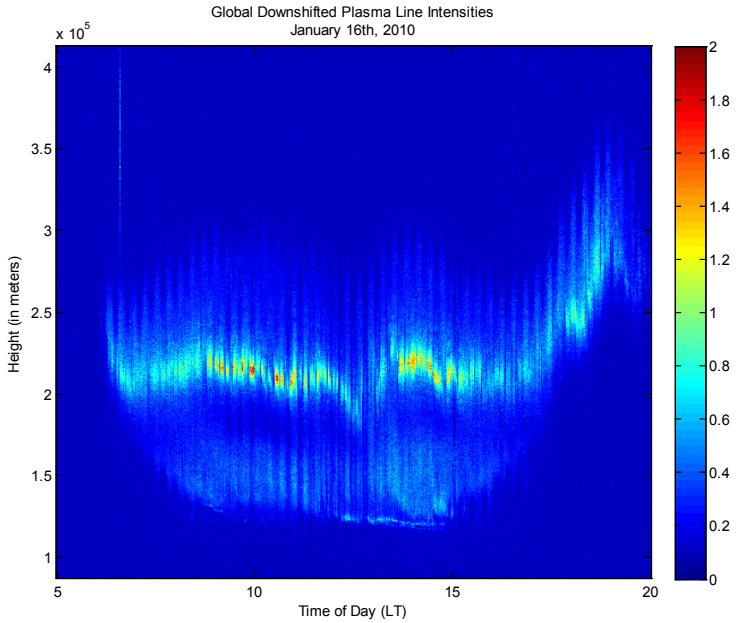

Figure 83: Global Downshifted Plasma Line Intensities; January 16th, 2010.

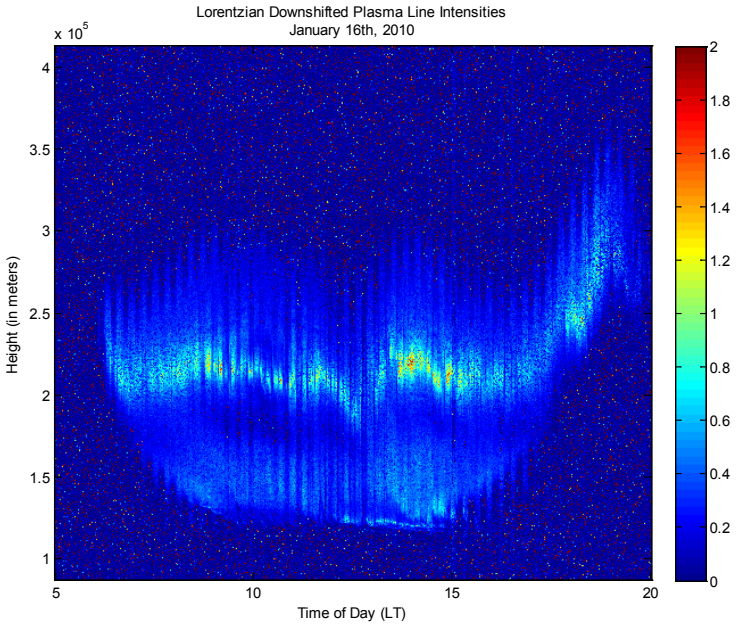

Figure 84: Lorentzian Downshifted Plasma Line Intensities; January 16th, 2010.

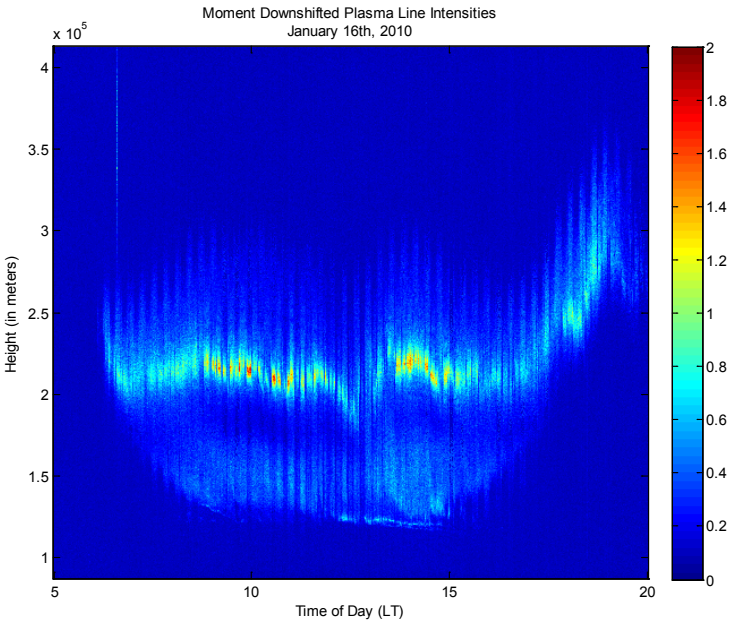

Figure 85: Moment Downshifted Plasma Line Intensities; January 16th, 2010.

Plasma Line Widths

Downshifted

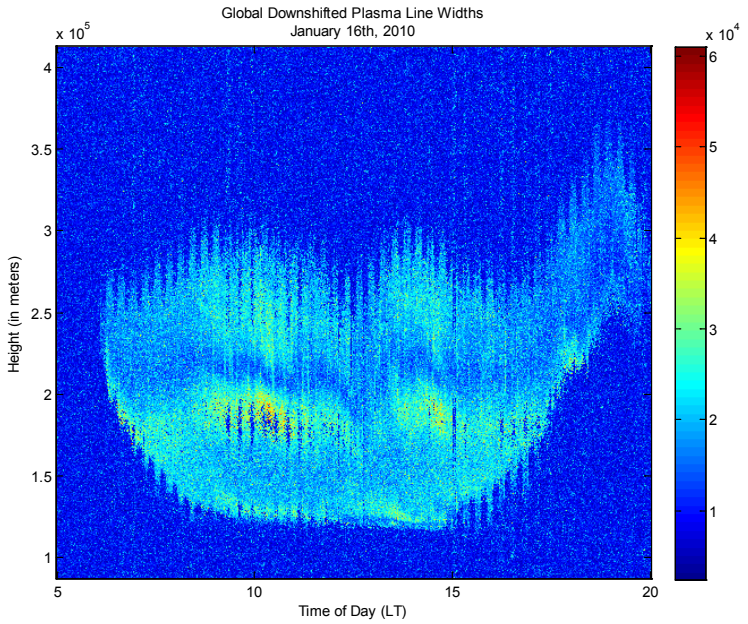

Figure 86: Global Downshifted Plasma Line Widths; January 16th, 2010.

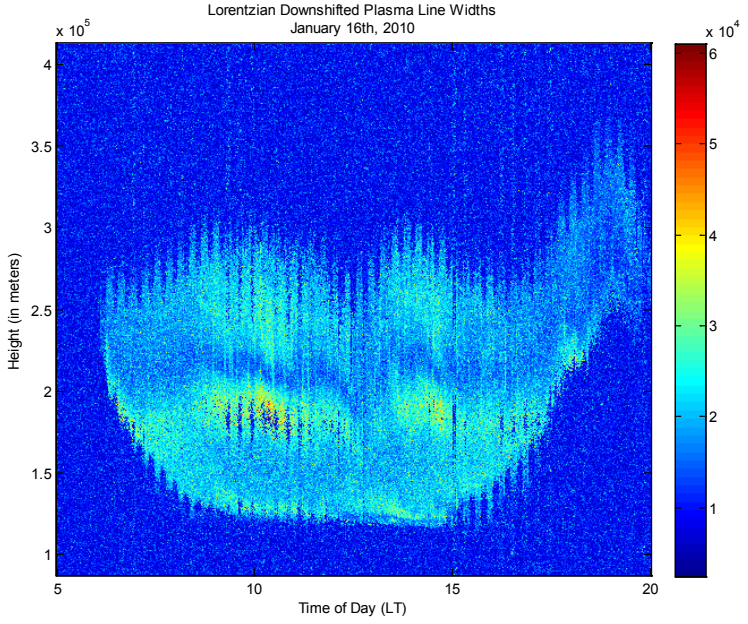

Figure 87: Lorentzian Downshifted Plasma Line Widths; January 16th, 2010.

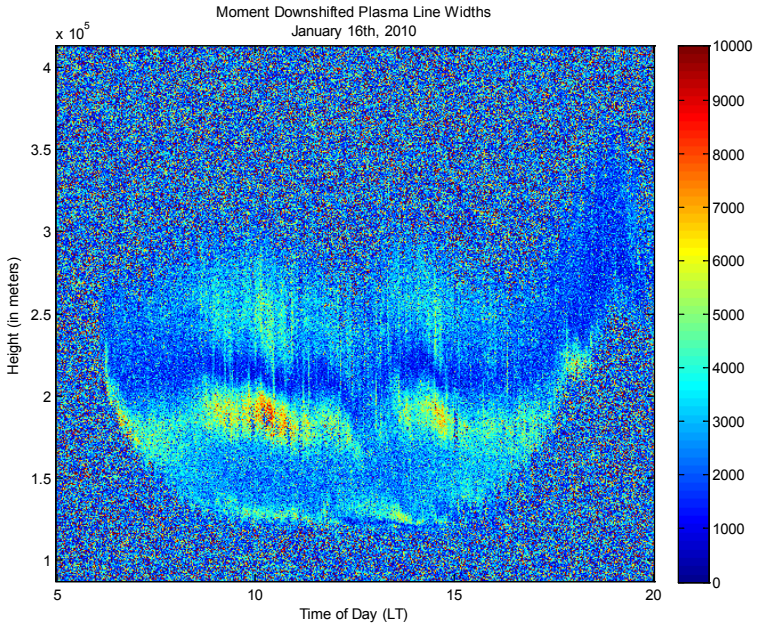

Figure 88: Moments Downshifted Plasma Line Widths; January 16th, 2010.

Plasma Line Frequencies

Upshifted

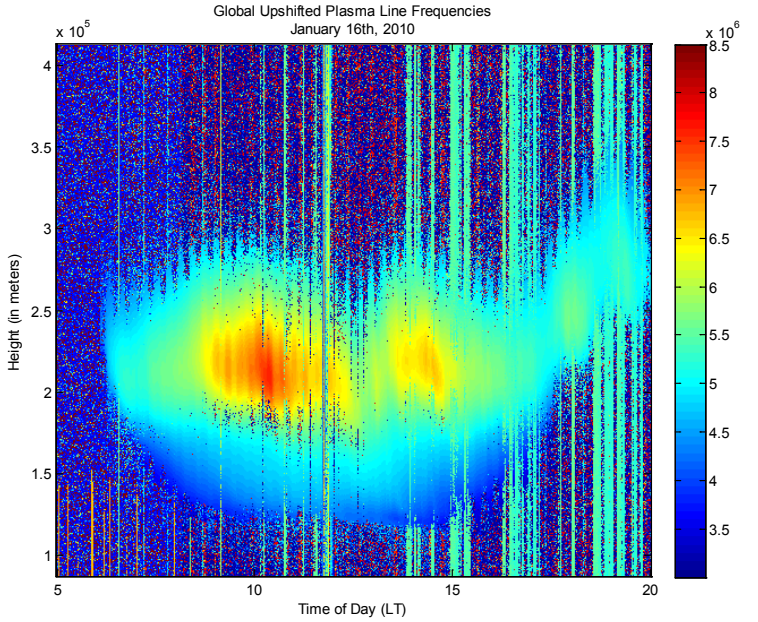

Figure 89: Global Upshifted Plasma Line Frequencies; January 16th, 2010.

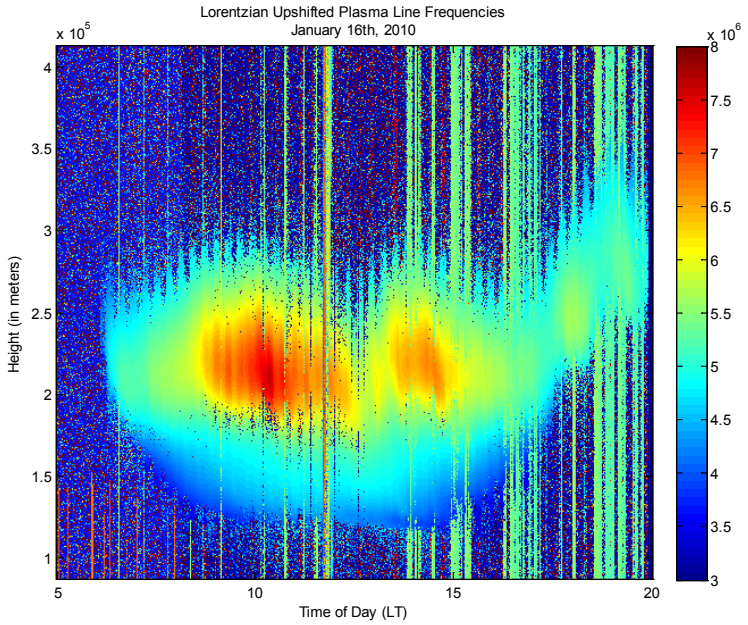

Figure 90: Lorentzian Upshifted Plasma Line Frequencies; January 16th, 2010.

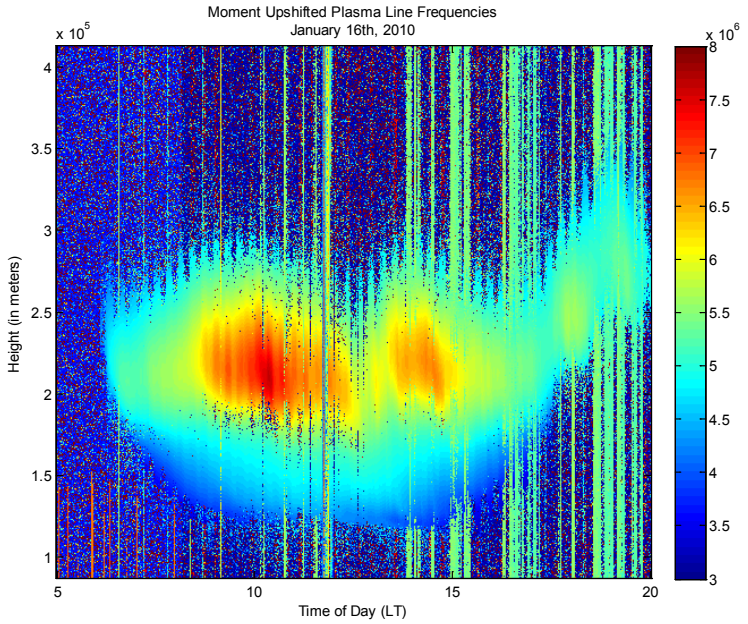

Figure 91: Moment Upshifted Plasma Line Frequencies; January 16th, 2010.

Plasma Line Intensities

Upshifted

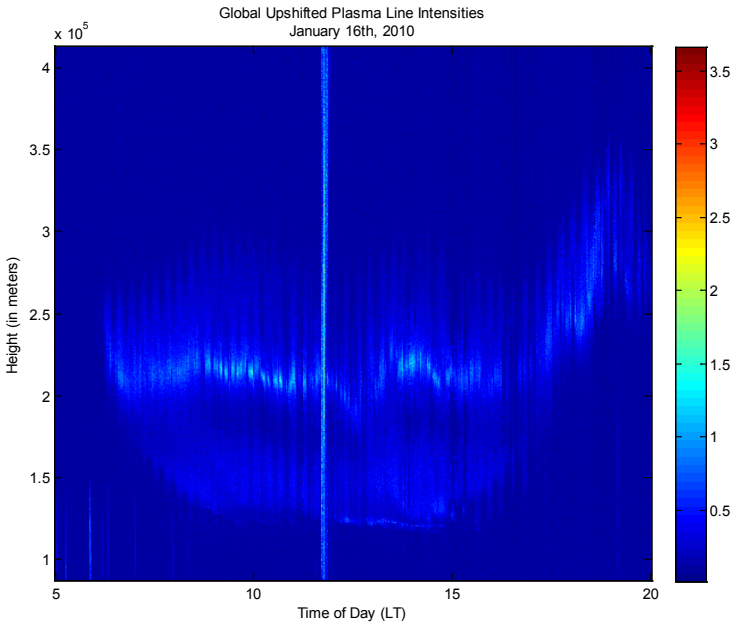

Figure 92: Global Upshifted Plasma Line Intensities; January 16th, 2010.

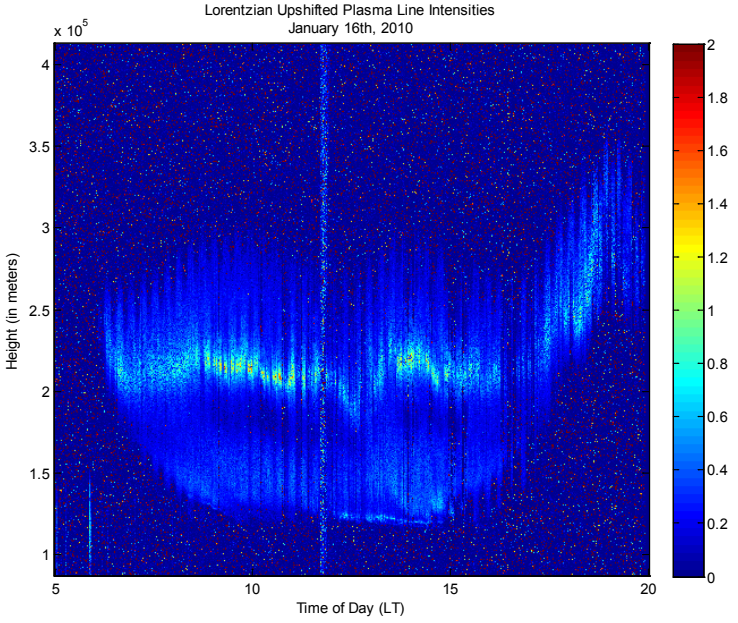

Figure 93: Lorentzian Upshifted Plasma Line Intensities; January 16th, 2010.

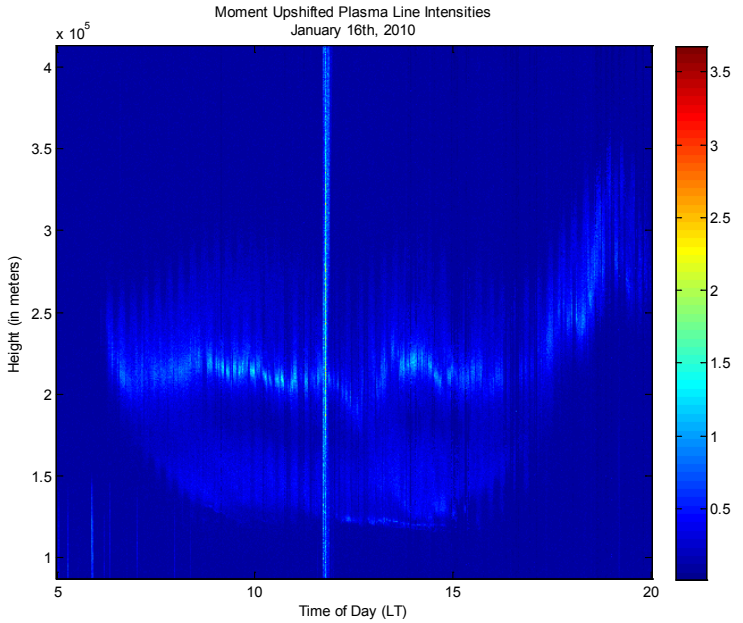

Figure 94: Moment Upshifted Plasma Line Intensities; January 16th, 2010.

Plasma Line Widths

Upshifted

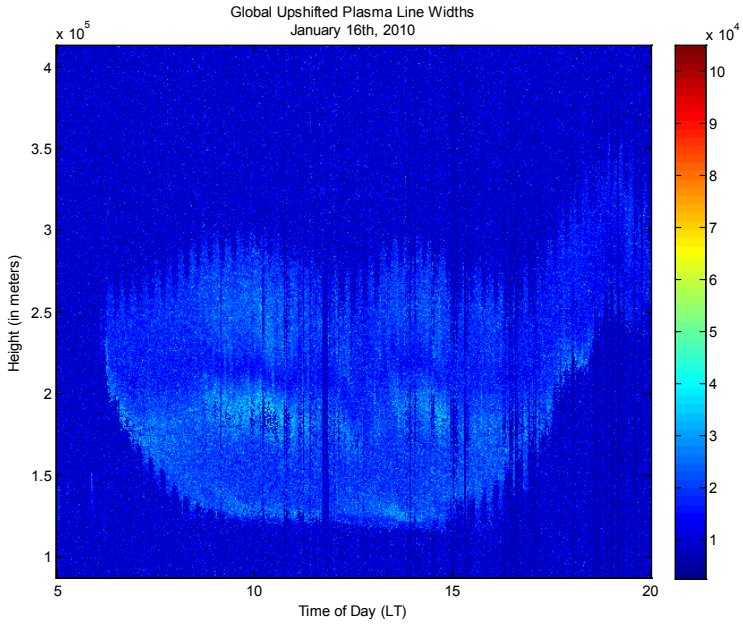

Figure 95: Global Upshifted Plasma Line Widths; January 16th, 2010.

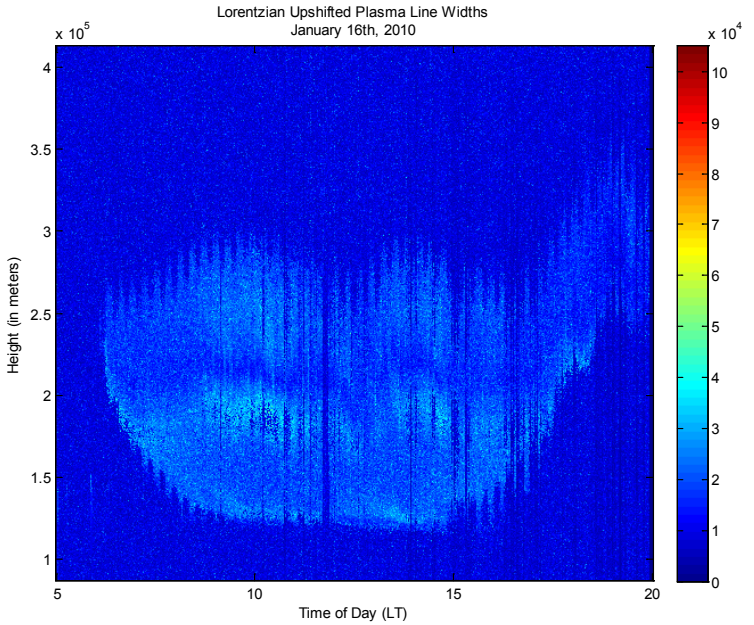

Figure 96: Lorentzian Upshifted Plasma Line Widths; January 16th, 2010.

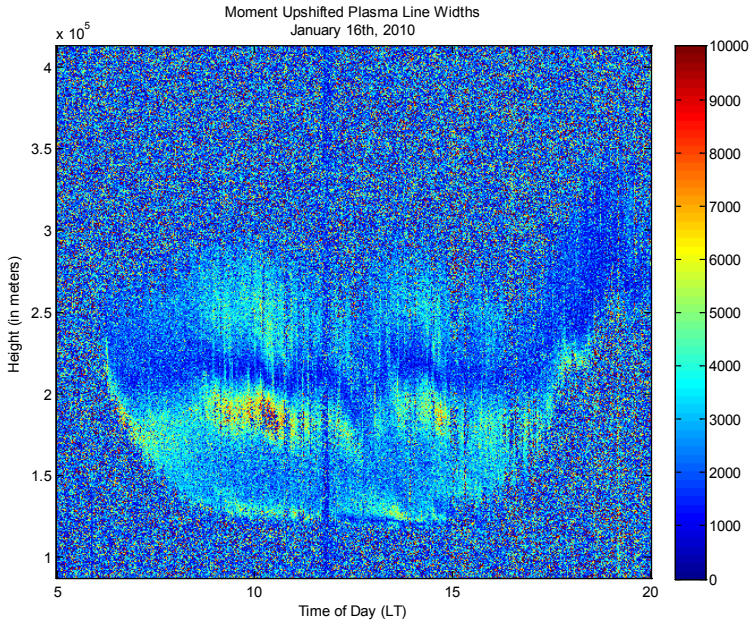

Figure 97: Moment Upshifted Plasma Line Widths; January 16th, 2010.

JANUARY 17TH, 2010

Plasma Line Frequencies

Downshifted

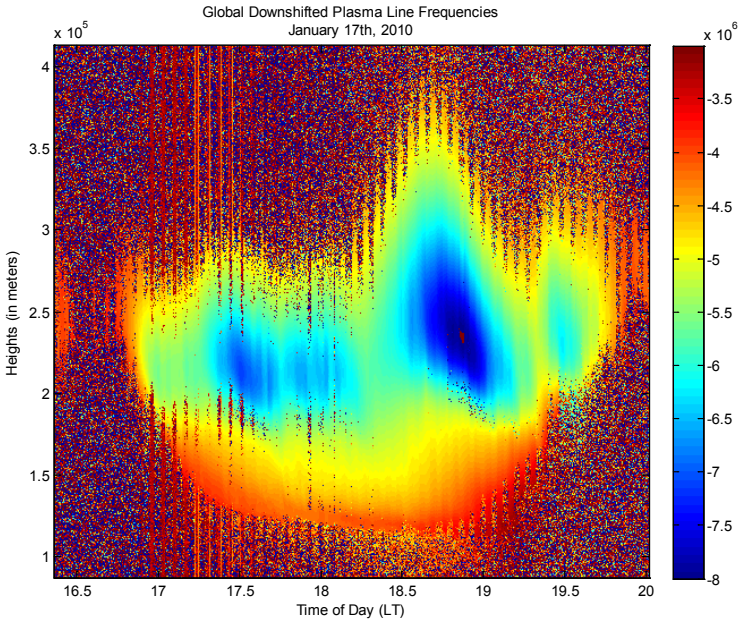

Figure 98: Global Downshifted Plasma Line Frequencies; January 17th, 2010.

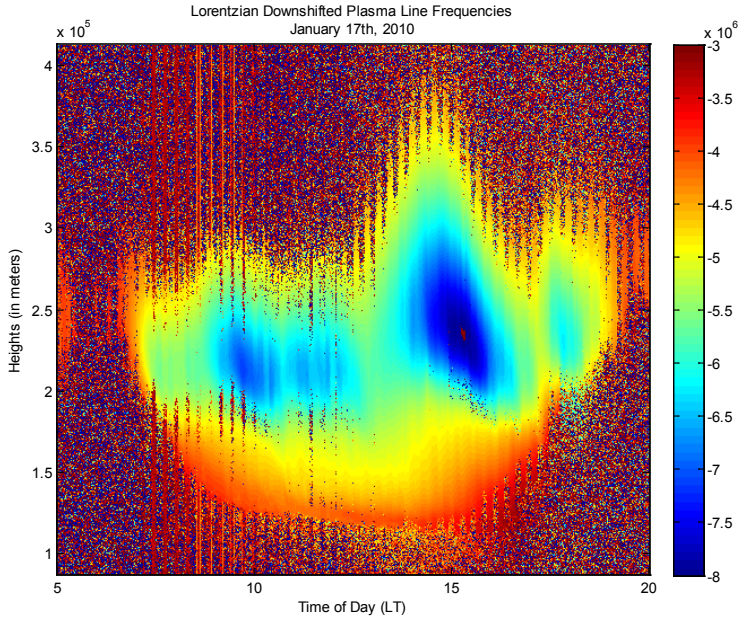

Figure 99: Lorentzian Downshifted Plasma Line Frequencies; January 17th, 2010.

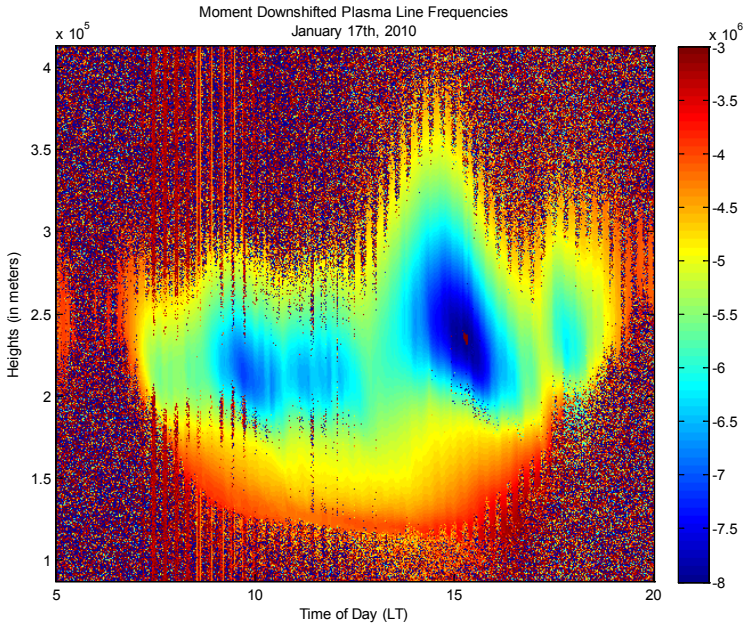

Figure 100: Moment Downshifted Plasma Line Frequencies; January 17th, 2010.

Plasma Line Intensities

Downshifted

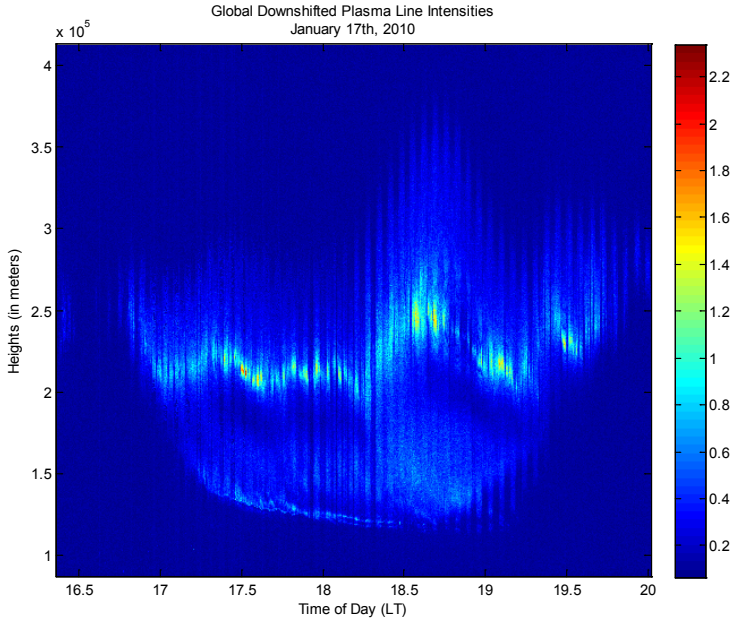

Figure 101: Global Downshifted Plasma Line Intensities; January 17th, 2010.

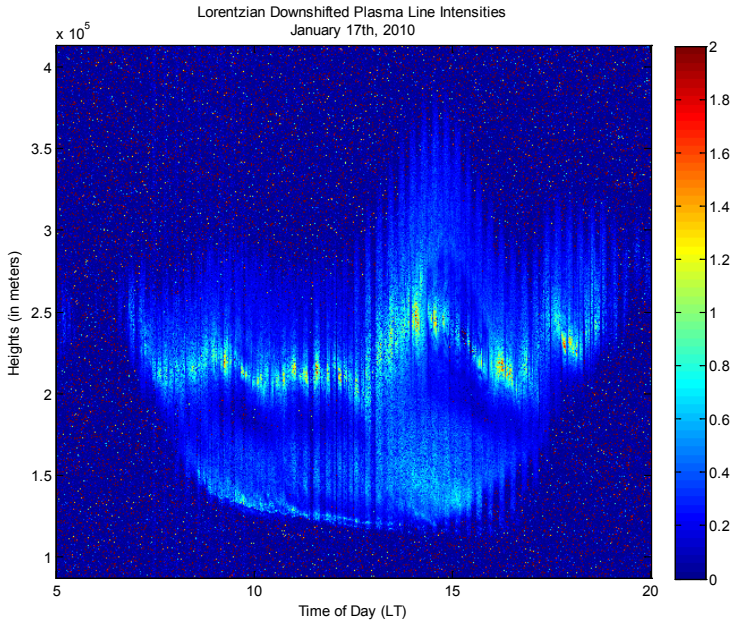

Figure 102: Lorentzian Downshifted Plasma Line Intensities; January 17th, 2010.

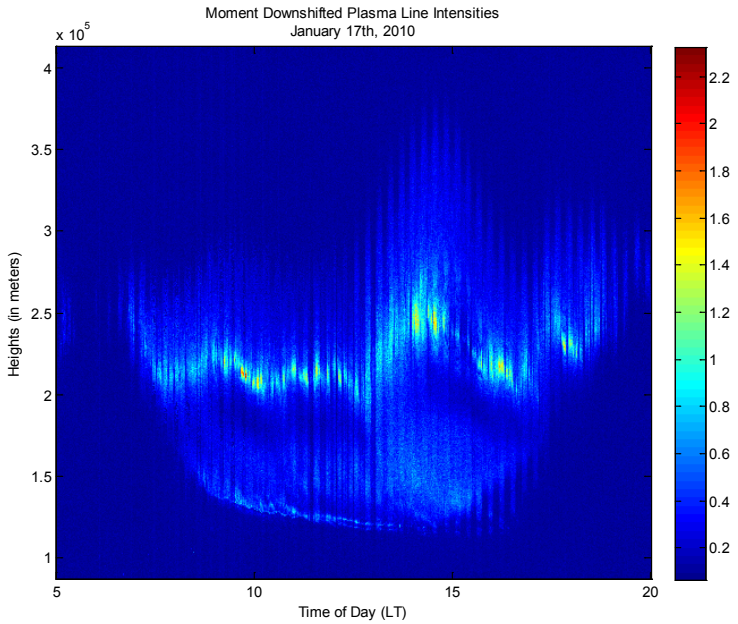

Figure 103: Moment Downshifted Plasma Line Intensities; January 17th, 2010.

Plasma Line Widths

Downshifted

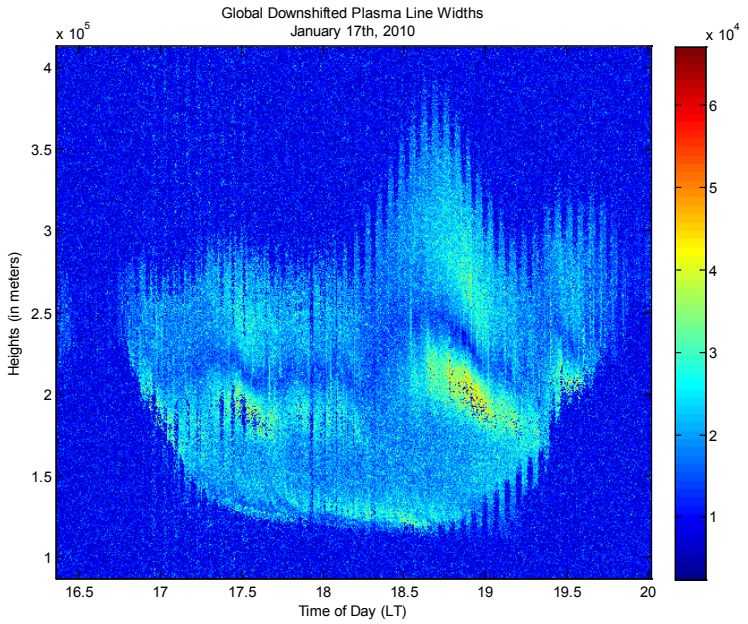

Figure 104: Global Downshifted Plasma Line Widths; January 17th, 2010.

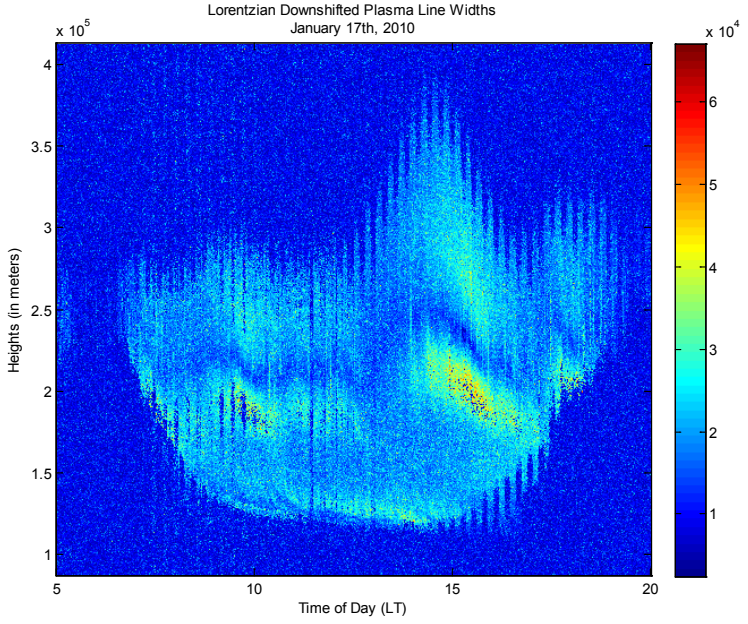

Figure 105: Lorentzian Downshifted Plasma Line Widths; January 17th, 2010.

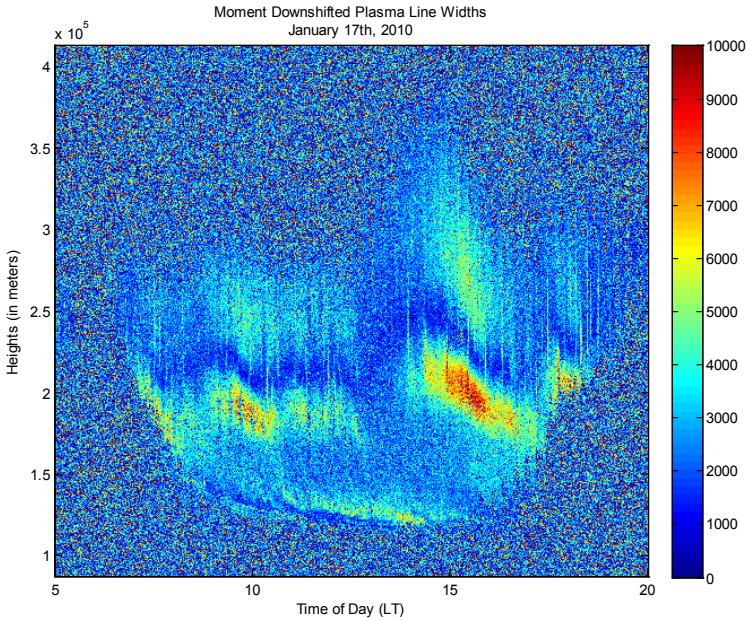

Figure 106: Moment Downshifted Plasma Line Widths; January 17th, 2010.

Plasma Line Frequencies

Upshifted

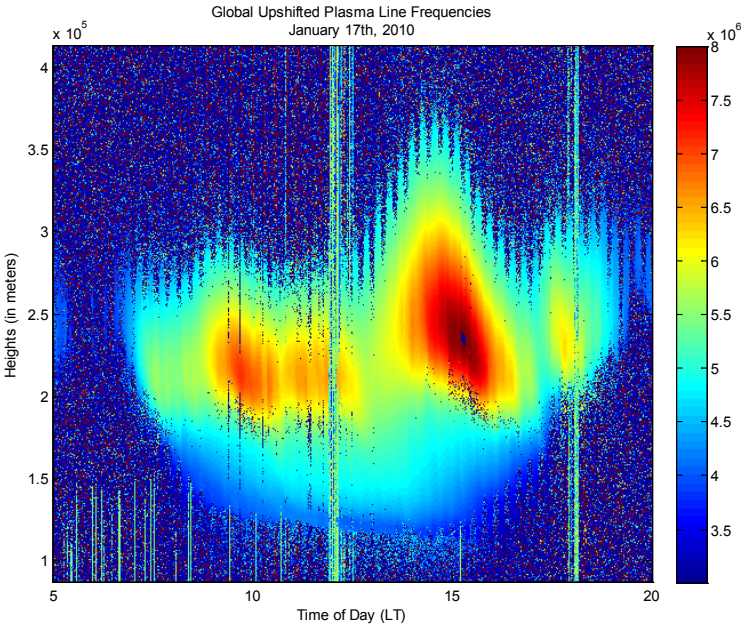

Figure 107: Global Upshifted Plasma Line Frequencies; January 17th, 2010.

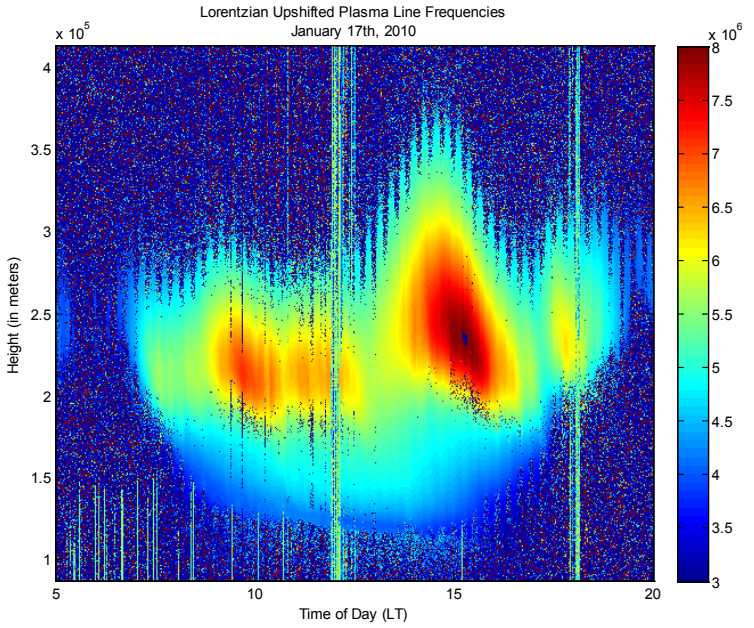

Figure 108: Lorentzian Upshifted Plasma Line Frequencies; January 17th, 2010.

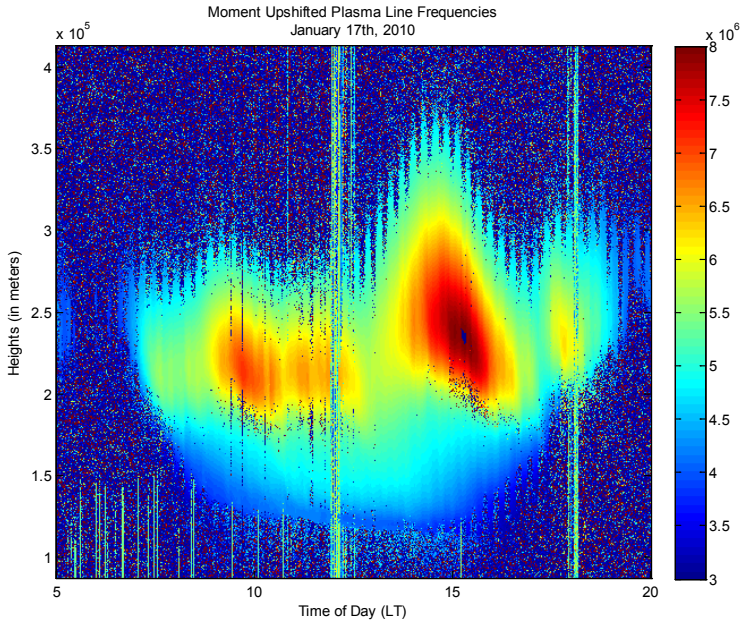

Figure 109: Moment Upshifted Plasma Line Frequencies; January 17th, 2010.

Plasma Line Intensities

Upshifted

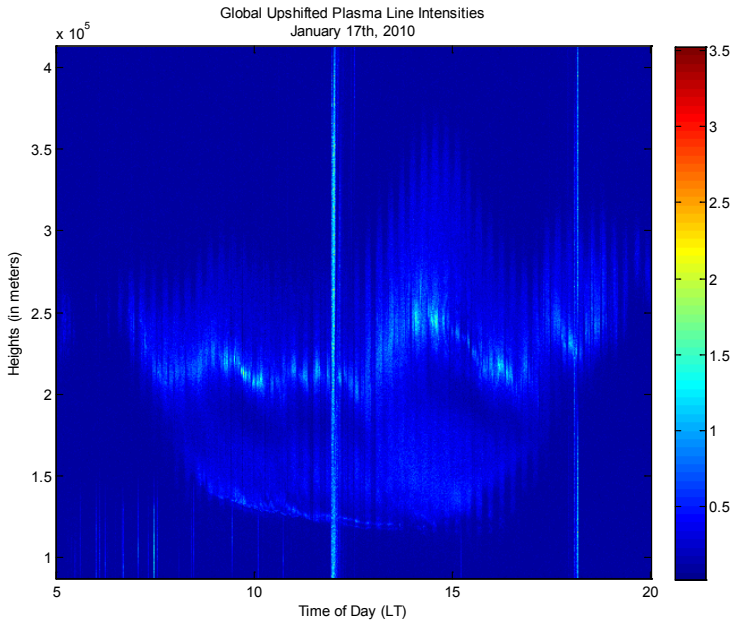

Figure 110: Global Upshifted Plasma Line Intensities; January 17th, 2010.

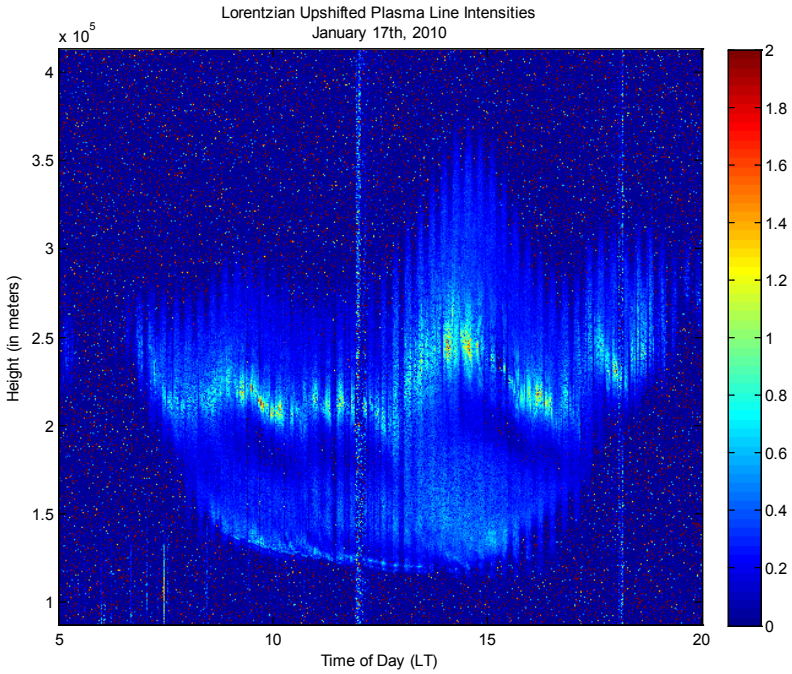

Figure 111: Lorentzian Upshifted Plasma Line Intensities; January 17th, 2010.

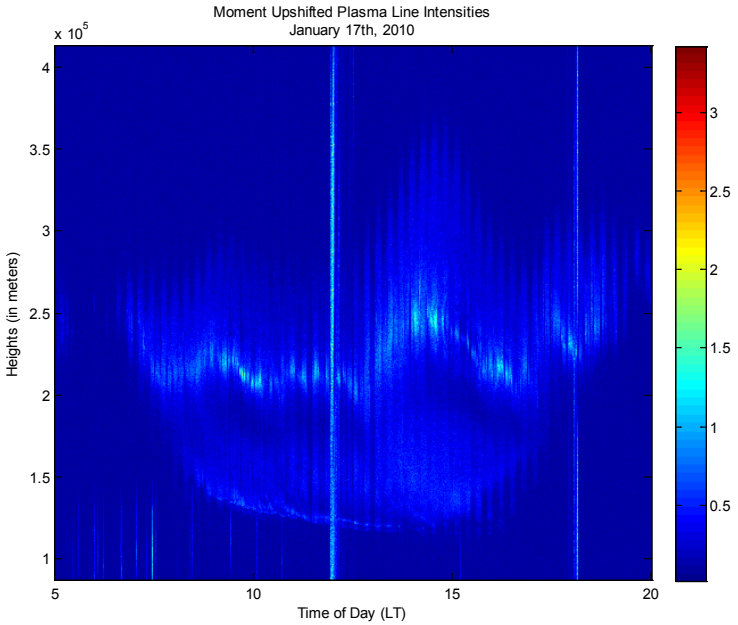

Figure 112: Moment Upshifted Plasma Line Intensities; January 17th, 2010.

Plasma Line Widths

Upshifted

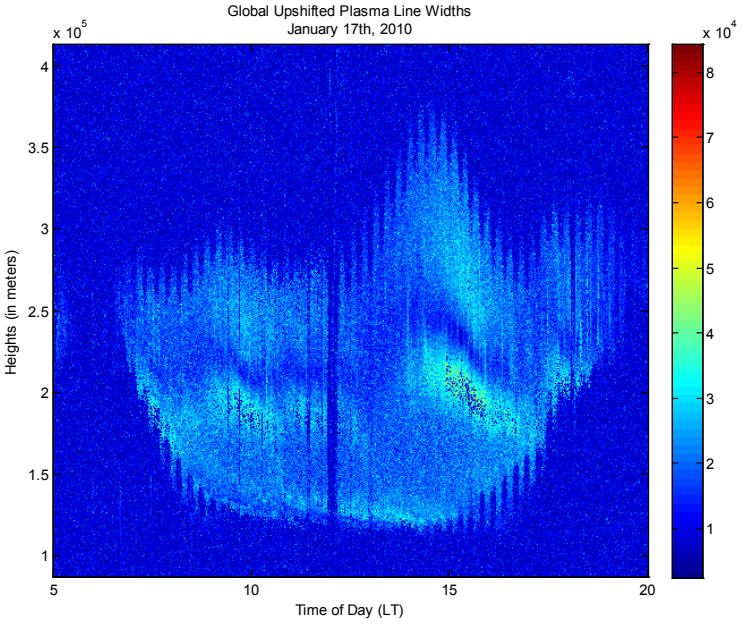

Figure 113: Global Upshifted Plasma Line Widths; January 17th, 2010.

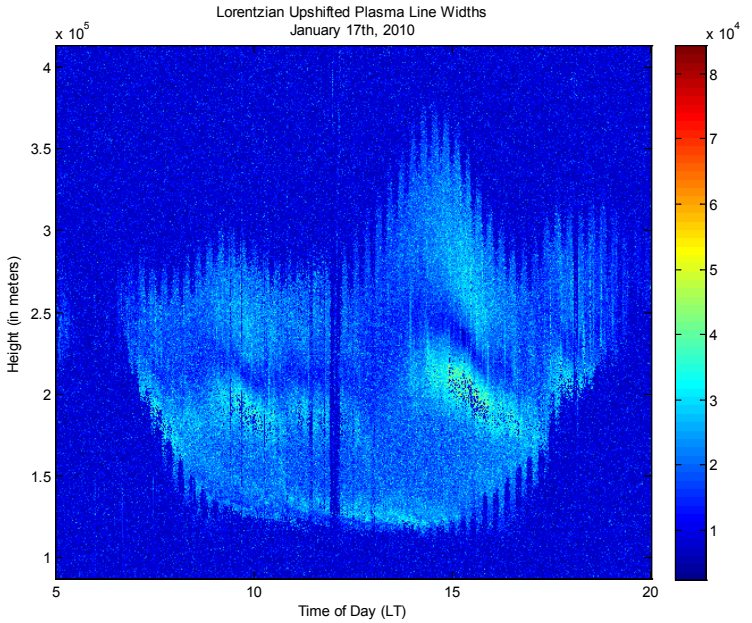

Figure 114: Lorentzian Upshifted Plasma Line Widths; January 17th, 2010.

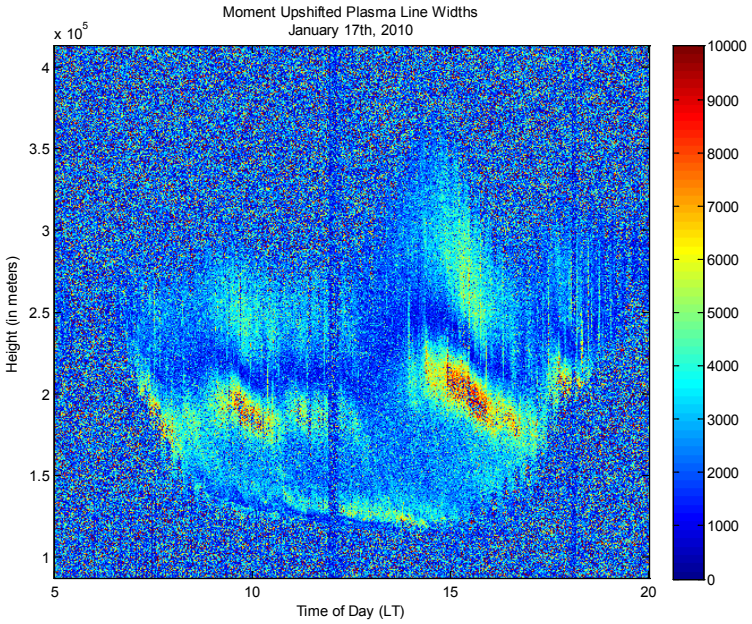

Figure 115: Moment Upshifted Plasma Line Widths; January 17th, 2010.

JANUARY 22nd , 2010

Plasma Line Frequencies

Downshifted

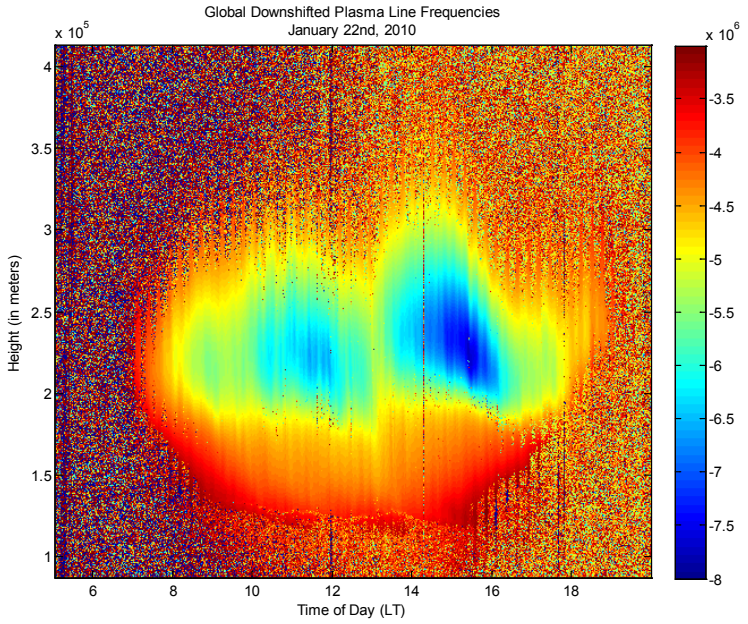

Figure 116: Global Downshifted Plasma Line Frequencies; January 22nd, 2010.

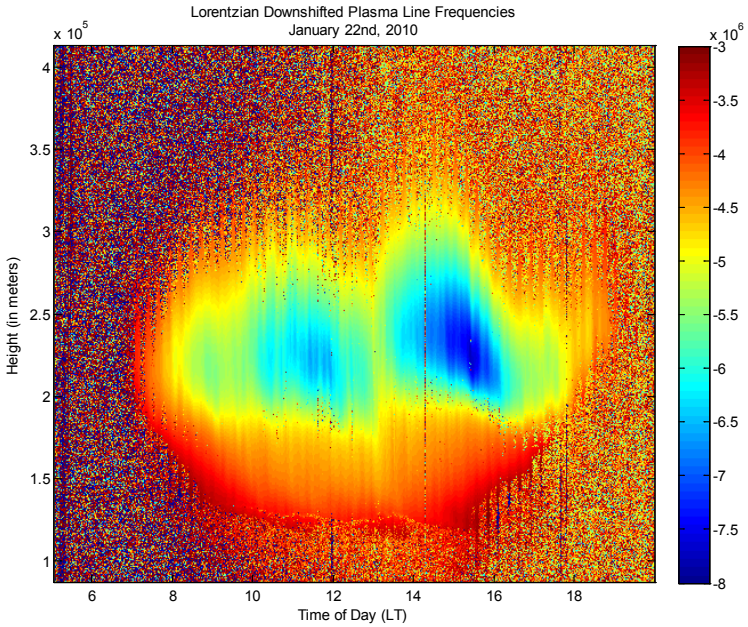

Figure 117: Lorentzian Downshifted Plasma Line Frequencies; January 22nd, 2010.

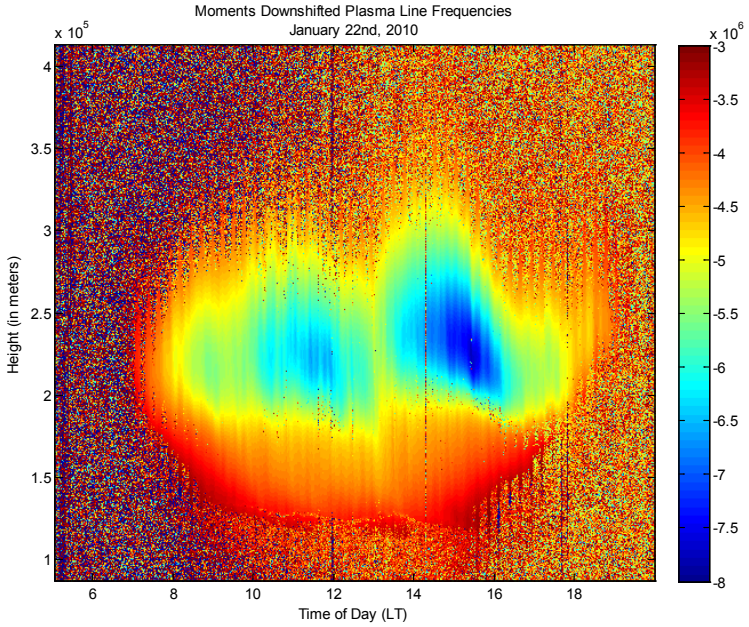

Figure 118: Moment Downshifted Plasma Line Frequencies; January 22nd, 2010.

Plasma Line Intensities

Downshifted

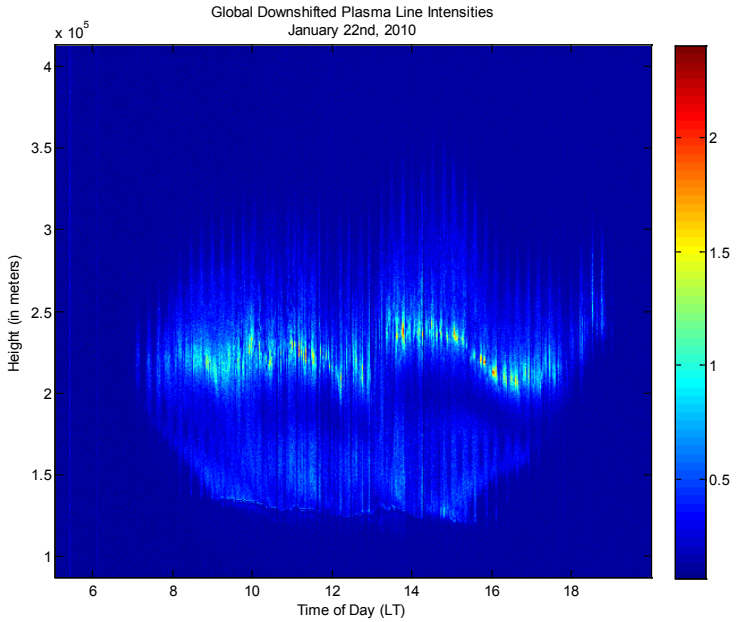

Figure 119: Global Downshifted Plasma Line Intensities; January 22nd, 2010.

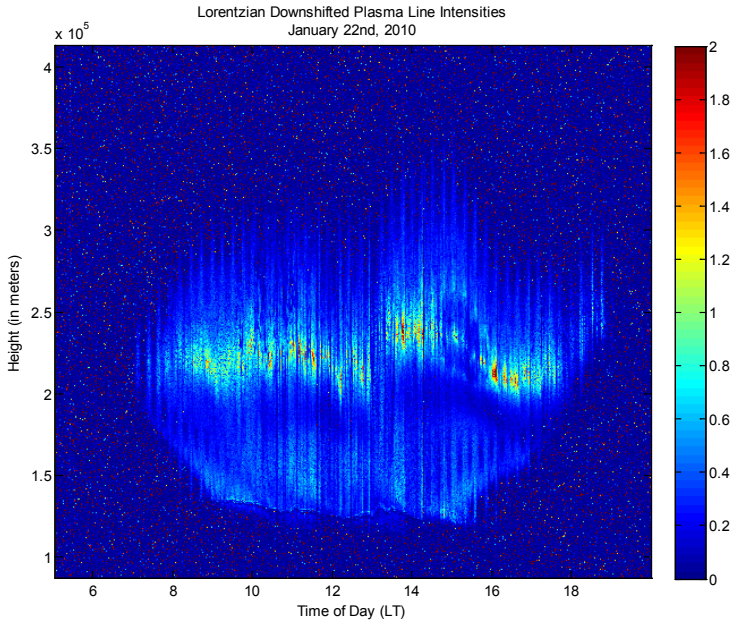

Figure 120: Lorentzian Downshifted Plasma Line Intensities; January 22nd, 2010.

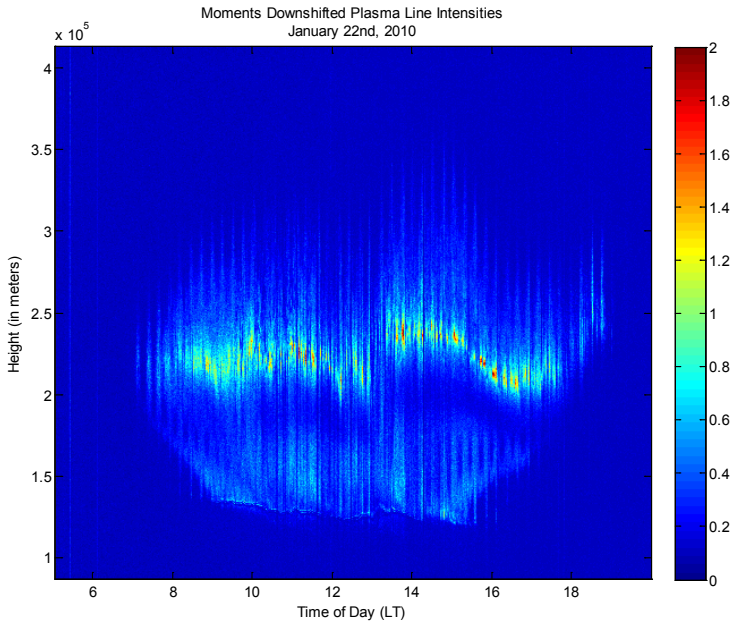

Figure 121: Moment Downshifted Plasma Line Intensities; January 22nd, 2010.

Plasma Line Widths

Downshifted

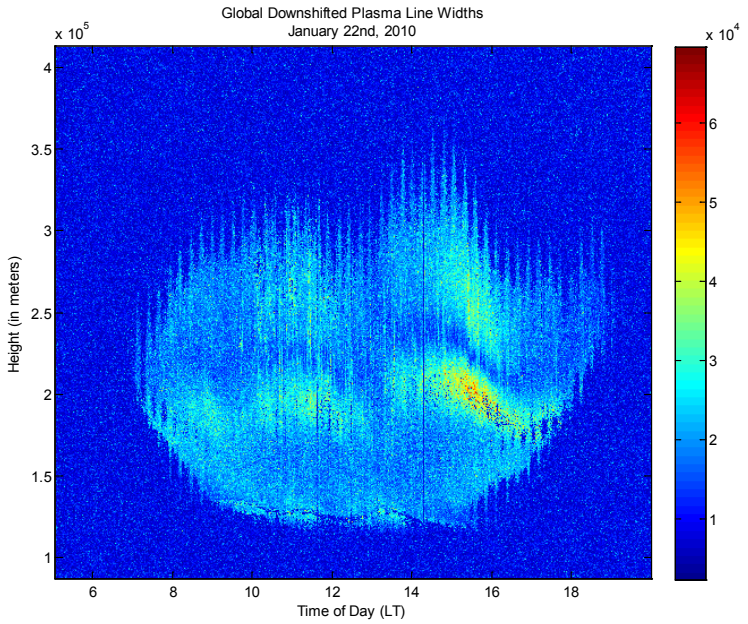

Figure 122: Global Downshifted Plasma Line Widths; January 22nd, 2010.

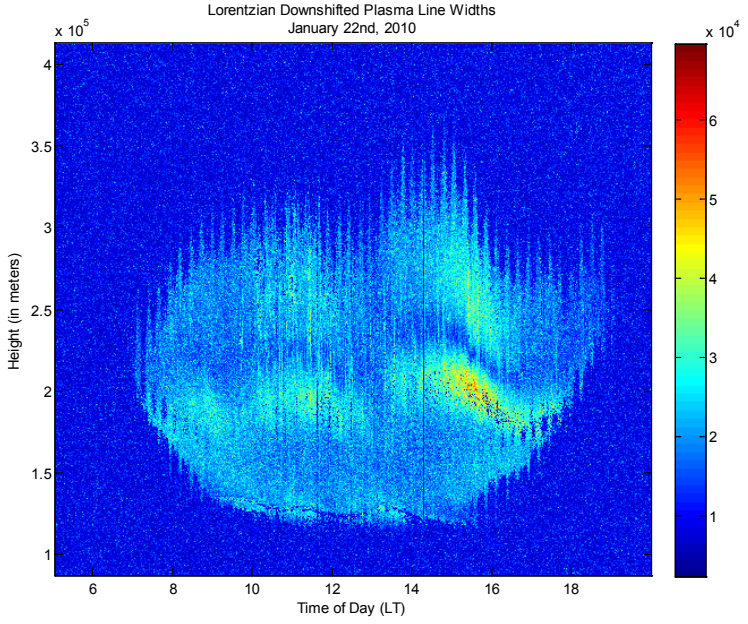

Figure 123: Lorentzian Downshifted Plasma Line Widths; January 22nd, 2010.

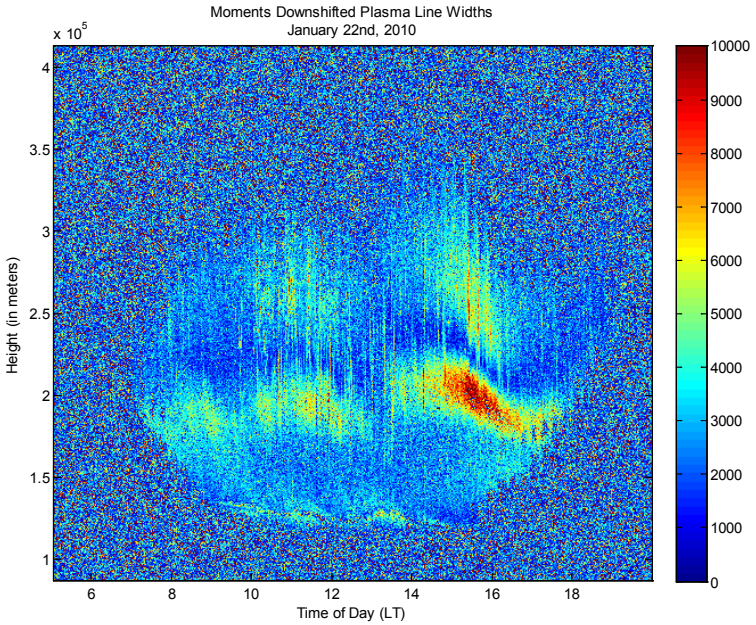

Figure 124: Moment Downshifted Plasma Line Widths; January 22nd, 2010.

Plasma Line Frequencies

Upshifted

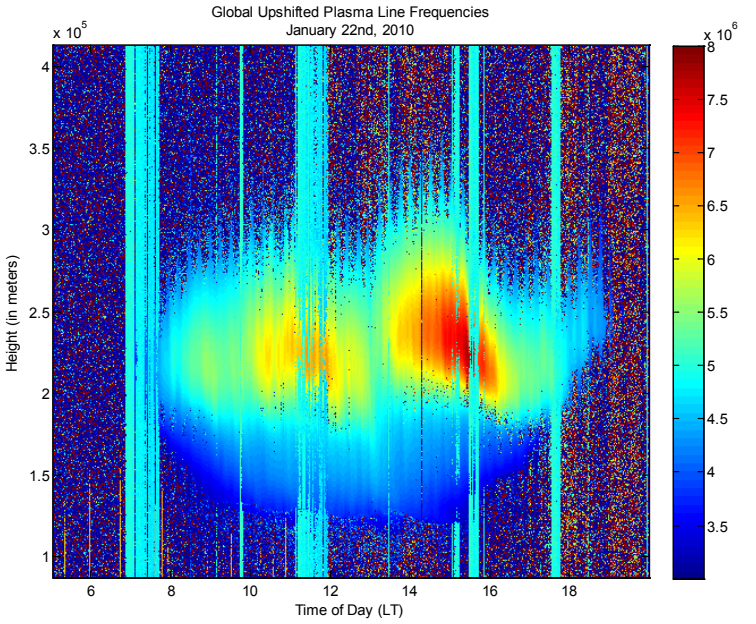

Figure 125: Global Upshifted Plasma Line Frequencies; January 22nd, 2010.

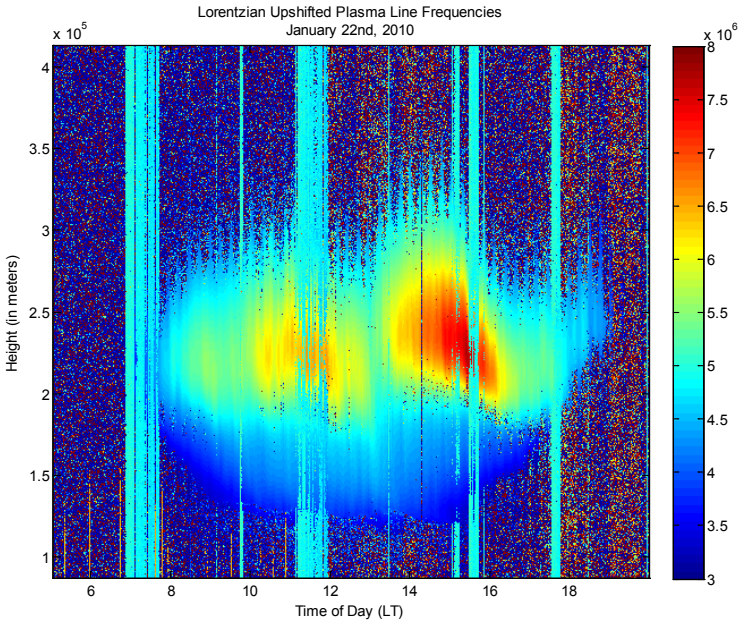

Figure 126: Lorentzian Upshifted Plasma Line Frequencies; January 22nd, 2010.

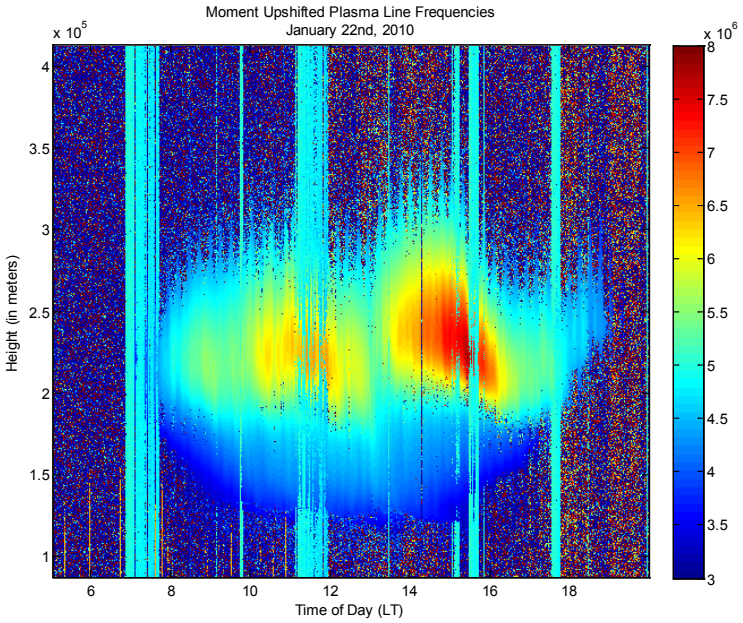

Figure 127: Moment Upshifted Plasma Line Frequencies; January 22nd, 2010.

Plasma Line Intensities

Upshifted

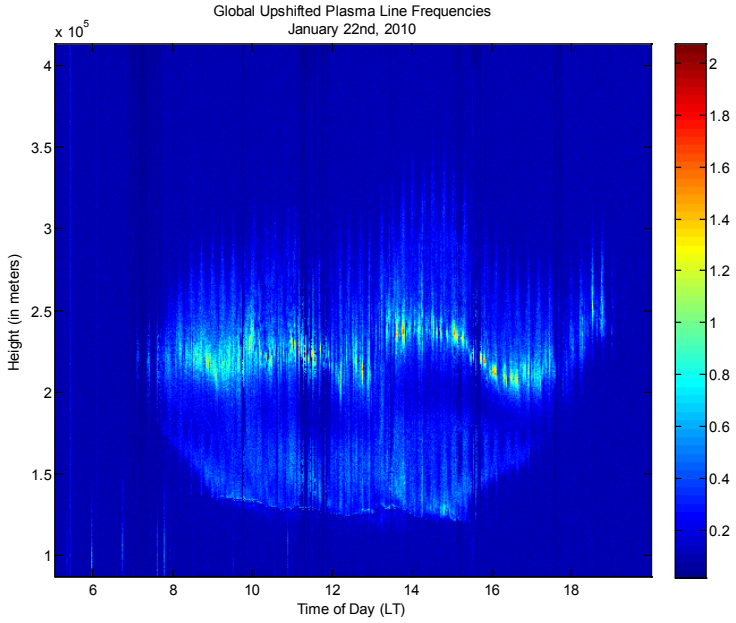

Figure 128: Global Upshifted Plasma Line Intensities; January 22nd, 2010.

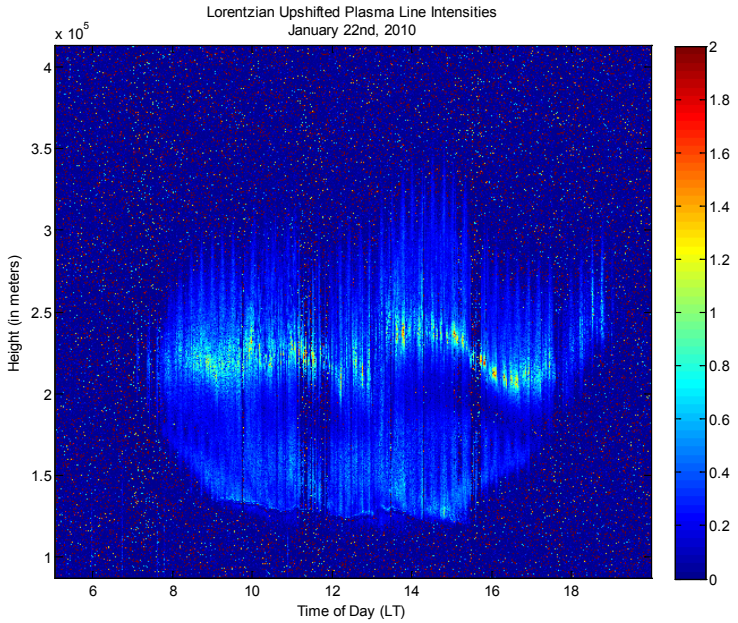

Figure 129: Lorentzian Upshifted Plasma Line Intensities, January 22nd, 2010.

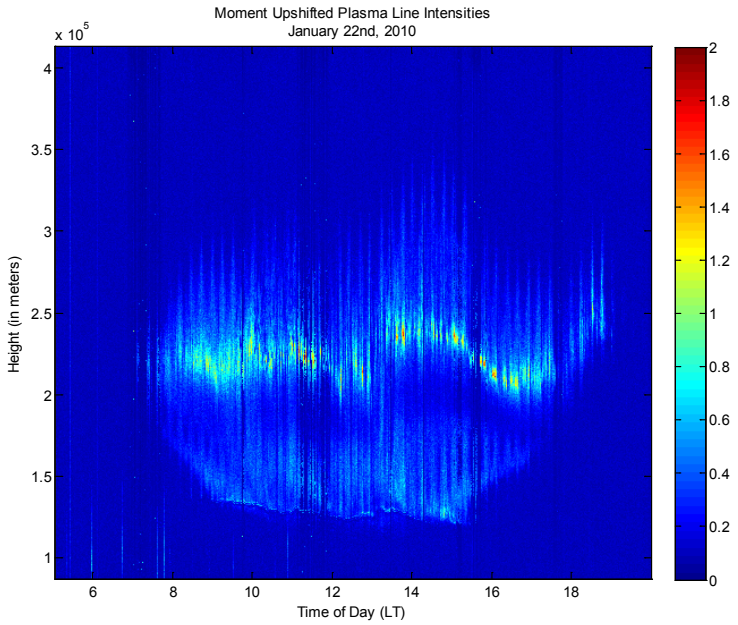

Figure 130: Moment Upshifted Plasma Line Intensities; January 22nd, 2010.

Plasma Line Widths

Upshifted

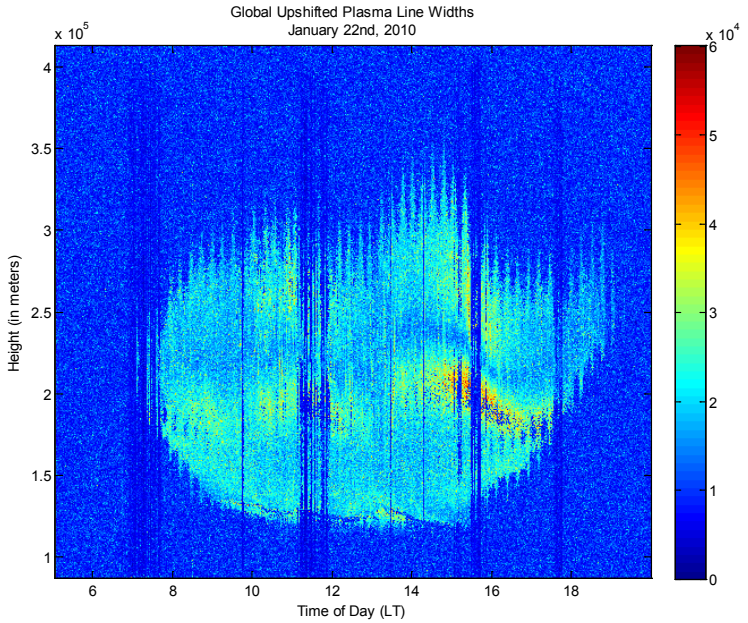

Figure 131: Global Upshifted Plasma Line Widths; January 22nd, 2010.

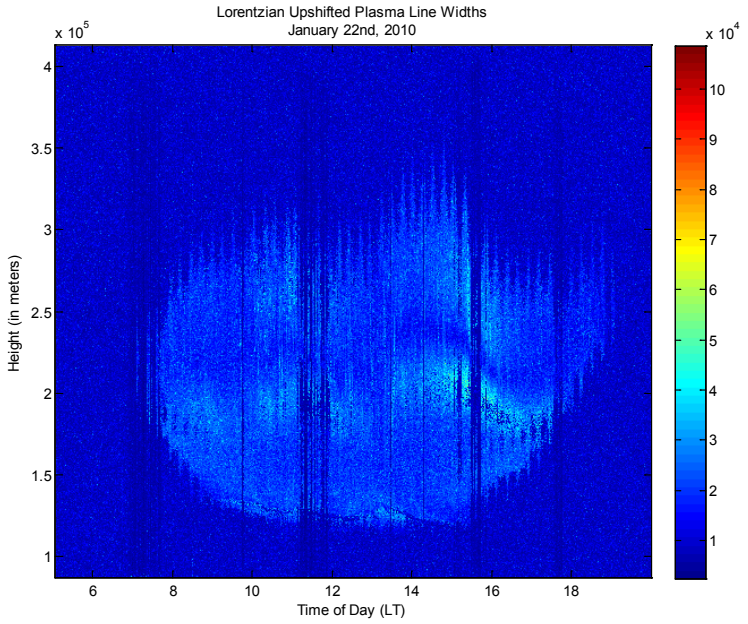

Figure 132: Lorentzian Upshifted Plasma Line Widths; January 22nd, 2010.

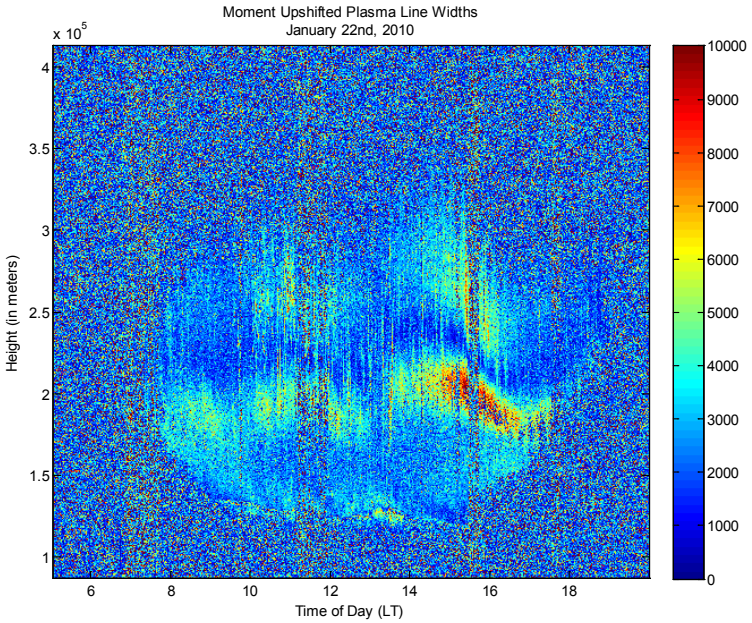

Figure 133: Moment Upshifted Plasma Line Widths; January 22nd, 2010.